AUTOMATED ANALYSIS OF ANATOMICAL STRUCTURES FROM LOW-DOSE CHEST COMPUTED TOMOGRAPHY SCANS

A Dissertation

Presented to the Faculty of the Graduate School

of Cornell University

in Partial Fulfillment of the Requirements for the Degree of

Doctor of Philosophy

by

Jaesung Lee

January 2011

AUTOMATED ANALYSIS OF ANATOMICAL STRUCTURES FROM LOW-DOSE CHEST COMPUTED TOMOGRAPHY SCANS

Jaesung Lee, Ph.D.

Cornell University 2011

Recent advances in CT technologies have enabled clinicians to obtain three-dimensional (3D) volumetric images with high resolution. In this research, fully-automated methods to analyze anatomical structures from chest CT images were developed and evaluated. The main focus of this research was on analyzing low-dose CT images to obtain diagnostic information. All automated analysis methods presented have been designed for and evaluated on CT images taken with low radiation exposure to the patients.

A method was developed for analyzing intrathoracic airways, and the precision of the automated measurement was quantified. A novel contribution of this work was the development of the method for comparative measurement of airways using repeat scans of the same patient, which is clinically relevant for monitoring a patient's condition over time but has not yet been explored by others. A technique for precisely measuring airway's wall thickness was developed, which showed a significant improvement in measurement precision over the conventional full-width half-maximum (FWHM) based measurements.

The segmentation is often a first step in the automated analysis as the segmented organs or structures may be used to retrieve useful diagnostic measures. The algorithms to segment various anatomical structures were developed and validated using large datasets. Top-down approach was used by first performing segmentations of the structures that were robustly identifiable and using those as a basis for segmenting other

structures. The segmentations were performed for airway tree, spinal canal, ribs, and vertebrae, and the experimental results showed that these structures can be segmented robustly from low-dose CT images.

Another aspect of this dissertation was on establishment of a chest frame of reference (CFOR) that serves as a common reference grid for the chest region. Such a reference frame is useful for normalizing chest regions for different-sized individuals, for studying spatial distribution of a certain anatomical point of interest, or for matching anatomical point across different intra-subject CT scans. Experimental results showed that the anatomical points are well-localized when the proposed CFOR was used.

BIOGRAPHICAL SKETCH

Dr. Jaesung Lee was born in Seoul, South Korea. At the age of fifteen, he moved with his family to the United States. In 2001, he graduated from Memorial High School in Houston, Texas. He continued his education at the University of Michigan, Ann Arbor and received a B.S. degree in Computer Engineering (summa cum laude) from the University of Michigan, Ann Arbor in 2004.

He started a M.S-Ph.D program in the School of Electrical and Computer Engineering at Cornell University in 2005. Inspired by the idea of computer-aided diagnosis using medical imaging modalities, he became interested in the field of biomedical image analysis and joined the Vision and Image Analysis group headed by Dr. Anthony P. Reeves. As a member of the group, he has worked on automated analysis of anatomical structures from chest CT scans in close collaboration with Drs. David Yankelevitz and Claudia Henschke at Weill Cornell Medical College.

This dissertation is dedicated to my family and friends.

ACKNOWLEDGEMENTS

First of all, I would like to acknowledge my advisor, Dr. Anthony P. Reeves, to whom I owe my deepest gratitude. This dissertation would not have been possible without his encouragement, guidance, and support.

I would also like to give my gratitude to my other special committee members, Drs. Peter C. Doerschuk and Keith N. Snavely, for their time, support, and assistance, as well as to Drs. David F. Yankelevitz and Claudia I. Henschke at Weill Cornell Medical College for their assistance and feedback over the course of this work.

I thank my colleagues in Vision and Image Analysis group, Dr. Alberto Biancardi, Artit Jirapatnakul, Brad Keller, Jeremiah Wala, and Sergei Fotin, for their enlightening thoughts, friendship, and encouragement. I want to acknowledge other faculty members and students in the School of Electrical and Computer Engineering who provided me with helpful advice along the way.

Finally, I would like to thank my parents, my sister, and my other half for their endless support and trust.

TABLE OF CONTENTS

LIST OF TABLES

LIST OF FIGURES

CHAPTER 1

INTRODUCTION

X-ray Computed tomography, commonly known as CT, is an imaging modality that is widely used in medical practice. CT imaging provides three-dimensional (3D) volumetric image data and allows clinicians to visualize the inside of a patient's body. For a clinician to analyze a 3D volumetric CT images is a very time-consuming and tedious task, and computer-aided analysis of volumetric image data is often desirable. The focus of this research was to develop a system which, given a CT scan, will automatically analyze anatomical structures to obtain useful diagnostic information.

1.1 Background and motivation

Recent advances in CT technologies have enabled clinicians to obtain 3D volumetric images with high resolution. Accordingly, there has been an increase in amount of image data to be processed by the clinicians, and computer-aided diagnosis (CAD) systems have received much attention [9, 19, 20, 30, 47, 92].

CAD systems assist physicians in analyzing and interpreting medical images. The CAD systems have been widely used to diagnose diseases such as breast cancer [10, 18, 28], lung cancer [25, 45, 73], and colon cancer [15, 26, 87]. Manually analyzing medical images is a very time-consuming task for physician, especially for 3D volumetric images. Using computers to analyze medical images not only increases chance to detect cancer at early stage [9] but also allows for efficient interpretation of images taken for large group of patients.

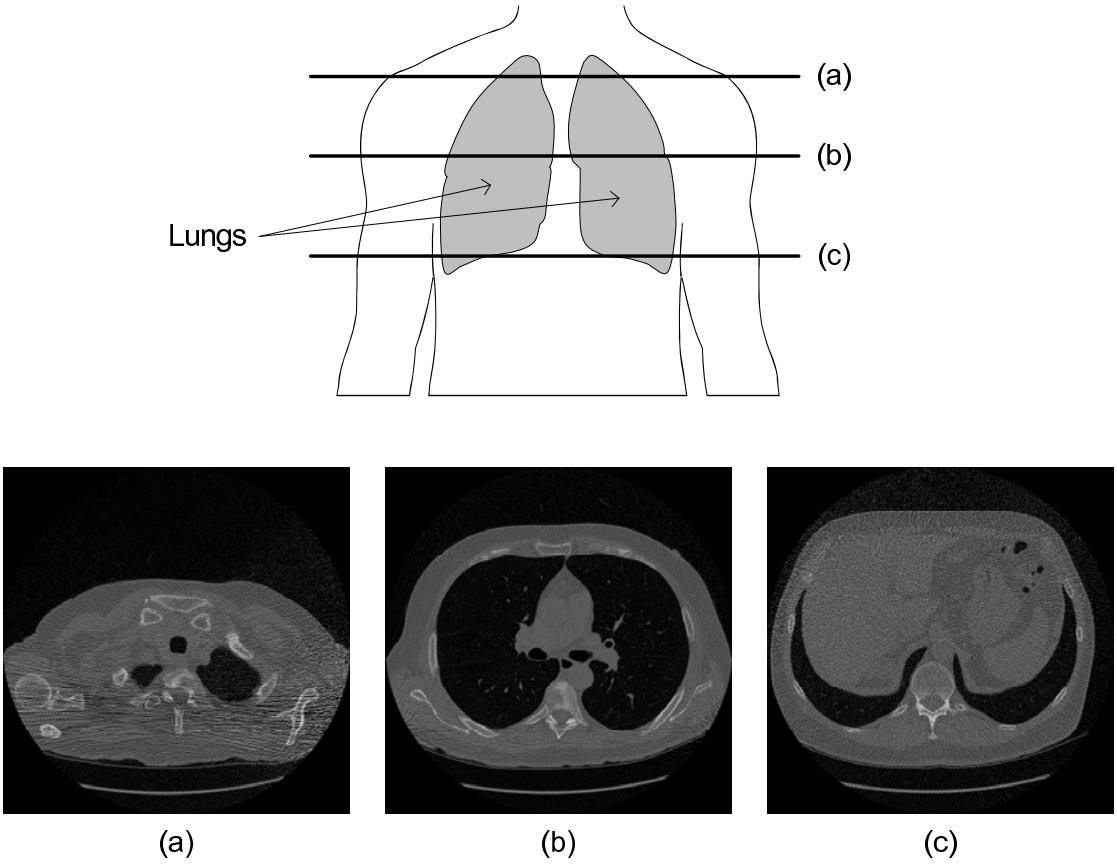

Figure 1.1: An example of chest CT scan. The axial image slices are shown at different body locations (top, middle, and bottom regions of the lungs). Actual CT scan spans through the entire chest region, but only three selected images are shown here for illustration purpose.

1.1.1 Low-dose Computed Tomography (CT)

3D volumetric CT data is obtained by taking a series of 2D X-ray images from different views around the body. 3D CT data is processed to obtain a set of axial images, where each image represent a slice through a human body as shown in Figure 1.1.

Every pixel in an axial image represents a cubic volume in 3D space, rather than a rectangle in a flat 2D image, and therefore it is commonly referred to as a “voxel”.

The image intensity of each voxel is the estimation of a radiographic density and is represented using Hounsfield units (HU). CT scans are calibrated and should have -1000 HU for air and 0 HU for water. This is a major advantage of CT imaging over other imaging modalities when performing computer-aided analysis, since one can expect to see a certain intensity range for an organ or structure of interest.

When acquiring a CT scan, the radiation exposure is a major concern and may involve serious consequences. Ionizing radiation absorbed by body tissues can cause damage to DNA which may result in cancer [5]. The radiation exposure of $\leq$3 mSv per year is considered a low dose [13], as this is comparable to what an average person in the United States received from naturally occurring radiation [14]. The cancer risk of radiation exposure has been studied in the past by analyzing the atomic-bomb survivors [65–67]. These studies have used a simple linear model to estimate the risk of low radiation doses and observed a significant increase in cancer risk for the doses ranging from 5 to 150 mSv [5].

A standard chest CT imaging involves an approximate radiation dose of 7 millisievert (mSv), while a low-dose CT imaging involves approximately 1.5 mSv [68]. While there is no consensus on the risk factor of CT imaging, everyone agrees that there is a tradeoff between radiation dose and image quality, and the ideal balance is to obtain an image which is adequate for the clinical purpose with the minimum radiation dose [52].

The CT scans for screening purposes are usually taken with a low radiation dose. The low-dose chest CT scans for lung cancer screening are taken mainly to discover a malignant pulmonary nodule at its early stage [27]. However, the 3D volumetric data present may still be used for analyzing other anatomical structures and may provide physicians with useful information for patient monitoring and treatment planning. The major airways are identifiable in the low-dose images up to 6th generations in most

cases. The airways can be analyzed to measure dimensions that may be relevant in diagnosing pulmonary diseases [2, 57]. Further, the major bone structures are clearly visible in chest CT images and may be analyzed to measure bone mineral density, which is an indicator of osteoporosis and bone strength [94].

1.1.2 Analysis of intrathoracic airways

Airways are tubular structures through which air is transferred to the lungs. The entire set of airways in a human appears as a tree-like structure and is often referred to as an "airway tree". The term "airway segment" refers to one cylindrical tube within the airway tree, as illustrated in Figure 1.2, and is used interchangeably with the term "airway branch" throughout this dissertation. Air enters a human body through the trachea, the top-most airway segment. The trachea divides into two main bronchi, the left and right bronchus, which further divides into smaller airways.

Currently, whole-lung CT is the main imaging modality for obtaining volumetric information of the human airway [8, 23]. An individual segment of an airway tree is a tubular structure and appears in CT images as a low-intensity lumen area ($\approx$ -900 HU) that is surrounded by high-intensity wall and adjacent structures ($>$ 0 HU), as shown in Figure 1.3.

A main interest in the quantitative analysis of airway dimensions is to aide in the diagnosis of chronic obstructive pulmonary disease (COPD). The COPD is currently fourth leading cause of death in the United States [59] and includes two subtypes, chronic bronchitis and emphysema. Chronic bronchitis is characterized by inflammation of airways, and emphysema is characterized by destruction of lung tissue around small airways. The standard tool for diagnosing COPD is the pulmonary function test

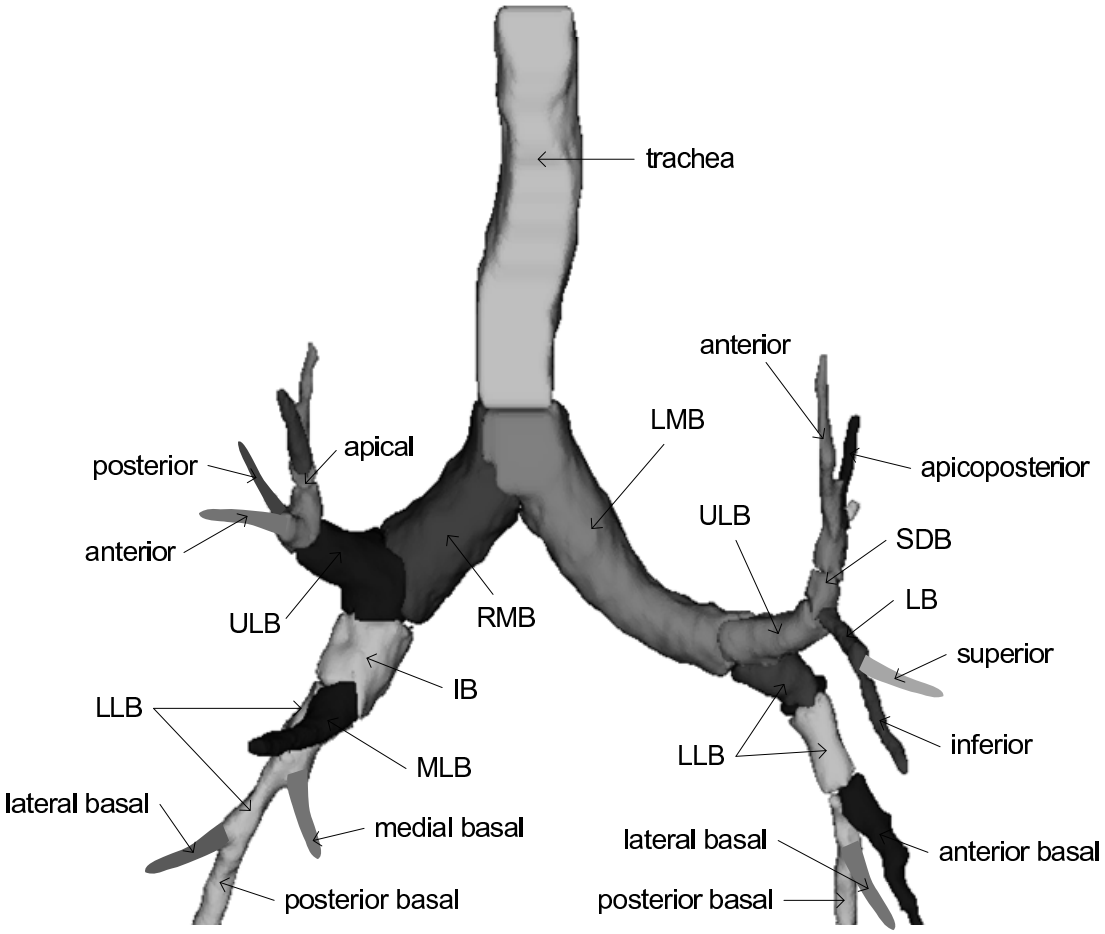

Figure 1.2: Nomenclature for human airway segments [58]. The abbreviations shown in the figure include RMB (right main bronchus), LMB (left main bronchus), ULB (uppoer lobe bronchus), MLB (middle lobe bronchus), LLB (lower lobe bronchus), IB (intermediate bronchus), SDB (superior division bronchus), and LB (lingular bronchus).

(PFT). The PFT provides quantifiable measures of lung function and is helpful in diagnosing pulmonary diseases. The current most common form of PFT is using spirometry, a practice of letting patient exhale into the tube, which measures the movement of air into and out of the lungs.

Two main quantities measured by spirometry are forced vital capacity (FVC) and forced expiratory volume in 1 second (FEV1). FVC measures the volume change be-

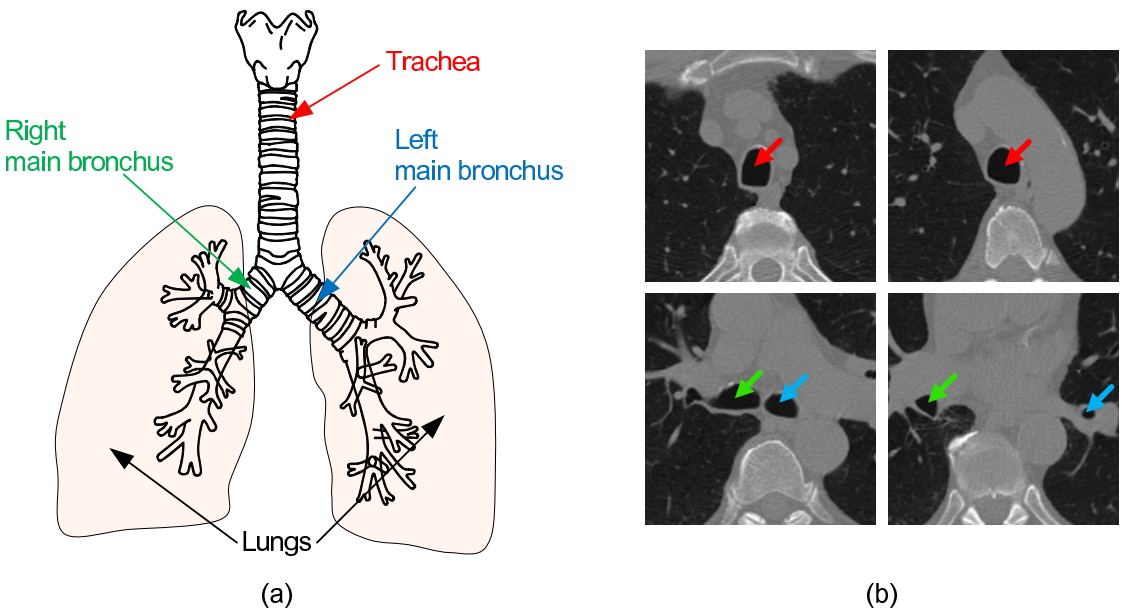

Figure 1.3: Human airways. (a) Illustration of a human airway tree with trachea and the main bronchi labeled. (b) Airways in a CT scan. Clipped axial images of a CT scan with the arrows pointing at the trachea and two main bronchi are shown.

tween full inspiration to the maximum expiration, and FEV1 measures the volume exhaled during first second. The COPD is diagnosed as different stages based on the normalized measures including FEV1/FVC and FEV1%. FEV1/FVC is the ratio between FEV1 and FVC and is normalized by subject's lung capacity. FEV1% is normalized with respect to patient demographics such as age, gender, and height. Table 1.1 summarizes how COPD is categorized into different stages.

Most previous clinical studies concerning the quantitative airway measurements from CT images have focused on correlating airway dimensions with PFT scores. Nakano et al. [57] used chest CT images to evaluate airway wall thickening in 114 COPD patients. They manually identified a CT image slice with the apical bronchus for each patient, measured the airway's cross-sectional wall area (WA) and outer area (OA),

Table 1.1: Classification of COPD stage using PFT scores [93]

Stage	FEV1/FVC	FEV1%
Mild	<0.70	≥80
Moderate		50-79
Severe		30-49
Very severe		<30

and correlated the WA/OA ratio with FEV1% ($r = -0.34$). Berger et al. [2] compared airway wall thickening in 24 patients with and without COPD. They manually selected approximately 40 airways for each patient, measured WA and lumen area (LA), and correlated WA/LA ratio with FEV1% ($r = -0.51$).

While human airways can be visually identified in CT scans, it is not an easy task to perform a quantitative analysis manually. Manual analysis of airways in CT is especially challenging due to the amount of volumetric data and the complexity of human airway system. Automated measurement of the airways reduces subjective bias and saves time when compared to the manual measurement. Further, volumetric measurement, by assessing all available data in 3D CT images, provides more precise measurement than taking the measurement from a single 2D image.

The airway tree structure must first be segmented from a CT image in order to perform analysis. There have been considerable amount of interest for automated segmentation of human airways [16, 22, 42, 90, 91, 96]. The term "airway segmentation" is misleading because the automated algorithms segment the lumen of the airway rather than the entire structure including the airway wall. The reason why the most algorithms segment only the lumen region is due to the fact that the lumen appear relatively dark and is much easier to segment automatically than the entire airway structure.

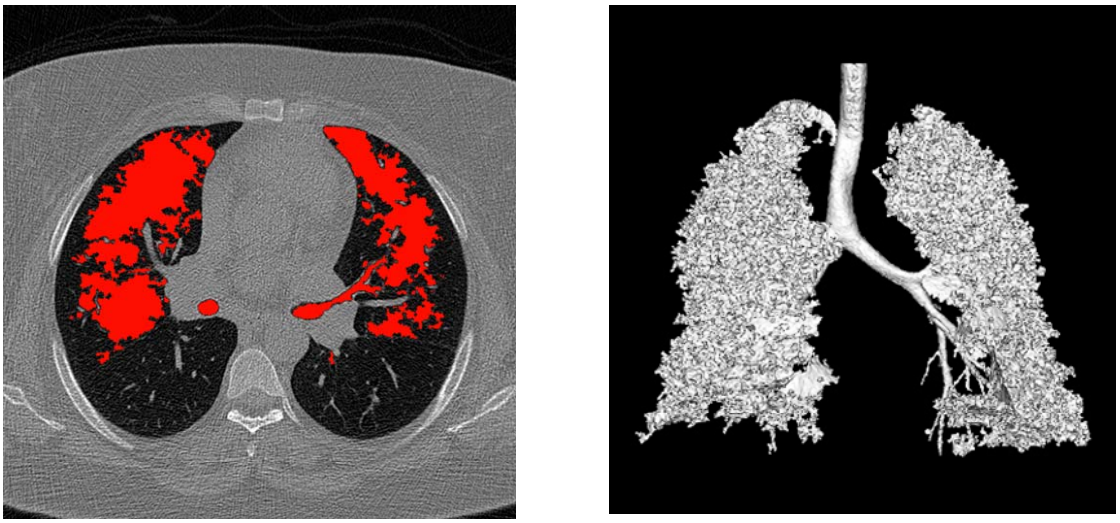

Figure 1.4: Leakages in airway segmentation. The segmentation is prone to a leakage into lung parenchyma when a simple 3D region growing is used. (a) The segmentation outcome overlayed onto the scan. (b) 3D rendering of the segmentation.

The main challenge of automatically segmenting the airway tree is to avoid what is commonly known as a "leakage". The segmentation is said to have "leaked" when the segmentation algorithm mistakenly identifies the lung parenchyma region as a part of airway. Segmenting the airway tree conservatively by minimizing leakage is important for subsequent analysis of airways, since any analysis based on a false segmentation is undesirable. When using a simple region growing algorithm, the segmentation is vulnerable to a leakage in small airways where the airway wall is relatively thin, as shown in Figure 1.4. Avoiding leakage is especially challenging when using low-dose CT images due to the amount of image noise.

The automated method has been developed for assessing dimensions of individual airway segments. The dimensions of interest were the lumen diameter and wall thickness, as depicted in Figure 1.5. Another contribution is on the comparative measurement

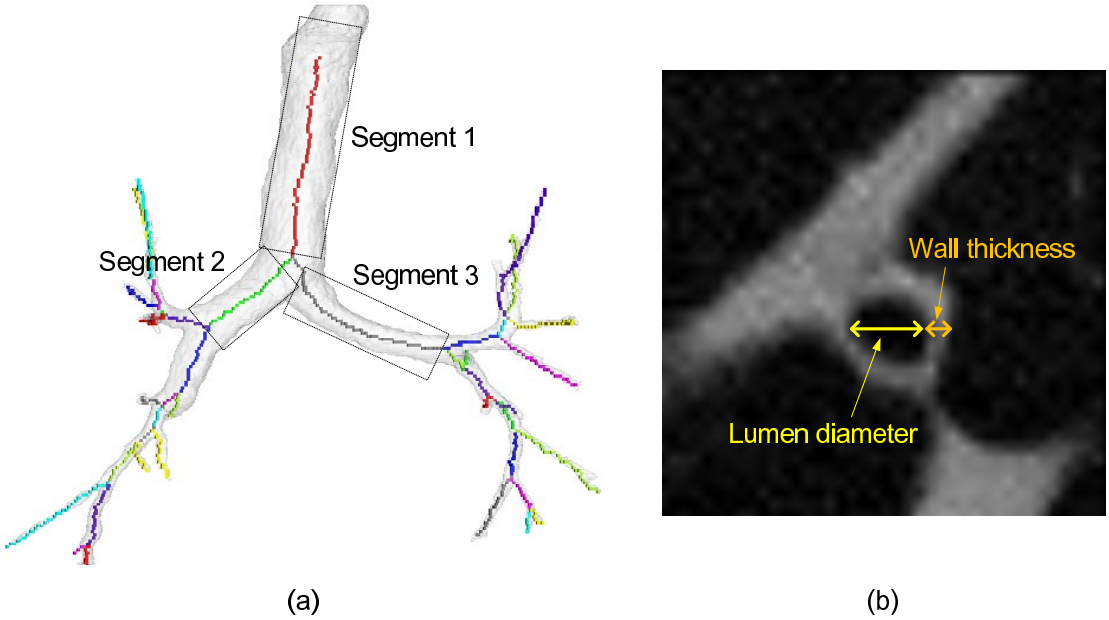

Figure 1.5: Airway segments and dimensions. (a) First three segments are labeled on a 3D visualization of the airway tree. The centerlines of individual segments are drawn with different colors. (b) An airway on a clipped CT image slice (zoomed in) showing a lumen diameter and wall thickness. The average airway dimensions are assessed or each segment.

of airways using multiple CT scans of same patient. No previous works have addressed the issue of analyzing airways using serial low-dose CT scans which is important for monitoring a patient's condition.

1.1.3 Segmentation of anatomical structures

In computer vision, segmentation is the process of partitioning an image into multiple regions. In medical imaging perspective, segmentation of an anatomical structure refers to a selection of image voxels that belong to the structure of interest. There are various organs and structures that appear in a chest CT scan, as shown in Figure 1.6.

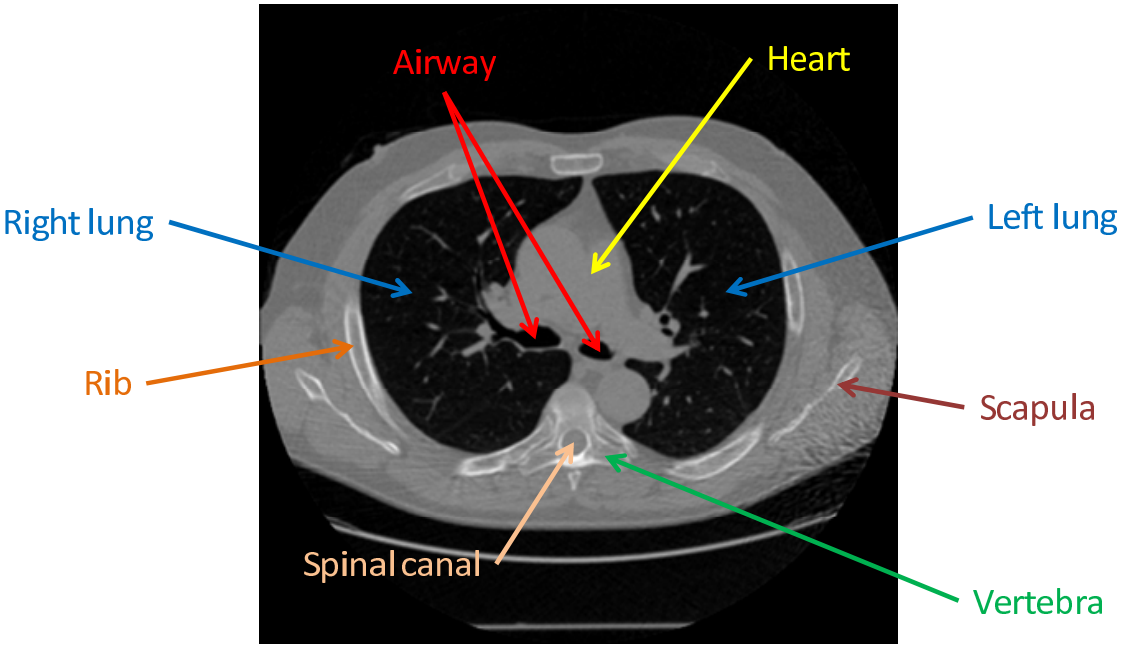

Figure 1.6: Anatomical structures in a CT image.

The segmented organs and structures may be analyzed quantitatively or morphologically to aid patient diagnosis. Further, segmentations of various anatomical structures within a chest CT scan yield a labeled atlas of the chest region. Such an atlas provides:

- Quantitative information to radiologists
- A basis for comparing across population and different scans of same patient
- An opportunity for surgical planning and computer-guided surgery

The organs and structures in human body are 3D volumes, and manual segmentation must be performed on multiple 2D images and is tedious, inaccurate, and time-consuming. Automating a segmentation is essential in a CAD system since such a manual operation requires a heavy workload for a physicians. Further, the automated segmentation allows for batch analysis of large group of patients. In this dissertation,

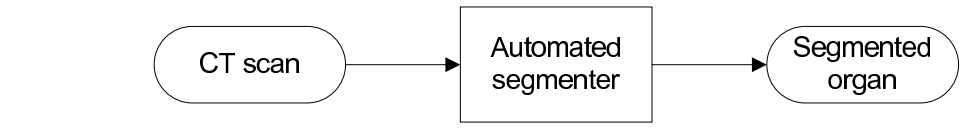

(a) Fully-automated segmentation

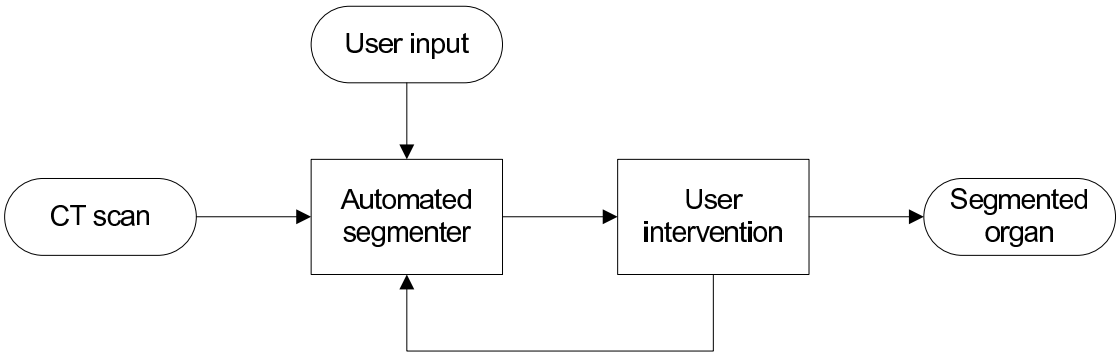

(b) Semi-automated segmentation

Figure 1.7: Flowcharts for (a) fully-automated and (b) semi-automated segmentations. For semi-automated method, either user intervention may or may not be required.

the automated segmentation algorithm is presented for various anatomical structures including lungs, airways, spinal canal, ribs, and vertebrae.

When an "automated" segmentation is discussed in a paper, it usually means one of two computer-aided segmentation approaches: fully-automated and semi-automated, as illustrated in Figure 1.7. The fully-automated segmentation is where an algorithm takes a CT scan and outputs a segmentation. Semi-automated segmentation, on the other hand, is where an algorithm must be provided with additional input from the operator, such as a seed point or interactive correction. The objective was to develop a system that will analyze a given CT scan without any user intervention, and therefore, only fully-automated segmentation was considered.

To perform automated segmentation, the distinct features of an anatomical structure of interest need to be identified. There are three main features that can be used to segment an organ or structure:

- Image intensity: The expected intensity can be used to recognize the structure of interest. This is possible since CT image intensities are calibrated. For example, airway lumen and lung parenchyma are expected to appear in relatively low intensities, while dense structures, such as bones, are expected to appear in high intensities.
- Geometrical shape: The expected shape of the anatomical structure can be used. Although there are anatomical variations for different individuals, each structure should have an expected geometrical shape that distinguishes it from other anatomical structures.
- Relative location: The relative position with respect to other pre-segmented structures can be used. The variation in relative organ locations in human chest anatomy is limited, and whenever there are other previously-segmented organs, they can be used to refine the search space for the segmentation.

It is not necessary to use all the features listed above, and the selection of features depends on the characteristics of the anatomical structure to be segmented. However, using as many features as possible is likely to result in a segmentation algorithm with a robust performance.

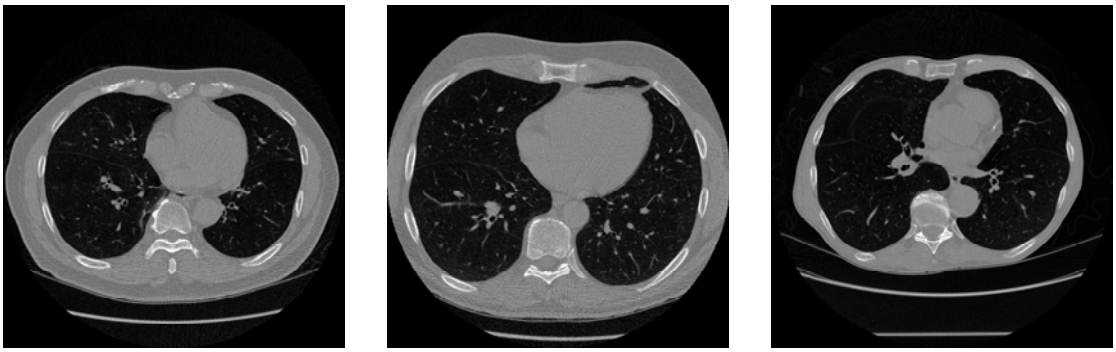

Figure 1.8: Variation in patient size and position. For each of three scans, an image slice 20 cm below the top-most image is shown. All scans were taken with same acquisition parameters and imaging protocol.

1.1.4 Chest frame of reference

Another aspect of this research is on the common reference grid for the chest region to which any given chest CT scan can be mapped. Such a reference frame, referred to in this dissertation as "chest frame of reference (CFOR)", will provide an opportunity to perform useful analysis of anatomical structures. Specifically, it provides a mechanism to:

- Refer to a specific location within the chest for any chest CT scan.
- Match locations of organs and anatomical features across scans.
- Perform comparative studies for a large group of subjects.

The variation of chest appearances in different CT scans poses challenges when establishing a standardized chest frame of reference (CFOR). The size of the chest region varies for different individuals, and the positioning of the body when taking a CT scan also varies. In Figure 1.8, the variation in lung size can be clearly observed for different patients. Due to variation in scanning position, the body in the right image appears to

be positioned higher in the axial view. Further, the image in the center shows the lung region closer to diaphragm when compared to the other two, which may be due to the size or position variation. Even for a same individual, CT scans taken at different times are likely to show variation in patient position.

A robust CFOR scheme must be able to normalize the variation in patient size and scanning position. In other words, a CFOR scheme needs to provide a common framework for mapping between a given chest CT scan and the CFOR space. This work focuses not only on establishing a robust CFOR scheme for the chest region but also on automated mapping between a given CT scan and the CFOR space.

From a CT scan, one or more robust landmark structures must be extracted and used to map from the CT image space to the CFOR space. The bone structures are the most rigid part in human chest and may serve as a solid baseline reference for a CFOR scheme. There are several different bone structures within a human chest, including vertebrae, ribs, sternum, and scapula. The rib cage surrounds the entire lungs and could potentially be used to define a robust CFOR.

1.2 Literature review

There have been much interest on automated analysis from CT scans in the past. This section summarizes the literatures from past 15 years that are related to this research. The previous literatures are presented in four categories: segmentation of airways, segmentation of bone structures, quantitative analysis of airways, and registration of CT images.

1.2.1 Analysis of intrathoracic airways

The previously proposed growing-based segmentation algorithms used different techniques to avoid leakages [22, 42, 49, 90, 91]. Graham et al. [22] and Ginneken et al. [91] proposed the methods that first segments the main branches conservatively and expands further into smaller branches. Tschirren et al. [90] and Kitasaka et al. [42] proposed the segmentation algorithms that consider small regions of interest to avoid leakage into lung parenchyma. Their algorithm used 3D region growing technique within local regions which are established around small section of an airway segment. Lo et al. [49] proposed the method that uses voxel features along with the voxel intensities to classify a given voxel.

Another variation of the airway tree segmentation algorithm is based on airway morphology which was proposed by Aykac et al. [1]. Their algorithm first performs grayscale morphological closing operation and thresholding in order to find airway lumen candidates from individual 2D image slices. The entire tree is reconstructed from the candidates using slice-by-slice forward pass to join the appropriate candidate regions and detect bifurcations. The backward pass is used to reconstruct the branches in the upper lung lobes that are directed upward. The algorithm was evaluated by comparing the segmentation to the expert-edited segmentation, and the authors report that the overall detection sensitivity was 73%.

Kiralry et al. [37] compared the performances of growing-based and morphology-based algorithms and studied the hybrid method that employs both region growing and mathematical morphology. The authors further studied the effect of 3×3 median filter on the segmentation outcome. The authors states that the growing-based method is the fastest method, while the morphology-based method is less prone to leakages. The proposed hybrid algorithm reduced the segmentation time compared to the morphology-

Table 1.2: Datasets to evaluate airway segmentation algorithms (* average resolution is reported, n/a indicates that the information was not available from the paper.)

Primary author	Number of Scans	Scan resolution (mm)	Dose
Kiraly	30	0.62×0.62×0.60 *	120 kVp, 100 mAs
Aykac	8	0.59×0.59×3.00	n/a
Kitasaka	3	0.59×0.59×2.00 *	n/a
Tschirren	22	0.68×0.68×0.60	120 kVp, 50 mAs
Graham	40	0.67×0.67×0.50	n/a (MDCT)
van Ginneken	150	n/a	1 mGy, 3mGy, 10mGy
Lo	20	0.78×0.78×1.00	low dose

based method. The authors concluded that neither growing-based nor hybrid method is superior over another, but the growing-based method was more robust when the CT image is pre-processed with a 3×3 median filter.

Since the different papers evaluate the algorithms using different datasets and evaluation metrics, it is difficult to compare different algorithms. Further, some information about the dataset are often not reported in the publications. The datasets used by seven different publications are shown in Table 1.2. The datasets vary in number of scans used, scan resolution, and radiation dose used to take the scan. To address this issue, Lo et al. [48] organized an airway segmentation challenge, EXACT09, with the goal of comparing the results of various algorithms for extracting the airway tree from chest CT scans using a common dataset and performance evaluation method.

Most works on automated measurement of intrathoracic airway focused on the measurement of lumen diameter, wall thickness, or both [38, 55, 60, 61, 64, 74, 79, 96].

To measure lumen diameter and wall thickness of an airway, it is necessary to determine the precise location of inner and outer wall boundaries. The full-width at half-maximum (FWHM) principle has been widely used to determine where the boundary is located [56, 78]. However, it has been shown that FWHM over-estimates the wall thickness and under-estimates the lumen diameter, and many have attempted to improve accuracy of the airway measurements [12, 64, 74].

Wood et al. [96] proposed a method to segment the airway tree and measure the diameter of individual branches, which was validated using two phantom airway trees. Reinhardt et al. [74] presented a measurement method to overcome the limitations of the traditional FWHM approach. The proposed approach was validated using plexiglass phantoms oriented axially on 2D image slices. Park et al. [64] proposed a wall thickness measurement algorithm using deconvolution with a point spread kernel, which was validated using tube phantoms of different sizes.

There have also been some interests on measuring other quantities such as airway length [1] and bronchoarterial diameter ratio [36, 95]. Aykac et al. [1] measured the lengths of airway segments using repeat scans of an individual. Wiemker et al. [95] proposed an automated method to find the pulmonary artery based on the airway position and compute a bronchoarterial diameter ratio.

The validation of automated measurements is often limited to CT scans of plexiglass phantoms with known dimensions [64, 74, 96]. The phantom images are used since it is very difficult to establish manually-measured ground truth for airways. While phantom images provide means to assess the accuracy of the automated measurement, they do not resemble complex airway surroundings that are seen in the actual CT images, such as adjacent structures and scan noise.

1.2.2 Segmentation of anatomical structures

There have been considerable interest in developing algorithms for bone segmentations from medical images. There are two broad categories of the bone segmentation methods: deformable model based methods [17, 43, 46, 50, 81, 84] and growing based methods [29, 39]. The methods that use deformable models construct the bone appearance model and set up the cost function to be optimized, while the growing based methods first extract a seed region and grows into the entire bones.

Many have proposed the algorithms to segment bones from CT scans of chest [43, 84, 86]. Staal et al. [86] presented a method to segment and label individual ribs in CT. Their method first identified image primitives and constructed rib centerline, from which The full ribs were then grown. Klinder et al. [43] used a rib cage model constructed from their training set. Their algorithm then detected the centerlines of the ribs in a CT image using the pre-established model. Shen et al. [84] introduced a rib tracing algorithm using dynamic programming based on the geometrical shape of the ribs. Kiraly et al. [39] proposed a tracing based visualization of ribs. Their method traced the centerline of each rib and performs straightening of individual ribs to aid the visualization of the ribs.

In related work, others have proposed algorithms to segment bone structures from CT scans of lower body. Kang et al. [29] applied 3D image techniques to segment the proximal femur in CT data. Their method used 3D region-growing with local adaptive threshold followed by morphological operation to obtain the segmentation. Lamecker et al. [46] proposed an automated algorithm to segment the pelvic bone using a statistical shape model built from a training dataset.

The bone segmentation has also been explored in other modalities such as magnetic resonance imaging (MRI). Many have studied the segmentation algorithms for MR im-

ages of the knee [17, 50, 81]. Fripp et al. [17] proposed a semi-automated algorithm to segment the articular cartilages. Lorigo et al. [50] used a method based on active contour model to segment the tibia and femur. Schmid et al. [81] proposed a method to segment hip and femur bones from clinical MR images using deformable models and shape priors.

1.2.3 Standardized frame of reference

The CT scans taken at different times are likely to have variation in scale and position. The registration process aligns multiple images into a common grid and can help clinicians when planning a surgery and allows for monitoring of a feature across the images.

Many have studied the algorithms to perform registration of CT images taken at different times [7, 31, 80, 82]. Coselmon et al. [7] proposed a registration method for sequential CT scans that uses the selected control points and iterative alignment process. Sarrut et al. [80] performed a deformable registration using second-order gradient to align a CT scan pair acquired at different breathing stages. Shekhar et al. [82] presented a phase-to-phase non-rigid registration algorithm for 4D CT scans, where the contour of a structure of interest on one phase is provided by an expert and used for automatic segmentation in other phases. Kaus et al. [31] proposed a registration method based on the deformation of organ surfaces and evaluated its accuracy using anatomical landmarks.

The technique that is closely related to the presented CFOR scheme is the segmentation-based registration, where anatomically the same structures are extracted from both images to be registered and used as sole input for the alignment procedure [51]. While there has not been much work for a standardized frame of reference for the entire chest region, there were considerable interest in the registration of a local

region of interest such as pulmonary nodule across multiple image data [4, 32, 85]. Shi et al. [85] developed an automated method to identify matching nodules in serial chest CT scans. They performed the initial registration using the rib centerlines followed by a 3D rigid transformation to fine-tune the registration of the local nodule region. Betke et al. [4] proposed an automated method for registering lung nodules in serial chest CT scans using detected anatomical landmarks and surface alignment of lungs. Kawata et al. [32] presented a method to register pulmonary nodules from chest CT data. They used the rigid transformation of the scans followed by affine transformation of the local region of interest including the nodule using normalized mutual information as a similarity metric.

Positron emission tomography (PET) is an imaging technique that is used to monitor biochemical or metabolic activities in the body. When visualizing a PET image data it is important to perform a registration with a X-ray CT image so that a physician can determine where exactly the observed activities are originated. There have been many interests in performing and evaluating registration of PET and CT images [6, 21, 24, 54, 63, 83]. Shekhar et al. [83] developed an automated method to align whole-body PET and CT images. They used normalized mutual information to perform elastic image registration by interpolating multiple rigid-body registrations. Mattes et al. [54] presented an algorithm for PET-to-CT registration in the chest with mutual information as a similarity metric. They used a rigid-body deformation along with localized cubic B-splines to align the images.

1.3 Overview of chapters

In the following chapters, three main aspects of automated analysis are presented:

1. Analysis of intrathoracic airways - The method for automatically assessing clinically-relevant measures of airways was developed, and the measurement precision was quantified. The airway measurements have been correlated with other measures used in clinical practice.
2. Segmentation of anatomical structures - The algorithms to automatically identify shape and location of the main anatomical structures visible in chest CT images were developed. The algorithms were evaluated using a large dataset composed of low-dose CT images.
3. Chest frame of reference (CFOR) - A common chest grid was established using skeletal structures. The established CFOR was used to study spatial variation of anatomical points among different patients and register points of interest across intra-subject scans, as well as to establish a population norm.

CHAPTER 2

ANALYSIS OF INTRATHORACIC AIRWAYS

In this chapter, the algorithms to segment the airway tree and measure individual airway branch are presented. The methods for measuring airways using a single CT scan as well as for comparative measurements using multiple scans of same subject are discussed. Quantitative experiments have been performed for validating precision of the automated measurement and correlating airway dimensions to the pulmonary function test (PFT) scores.

This chapter is organized into four main sections:

1. Airway tree segmentation - The airway tree is segmented from a given CT scan using the algorithm designed to avoid segmentation leakage.
2. Measurement of airway branches - Individual segments are identified from the segmented airway tree, and lumen diameter (LD) and wall thickness (WT) are measured for each segment.
3. Segment matching for comparative measurements - The corresponding airway segments are identified from multiple scans of a same patient, which allows for assessment of airway dimension change over time.
4. Quantitative experiments - The precision of the automated airway measurement is quantified, and the measurements are correlated to PFT scores.

2.1 Airway tree segmentation

The segmentation of the airway tree is the first step toward the automated airway measurements. An illustration of the airway tree segmentation from a CT scan is shown in

Figure 2.2. Segmenting the airway tree conservatively by minimizing leakage is important for subsequent analysis of airways since any analysis based on a false segmentation is undesirable, as discussed in Section 1.1.2.

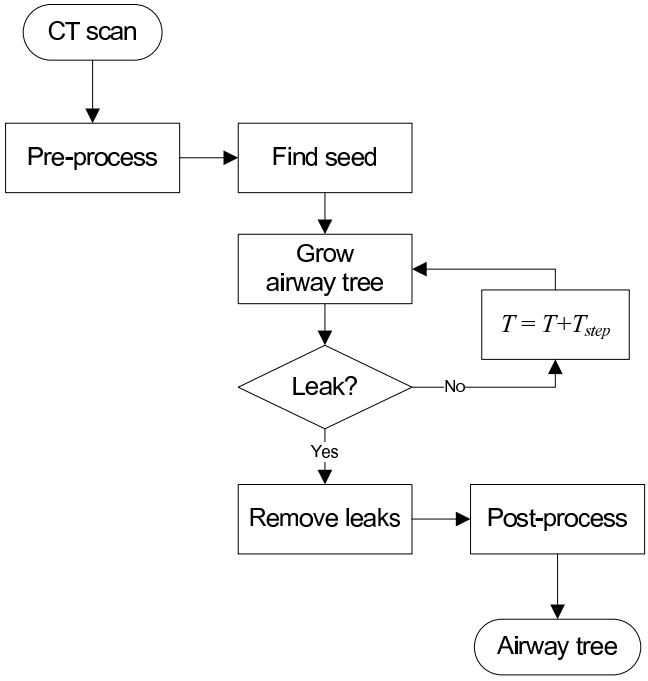

Figure 2.1: Flowchart for airway tree segmentation. The tree is grown from the automatically-identified seed point, and the optimal threshold is found by incrementing until a leak is detected. The locally detected leaks are removed from the final segmentation outcome.

2.1.1 Airway segmentation algorithm

The airway tree segmentation algorithm includes four main stages and is shown as a flowchart in Figure 2.1. First, a seed point from which a growing process is identified. Second, individual airway branches are grown within local envelopes starting from the trachea. The threshold for growing is incremented until a leak is detected, and the grown region corresponding to the leak is removed from the final segmentation output. The

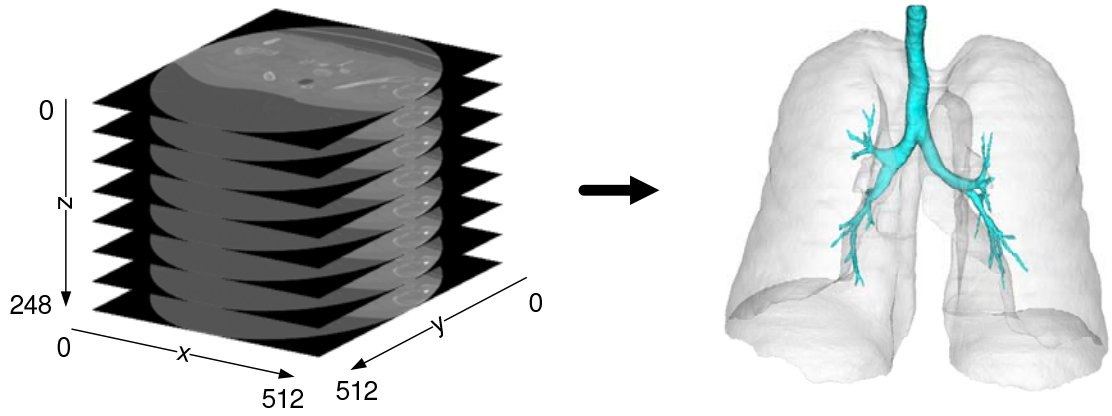

Figure 2.2: 3D visualization of airway segmentation. The airway tree is segmented from a 3D CT image and rendered together with the lung.

concept of local growing has been proposed by others previously [42, 90]. The major contributions of this research was on the leak detector.

The proposed algorithm performs segmentation in a conservative manner to prevent leakage into the lung parenchyma. When conservative local growing fails to avoid a leak, the second level of leakage prevention is carried out using a local leak detector. The low leakage level was achieved by using such a conservative segmentation approach.

Pre-processing

Each slice in a given CT scan is pre-processed with 3×3 median filter to reduce noise. The median filter increases the robustness of the segmentation algorithm at a cost of reduced sensitivity for the small airway branches [37]. The median filter eliminates image noise without creating new image intensity or blurring the image [88]. An $N \times N$ median filter transforms an image to the median intensity of an $N \times N$ region around each

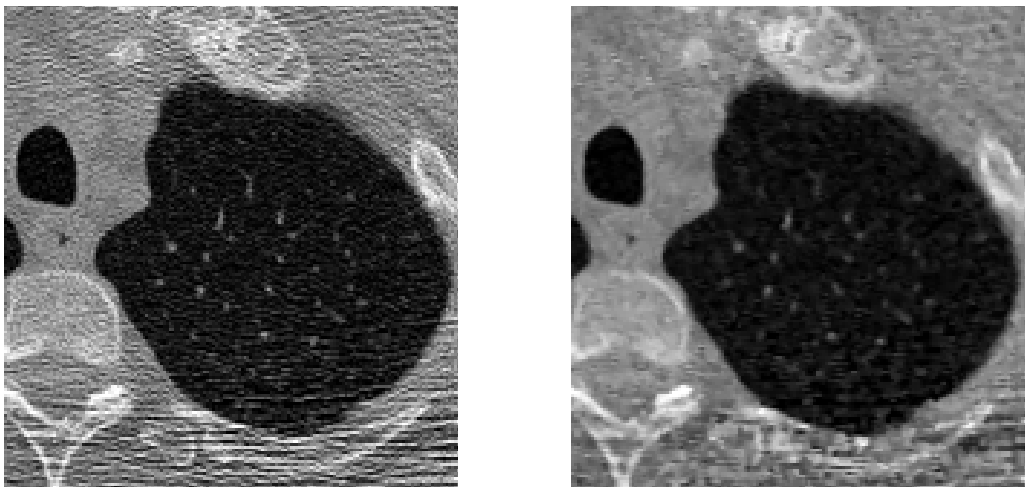

(a) (b)

Figure 2.3: Effect of median filter. An axial image before (a) and after (b) applying 3×3 median filter. The images are zoomed to the region around the left lung to better show the effect.

pixel:

$$m(I(x,y)) = median(K_{x,y}), \tag{2.1}$$

$$K_{x,y} = \{\ I(i,\ j) \quad | \quad x-N/2 \le i \le x+N/2,\ y-N/2 \le j \le y+N/2\ \}, \tag{2.2}$$

where $I(i, j)$ is the image intensity at (i, j).

Tree segmentation framework

The algorithm was designed to segment a single branch in each iteration. Using such a framework allows for a control over the depth of the airway tree to be segmented. Further, the outcome of the segmentation may be represented as a whole airway tree or as a set of labeled branches.

An illustration of the framework is shown in Figure 2.4. Within this framework, each branch in the airway tree is represented as a node with the pointers to its parent and

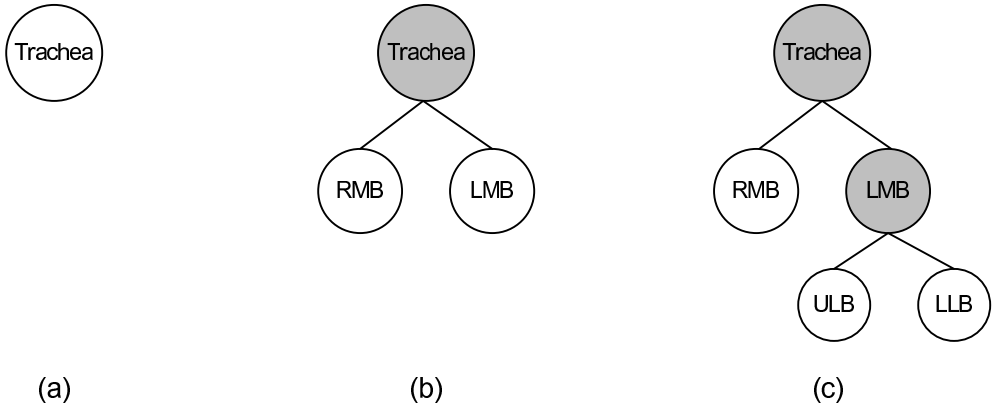

Figure 2.4: Framework for airway tree segmentation. Each node represents an airway branch, and the state of each node is shown with the colors. The white nodes are in "open" states, and the gray nodes are in "closed" states. Three iterations of the segmentation is shown. (a) The segmentation is initiated with a trachea, an open node. (b) The trachea is segmented, and two open nodes, for right main bronchus (RMB) and left main bronchus (LMB), are created. (c) The LMB is segmented, and two children nodes are created.

children, if any. Each node may be in one of two states, "open" or "closed". A node is in an open state when it is first created, meaning that the segmentation is not completed for the given branch. When the segmentation is complete (i.e. an end point or a bifurcation point is detected), the current node is closed, and if necessary, the child nodes are newly allocated with open states.

The growing process searches for any open node and performs segmentation on the corresponding branch. The program terminates when there are no more open nodes. Following airway segmentation airway analysis may proceed by measuring parameters of each detected airway segment.

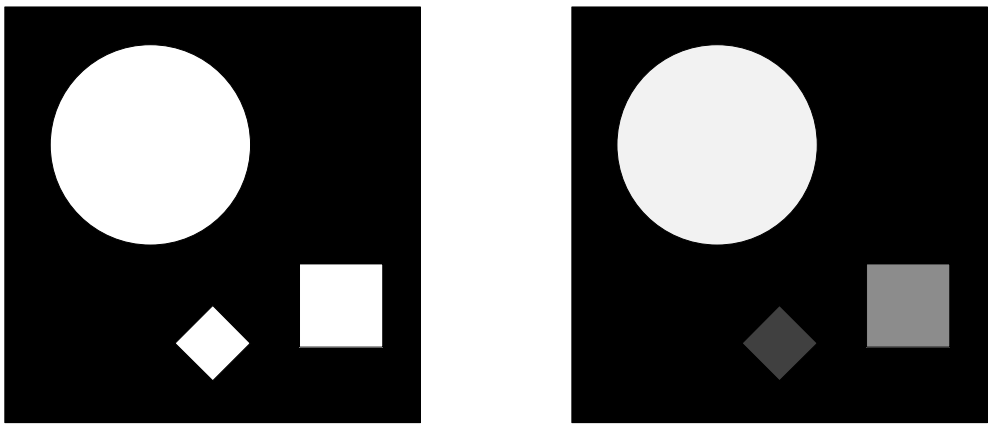

Figure 2.5: Illustration of connected component analysis. An input binary image (a) is analyzed to find connected region, and each region is given an unique label after performing connected component analysis (b).

Seed point detection

The airway tree segmentation begins by growing the trachea lumen from a seed point. The seed point is identified by locating a point within the lumen of the trachea which should be relatively centered on an axial image and appear in low intensity. The lumen of the trachea is identified using thresholding and connected components analysis.

Thresholding of an image is a process of selecting a subset of image pixels using their intensities. The thresholding is often used to distinguish the image regions with high contrast in the intensities. The outcome of the thresholding is a binary image containing zero and non-zero pixels. The image thresholding is defined as:

$$t(I(x,y)) = \begin{cases} 1, & \text{if } I(x,y) \geq Threshold \\ 0, & \text{if } I(x,y) < Threshold \end{cases} \tag{2.3}$$

Connected component analysis is commonly-used technique to identify and label each connected region within the image [75]. An example of connected component

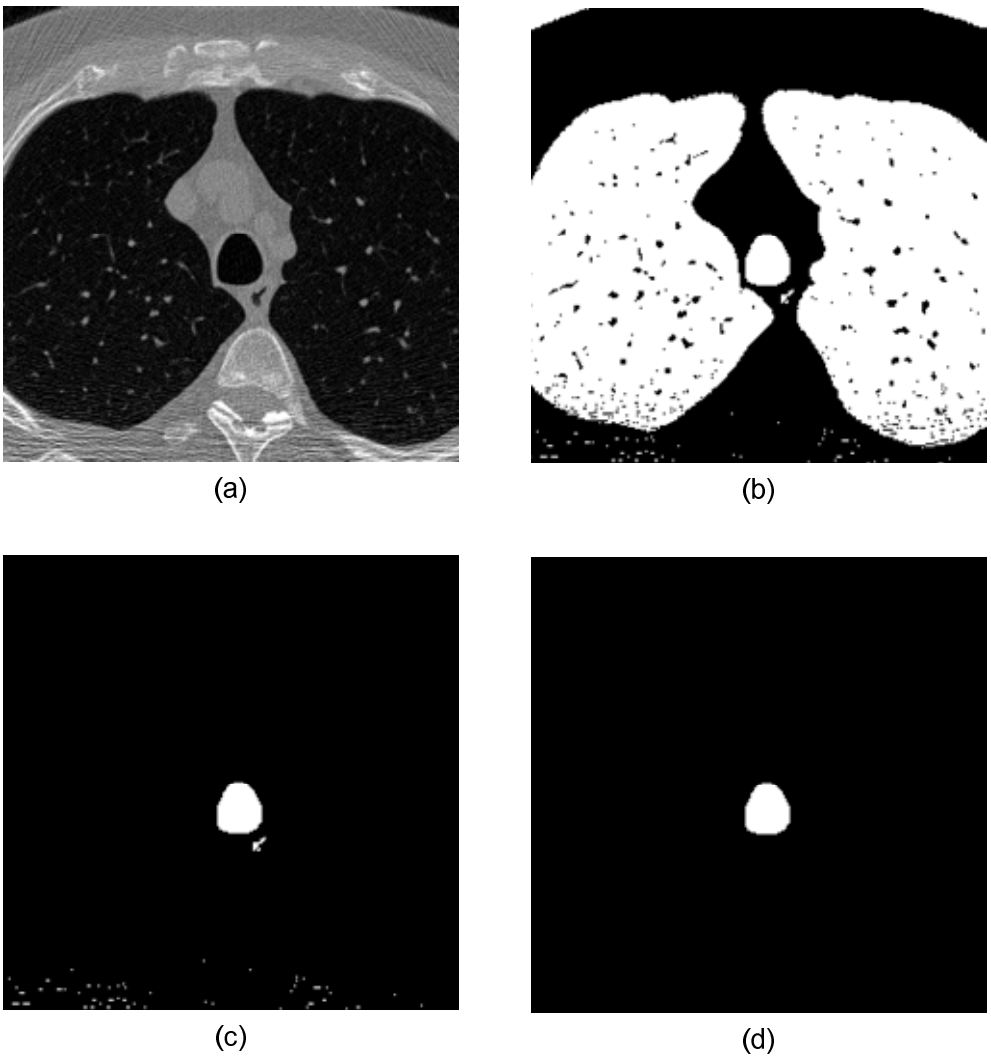

Figure 2.6: Seed point detection. The images at different stages are shown: (a) the clipped region of the CT image. (b) the image after thresholding and negating at -600 HU. (c) the image after performing connected component analysis and border-touching component removal. (d) the largest region among the remaining components.

analysis on a binary image is shown in Figure 2.5. Connected component analysis is useful for eliminating small voxels remaining after performing threshold-based segmentation, as high-intensity noise pixels captured by the thresholding often appear in small volumes.

The algorithm to find a lumen region within the trachea lumen is as follows:

1. Take a 2D image slice at d below the highest image.
2. Clip out the $n \times m$ central region of the image (Figure 2.6a).
3. Threshold the image at T to obtain a binary image and negate (Figure 2.6b).
4. Perform connected component analysis.
5. Remove any labeled regions that are touching the image border (Figure 2.6c).
6. Take the labeled region with the largest area (Figure 2.6d).

The outcome of the segmentation will not be affected as long as the selected image slice is above the tracheal bifurcation point. However, setting d too small may result in selecting an axial image where trachea lumen appears very small. The value of d was set to 50 mm. The clipping parameters n and m were set to half of x and y dimensions, respectively, as these values will robustly give images clipped through the lungs. For the images in our dataset, which had the dimensions of 512×512, n and m were set to 256. The threshold T was set to -600 HU [72] to separate regions between densities of soft tissue and air.

Once the lumen is identified on an image, the center of mass is computed and used as a seed point for airway tree growing. The center of mass $(\bar{x}, \bar{y})$ of a binary image can be found using first order moments:

$$\bar{x} = \frac{m_{1,0}}{m_{0,0}}, \tag{2.4}$$

$$\bar{y} = \frac{m_{0,1}}{m_{0,0}}, \tag{2.5}$$

where a moment $m_{p,q}$ for an $N \times M$ image I is defined as:

$$m_{p,q} = \sum_{y=0}^{M-1} \sum_{x=0}^{N-1} x^p \, y^q \, I(x,y) \tag{2.6}$$

Local growing of individual branches

Starting from the detected seed point in the trachea, each airway branch is grown using region growing. Region growing is a technique to segment a region of interest that requires an initial selection of a seed point. Adjacent voxels are iteratively added to the region with the constraint that the voxels in a grown region must satisfy homogeneity criteria which were selected conservatively to prevent the leakage into lung parenchyma as much as possible.

A simple threshold-based connected component analysis would have a homogeneity criterion based only on the voxel intensity. In other words, a voxel is iteratively added to the region if and only if the following conditions are met:

- The voxel is connected to the grown region using 26-connectivity.
- The voxel has an intensity below threshold T.

An example of a segmentation outcome when using the growing criteria described above, with T = -900 HU, is shown in Figure 1.4. If a simple threshold-based region growing is used to segment the airway tree, the segmentation would be vulnerable to the leakage into parenchyma region since only a given voxel's intensity of the grown region are considered.

The growing algorithm was designed to provide a first level of leakage prevention. A leakage is typically caused by the gap in the airway wall through which voxels are grown into the lung parenchyma. Such a gap may exist in a CT due to the image noise in low-dose scans, especially for the small airways with thin walls. An illustration of an airway with a small gap in the wall is shown in Figure 2.7. It has been observed that the voxels growing through the gaps are more likely to be surrounded by the airway wall

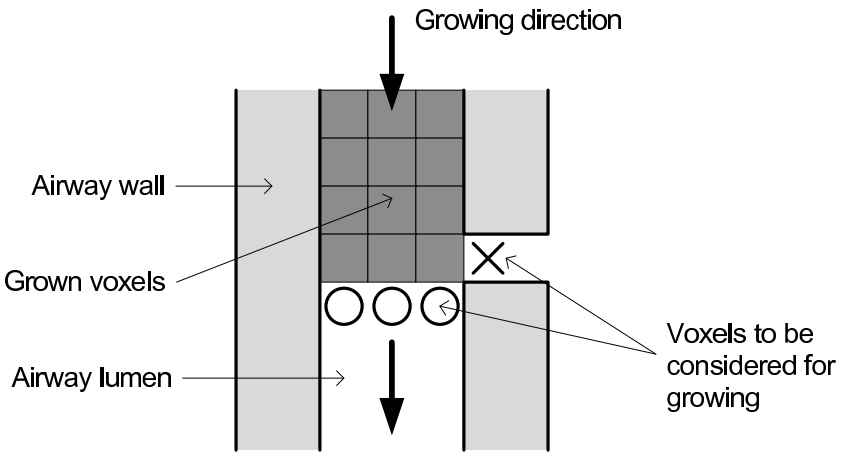

Figure 2.7: An illustration of a gap in airway wall.

than the voxels within the lumen. To prevent the growing algorithm to leak through the small gaps, an additional homogeneity criterion was added that uses the intensities of neighboring voxels.

The homogeneity criteria for our region growing algorithm is as follows:

- The voxel is connected to the grown region using 6-voxel connectivity.
- The voxel has an intensity below threshold T, which is adaptively selected for each scan.
- At least $(\gamma \cdot 26)$ of its 26 neighbors have intensities below T.
- The voxel is within a localized cylindrical volume [42, 90].

The value of γ was determined empirically using the training dataset. For airway segmentation, a reasonable leakage suppressions were observed for $\gamma = 0.5$. The growing is performed within a localized cylindrical volume that is advanced iteratively along the branch. The concept of the localized growing is similar to the methods proposed by

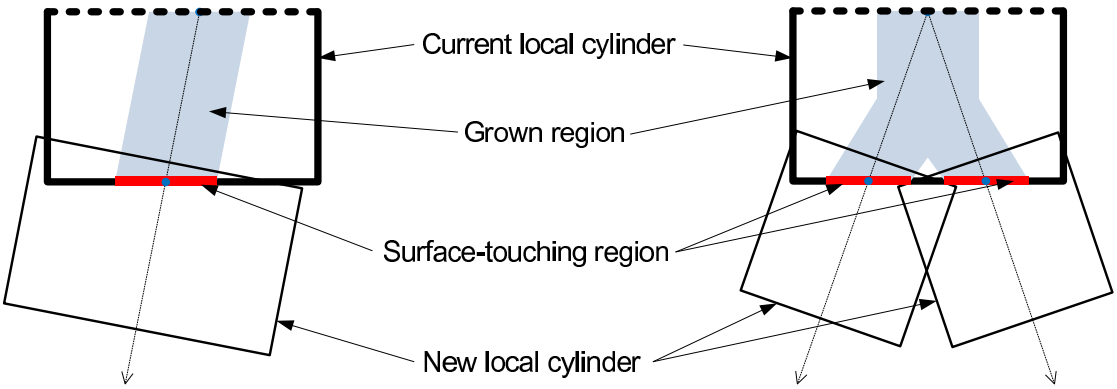

Figure 2.8: 2D illustration of establishing new local cylinders. The direction of the a new cylinder is determined based on the center of mass of the surface-touching region. The left and right figures show examples of $n = 1$ and $n = 2$, respectively.

Tschirren et al. [90] and Kitasaka et al. [42]. The growing of the current airway branch is terminated when the branch has ended or a bifurcation is detected.

As the airway lumen is grown within the localized cylinder, the number of grown regions n that intersect the surface of the cylinder is counted, excluding the surface from which the growing was initiated (shown in Figure 2.8 as bold dotted line). There are three possible states of the current airway segment depending on the value of n:

- $n = 0$: the current airway segment has ended,
- $n = 1$: the current segment is not yet fully grown,
- $n > 1$: a branch point is detected.

When $n \neq 1$, the current segment is fully grown and the growing process terminates for the current airway branch. Figure 2.8 illustrates how new local volumes are established when $n \geq 1$. The direction of the new cylinder is determined by connecting the center of masses of starting region and ending surface-intersecting region.

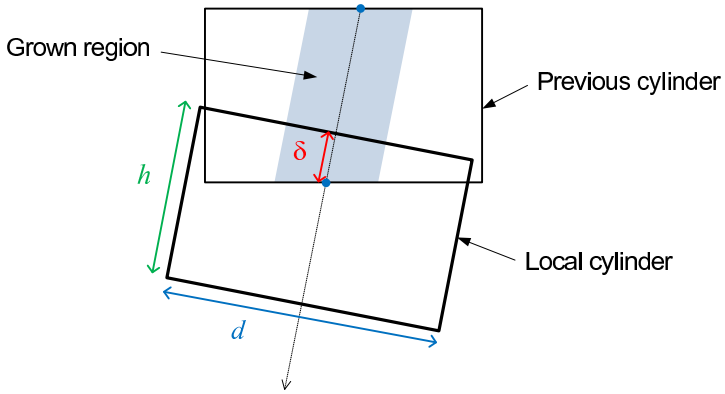

Figure 2.9: Cylinder parameters. The parameters δ, d, and h determine the size and placement of the local cylinder.

The parameters for a local cylindrical volume are shown in Figure 2.9 which include the following:

- d - the diameter of current cylinder
- l - the length of current cylinder
- δ - inter-cylinder overlap

The parameters d and l specify the dimension of the local cylinder. The starting point of a new cylinder is shifted backward by δ as shown in Figure 2.9. This offset is introduced in order to eliminate a gap between two subsequent cylindrical volumes. The cylinder parameters were empirically determined using the training dataset which is explained further in Section 2.1.2.

Leak detection

The leakage detector was designed to identify leakages within a localized cylinder using two main observations of typical leakage:

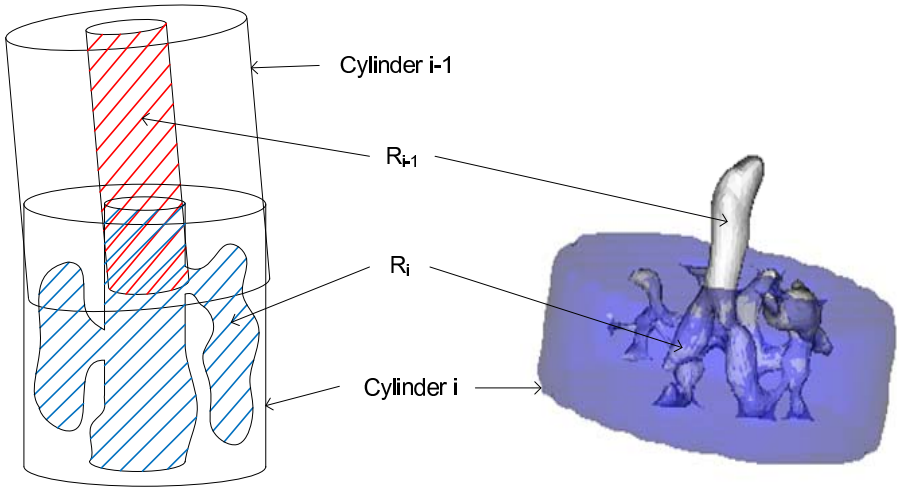

Figure 2.10: An example of a leakage detectable using increased volume. An illustration of the leakage is shown on the left, and a 3D rendering of an actual example is shown on the right.

1. The volume of the grown region increases abruptly when compared to the previous volume.
2. The grown region fills up the local cylindrical envelope, and there is a large area of contact between the grown region and cylinder's surface.

Most leakages can be detected within local cylindrical envelope using change in grown volume from the previous iteration. This common type of leakage is shown in Figure 2.10. However, the volume-based leak detection may fail when the volume change occurs gradually through several iterations. In such a case, the leaked region will eventually fill up the local envelope and continue growing in successive iterations as shown in Figure 2.11. In order to prevent this catastrophic situation, a second measure of leakage detection was added using the surface area of the grown region.

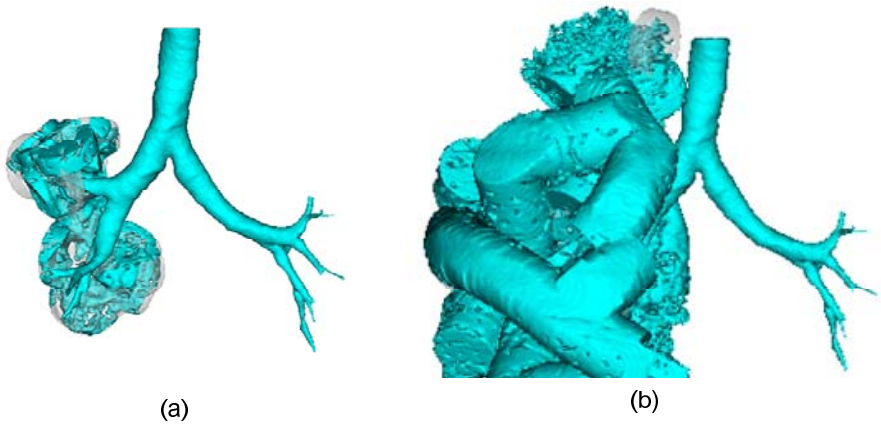

Figure 2.11: An example of a leakage detectable using surface area. The segmentation outcomes are shown for the situations where: (a) both volume-based and area-based leak detections were used (leakages detected and no further growing was allowed) and (b) only volume-based leak detection was used (leakage not detected and growing continued). The transparent cylinders indicate the iterations where the leakages have been detected. For illustration purpose, the images show the segmentation outcome before removing the detected leakages.

Specifically, the following criteria are used to classify a grown region R as a leak or non-leak:

$$R = \begin{cases} \text{Leak}, & \text{if } Vol_i > \beta \cdot Vol_{i-1} \\ \text{Leak}, & \text{if } Area_i > \alpha \cdot Area_{cylinder_i} \\ \text{No leak}, & \text{otherwise}, \end{cases} \tag{2.7}$$

where r and h are the radius and height of the local cylinder, $Area_i$ is the area of the region intersecting the surface of the cylinder, and Vol_i is the volume of the grown region in current iteration. The values of α and β were determined based on the leakages observed in the training data.

A locally grown region that is identified as leakage is removed from the final segmentation as shown in Figure 2.12. The leak removal is performed by unsetting all

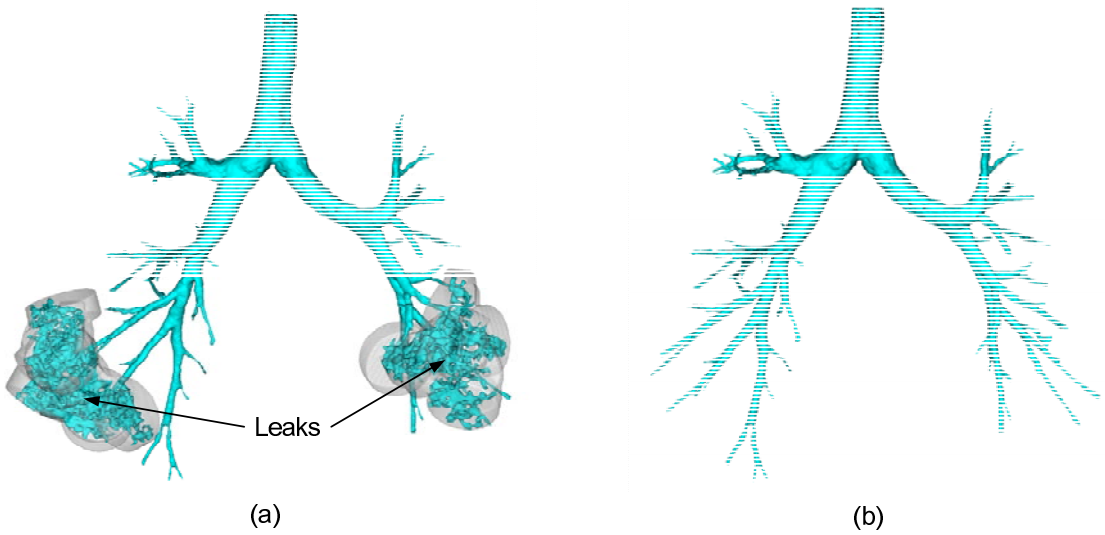

Figure 2.12: Removal of segmentation leaks. (a) The coronal visualization of the airway tree before removing the leaks (grown with the final threshold). The leaks are only allowed within the local cylinders. (b) Airway tree after removing all detected leaks.

grown voxels in the cylindrical volume.

Setting T high would result in a segmentation with high sensitivity at the expense of more leakage. To optimize the segmentation outcome, the threshold value is incremented until at least one leak is detected. The threshold T for growing is initially set to -950 HU, and incremented by T_{step} which was set to 5 HU. The initial threshold value was empirically determined using the training cases.

Post-processing

The lumen area segmented using local 3D region growing may contain some artifacts. The objectives of the post-processing step is to:

1. Fill in the voids enclosed in the segmentation.

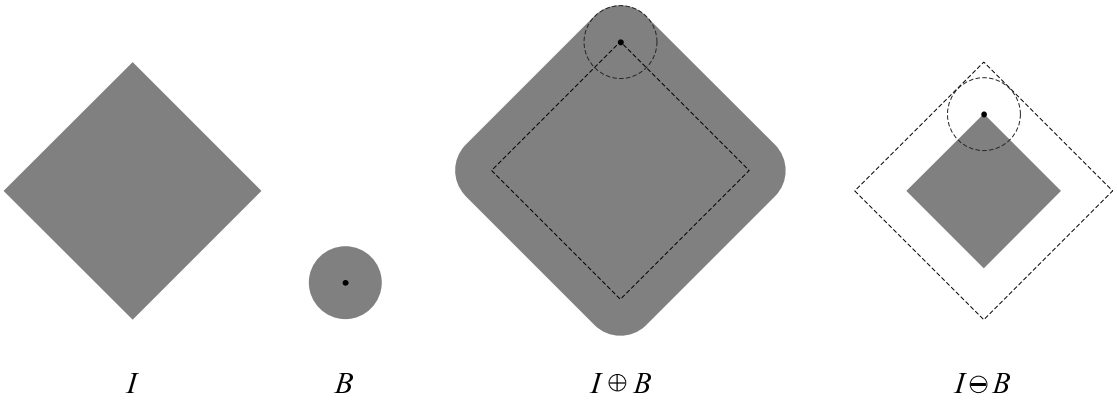

Figure 2.13: 2D illustrations of morphological dilation and erosion. For a binary image I and structuring element B, the outcome of dilation $I \oplus B$ and erosion $I \ominus B$ operations are shown. For illustration purpose, the borders of I and B are marked with the dotted lines on the outcomes.

2. Smooth the rough surface of the grown region.

The morphological operations are used to refine the binary outcome of the segmented airway tree. A binary morphological operation involves a binary image and a structuring element. There are two basic morphological operations: dilation and erosion.

An examples of dilation and erosion operations are shown in Figure 2.13. Given a 3D image I, the dilation and erosion operations are defined as:

$$I \oplus B = \bigcup_{\langle i,j,k \rangle \in B} I_{i,j,k}, \tag{2.8}$$

$$I \ominus B = \{ \langle x, y, z \rangle \mid B_{x,y,z} \subseteq I \}, \tag{2.9}$$

where I is a 3D image data, and B is a structuring element. $I_{i,j,k}$ and $B_{x,y,z}$ are the transitions of I and B, respectively:

$$A_{p,q,r} = \{ \langle i + p, j + q, k + r \rangle \mid \langle i, j, k \rangle \subseteq A \}. \tag{2.10}$$

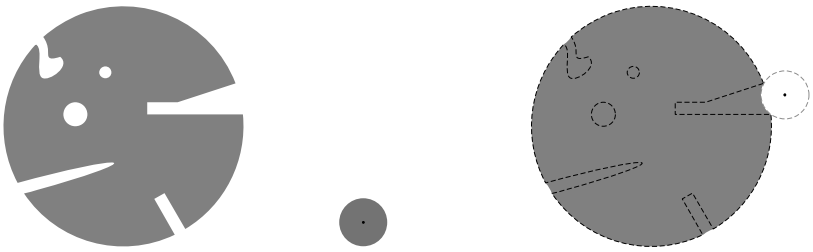

Figure 2.14: A 2D illustration of morphological closing. For a binary image I and structuring element B, the outcome of closing operation is shown. For illustration purpose, the borders of I and B are marked with the dotted lines on the outcomes.

The morphological dilation and erosion may be extended to opening and closing operations. The opening of an image I by B is defined as the erosion followed by dilation:

$$I \circ B = (I \ominus B) \oplus B, \tag{2.11}$$

and the closing of I by B is defined as the dilation followed by erosion:

$$I \bullet B = (I \oplus B) \ominus B. \tag{2.12}$$

An example of performing morphological closing is shown in Figure 2.14. One may think of closing as rolling a structuring element onto the object surface and filling in the space where the structuring element cannot fit into. The closing operation is useful for filling in small gaps and smoothing the object surface and is suitable for post-processing an airway tree segmentation as shown in Figure 2.15. A spherical structuring element with the diameter of 3 voxels was used based on the observation of the irregularities of the grown region in the training data.

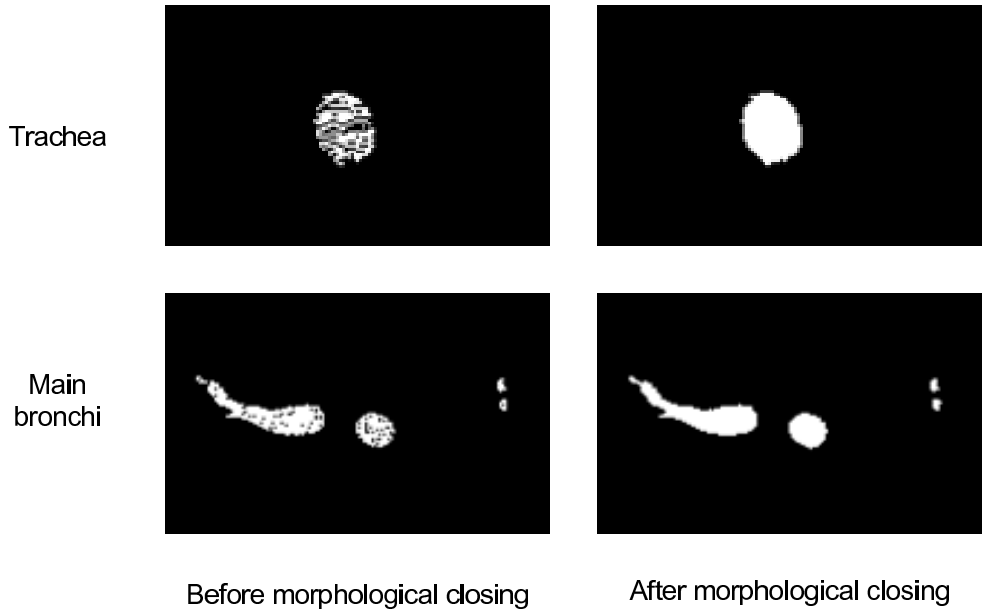

Figure 2.15: An example of performing morphological closing on segmented airways. The axial images of trachea and main bronchi are shown. It can be observed that the irregularities resulting from the intensity-based growing algorithm are smoothed out.

2.1.2 EXACT09: Airway segmentation challenge

In 2009, the airway segmentation challenge, Extraction of Airways from CT 2009 (EXACT09), has been organized as a part of pulmonary image analysis workshop [48]. The main objective of the challenge was to compare different airway segmentation algorithms using a common dataset and performance evaluation metrics. The presented airway tree segmentation algorithm was evaluated as one of 15 entries.

Dataset and evaluation metrics

The dataset provided for the challenge included two sets of 20 chest CT scans, one for training and the other for testing. The training dataset was used to optimize algorithm

parameters, and the testing dataset was used to evaluate the algorithm's performance. The ground truth segmentation for each CT scan in the testing set was established by taking the union of the valid airway branches from the segmentations by all 15 participating teams [48]. However, no ground truth was provided for the training dataset.

The acquisition parameters for the 20 testing cases are reported in Appendix A. The scans were acquired at different sites using different scanners and parameters. The scans were taken from healthy volunteers as well as from patients with mild to severe lung disease and taken at various degree of inspiration and expiration. The radiation dose of the scans ranged from clinical dose to low dose.

The metrics used in the challenge to evaluate the algorithms included the following:

- Branch count - number of segmented airway branches
- Branch detected (%) - percentage of branches detected from the ground truth
- Tree length (cm) - length of the entire airway tree
- Tree length detected (%) - percentage of tree length detected from the ground truth
- Leakage count - number of leakages
- Leakage volume (mm^3) - volume of leakages
- False positive rate (%) - percentage of leakages in the segmentation

Parameter optimization

The parameters for the presented algorithm were optimized using the training dataset. The following five parameters that were defined in Section 2.1.1 were optimized for the challenge:

1. d - diameter of the cylindrical volume
2. l - length of the cylindrical volume
3. δ - overlapping length of the cylindrical volume
4. α - area-based leak detection parameter
5. β - volume-based leak detection parameter

The cylinder's diameter d was that it must be greater than the diameter of airway branch of interest. Based on the training data, d was set to 40 mm for the very first branch (the trachea) and 30 mm for all other branches. Setting d to any greater value should not affect the outcome of the segmentation.

The length of the cylinder l determines how much to advance in each iteration of growing. Small l means that the growing is constrained to smaller local space and is preferred since it would allow for localized detection of leakage. However, d should be proportional to the diameter of the airway for robust placement of new cylindrical volumes. The value of l was varied depending on branch generation. The empirically determined value of l based on the segmentation outcome for the training data were 20 mm for the trachea (1st generation), 17.5 mm for the main bronchi (2nd generation), 15 mm for the 3rd generation bronchi, and 10 mm for the branches with higher generations. The parameter δ is important for eliminating a gap between two subsequent cylindrical volumes. The value of δ was set to a half of the cylinder length l.

The values of α and β have effect on the performance of the leak detection. Smaller α and β values would mean that the leak will be detected with higher sensitivity. These parameters were optimized using the training cases provided by EXACT09. The parameter setting that yielded small number of leakage without sacrificing branch count was selected. The segmentation was performed 20 parameter sets, and the outcomes were

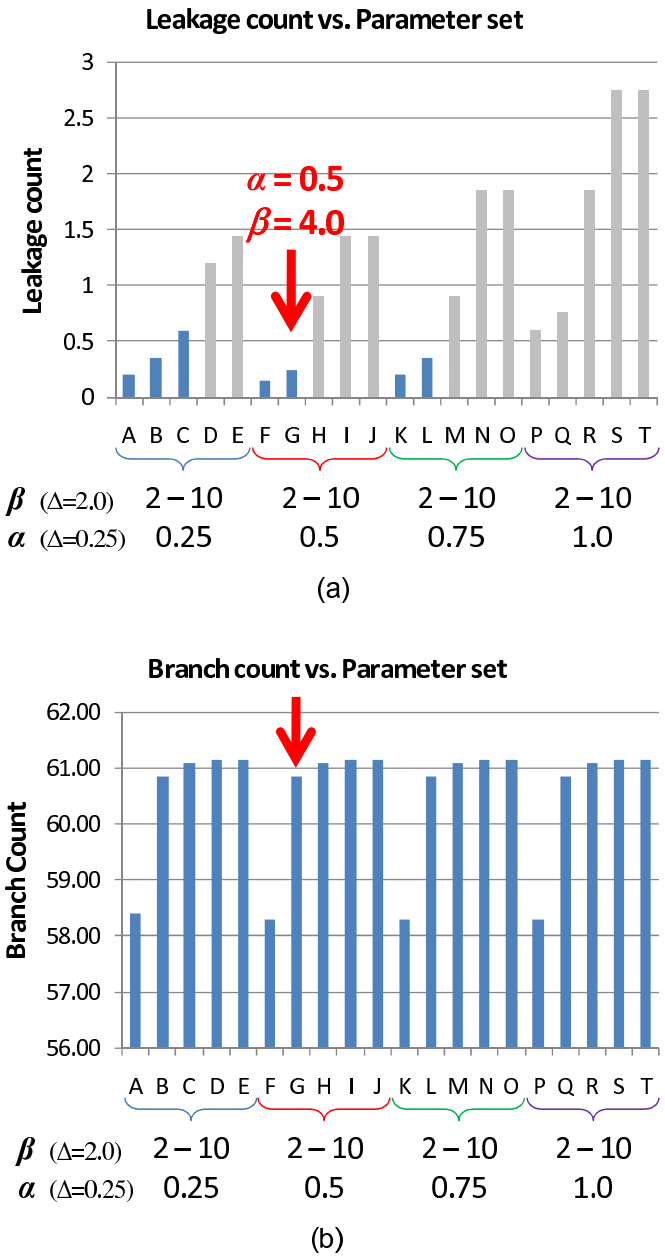

Figure 2.16: Leakage count and branch count using different parameter settings for airway segmentation.

visually inspected for leakage count and branch count. The parameter settings used for optimization are summarized in Table 2.1.2.

Table 2.1: Parameter settings used for optimizing airway segmentation.

Parameter	Description	Range	Δ
α	Area-based leak detection parameter	[0.25, 1.0]	0.25
β	Volume-based leak detection parameter	[2.0, 10.0]	2.0

The leakage count and branch count of different parameter settings are shown in Figure 2.16. The lowest level of leakage was observed with the parameter settings of $\alpha = 0.5$ and $\beta = 2.0$ Between β values of 2.0 and 4.0, less leakages were observed when setting β to 2.0. However, the difference was small, and β of 4.0 segmented approximately 3 more branches per scan. The final algorithm parameters were set to $\alpha = 0.5$ and $\beta = 4.0$.

Results

The algorithm's performance using the evaluation metrics defined by EXACT09 challenge is shown in Table 2.2. On average, the algorithm successfully segmented 79 branches (32.4% of the ground truth segmentation) with the false positive rate of 0.11%. The performance for every testing case as well as the performance of the algorithms submitted by other teams are reported in Appendix B.

The presented segmentation algorithm is fully automated and does not require any user intervention. Once an optimal threshold was found for a given case, the algorithm took less than 30 seconds to process a CT scan on a workstation with Intel Xeon 3.00 GHz CPU.

The examples of the airway trees segmented using conventional region growing method and the proposed method are shown in Figure 2.17. The algorithm was able

Table 2.2: Algorithm performance for the testing dataset.

	Branch count	Branch detected (%)	Tree length (cm)	Tree length detected (%)	Leakage count	Leakage volume (mm^3)
Mean	79.3	32.4	57.8	28.1	0.4	14.3
Std. dev.	51.1	9.6	36.2	8.8	1.0	37.2
Min	31	12.1	20.9	9.7	0	0.0
1st quartile	43	25.9	30.3	21.5	0	0.0
Median	61	32.3	44.1	27.0	0	0.0
3rd quartile	110	38.8	88.1	39.7	1	26.8
Max	221	53.5	150.0	42.0	4	155.2

to segment 79 airway branches for each scan on average, which corresponds to approximately the 6th to 7th branch generations. The number of successfully segmented branches corresponded to approximately one third of the number of branches in the ground truth. While the proposed algorithm may exhibit a low sensitivity, the false positive rate was very low (0.11%). It should also be noted that the number of leakages was less than 1 per scan on average.

2.2 Measurement of airway branches

To perform segmental analysis of airways, individual airway branch must be identified from the segmented airway tree. For the identified branches, the lumen diameter (LD) and wall thickness (WT) are measured.

There are several factors that make automated analysis challenging. First, the airway

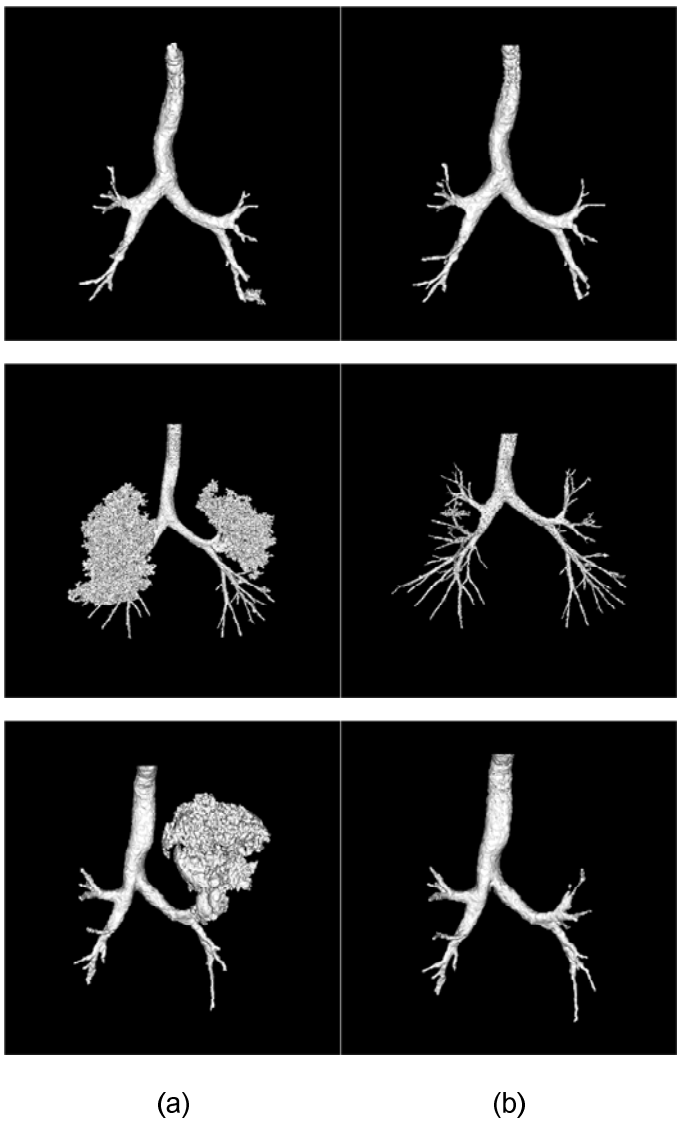

Figure 2.17: Airway segmentation on three cases. The segmentations using a simple threshold-based 3D region growing (a) and the proposed algorithm (b) are shown. The proposed method employs a local leak detector and performs the segmentation with a low leakage level.

segments are curved and appear in various orientations. Due to arbitrary orientation and anisotropy of the 3D image data, every airway branch must first be represented using a common model.

Finally, the high-intensity structures adjacent to the airway, such as pulmonary ar-

teries, may cause over-estimation of wall thickness.

There are four main steps for measuring airways from the tree segmentation:

1. Branch identification - The location of individual airway segment (i.e. start and end points) is identified from the segmented airway tree.
2. Branch model definition - A segment-centric cylindrical model is defined to represent each segment.
3. Intensity mapping - The CT intensities along the segment is mapped to the cylindrical model.
4. Branch measurement - Lumen diameter (LD) and wall thickness (WT) of each segment are measured.

2.2.1 Branch identification

An airway segment can be modeled as a generalized cylinder that best fits the airway lumen, as shown in Figure 2.18. The model was designed with the start and end points as the center of the circles at the both ends of the generalized cylinder. Since the branch structure is connected to one another, we locate the start point of a branch at the end point of the previous branch. An example of the identified start and end points of individual branches are shown in Figure 2.19.

In order to identify branch locations, the segmented airway tree is first skeletonized to give an one-voxel thin-line representation of the airway tree as shown in Figure 2.20. A sequential 3D thinning algorithm is applied to the segmented tree to get an initial skeleton of the airway tree. The algorithm iteratively removes “simple” points from the

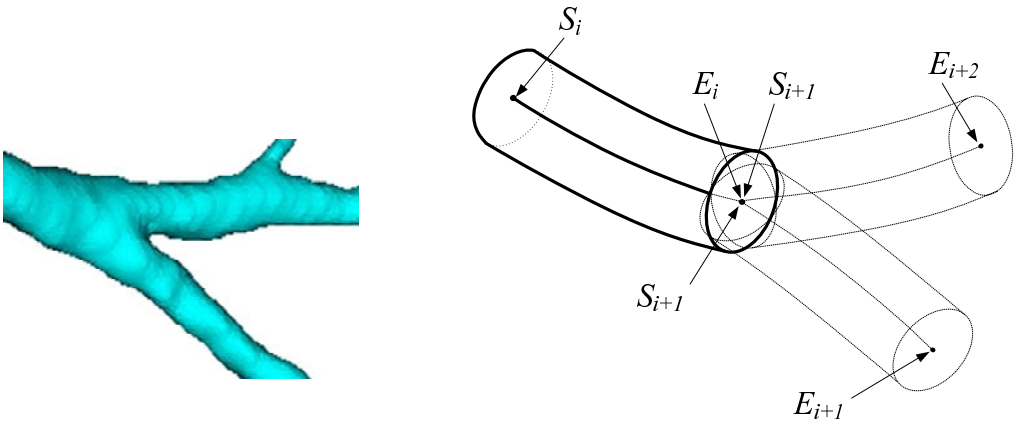

Figure 2.18: Modeling of airways using generalized cylinders. (a) 3D rendering of a posterior basal airway and subsequent airways. (b) An illustration of airway modeling using cylinders. The start point of a subsequent airway is the end point of the current cylinder.

boundary of the airway until a one-voxel line remains. A "simple" point is defined as a point whose removal does not change the topology of an object [3].

The initial skeleton may include spurious false branches that are caused by the fact that the airway lumen is not perfectly cylindrical (i.e. cross-sectional area is not circular) as shown in Figure 2.21a. The thinned tree is post-processed to remove false branches and obtain smooth skeletal lines, as shown in Figure 2.21b. The pruning process is an implementation of the algorithm proposed by Palágyi et al. [62]. It has been shown that this process eliminates the false branches that may exist after performing thinning operation.

The spurious false branches are trimmed using the observation that the tip of a false branch is somewhat embedded in the airway segmentation, while the tip of a true terminal branch does not have too many neighbors that belong to the segmented airway

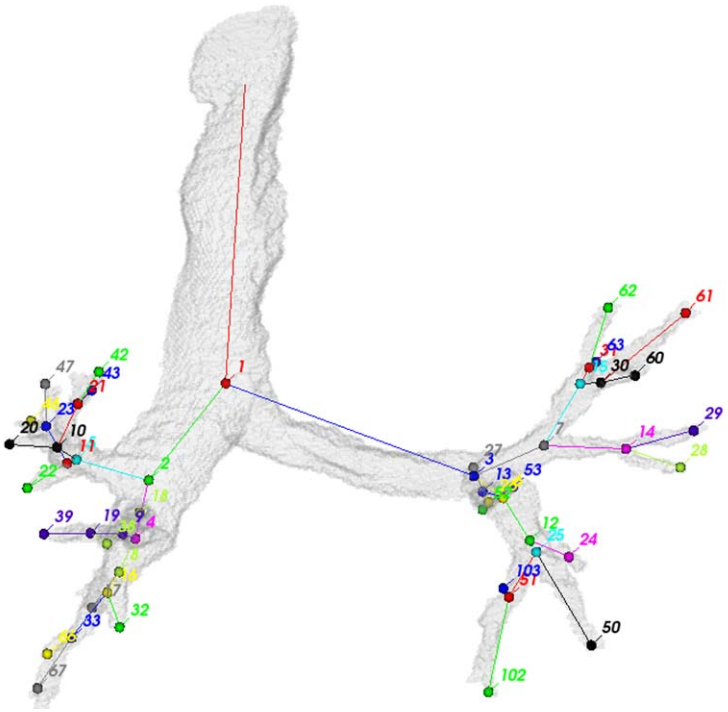

Figure 2.19: Identification of individual branches. For each branch, the start point is labeled with the end point of the previous branch, and the end point is labeled with an unique label for that branch. In thi figure, the start-end points pairs are linked with a straight line.

lumen, as shown in Figure 2.22. First, a set of terminal voxels V is defined as:

$$V = \{ \; v \in S \; | \; |N_v \cap S| = 1 \; \}, \tag{2.13}$$

where S is a set of voxels in the skeletal representation, and N_v is a set of 26-connected neighboring voxels of v. Further, for each voxel $v \in V$, a set of voxels A_v in the airway segmentation A is defined:

$$A_v = \{ \; a \in A \; | \; dist(a, v) \leq d \; \}, \tag{2.14}$$

where $dist(a, v)$ is the distance between two voxel locations. Each voxel $v \in V$ is classi-

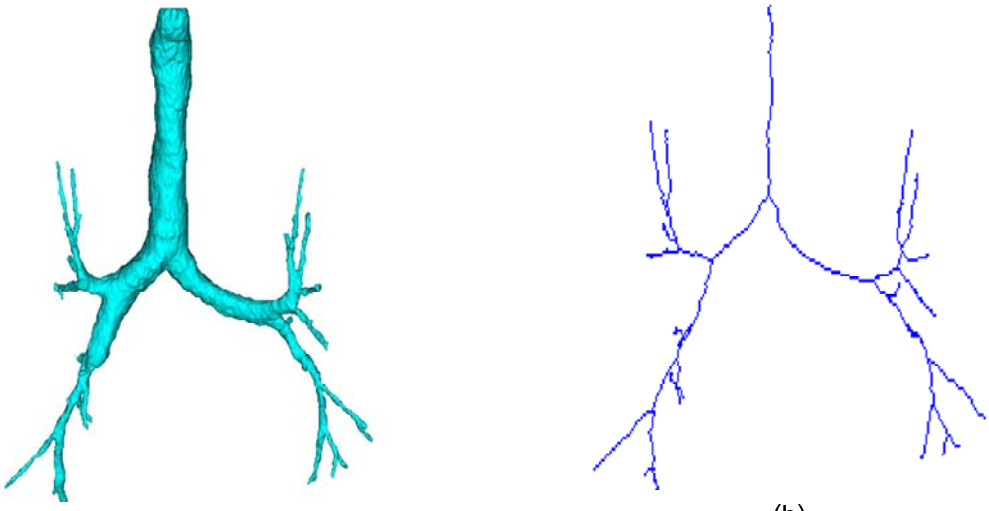

Figure 2.20: 3D thinning of an airway segmentation. (a) Rendering of an airway segmentation. (b) 3D thinning performed on the segmentation.

fied as the tip of the true or false branch based on the number of voxels in A_v:

$$v = \begin{cases} \text{False tip}, & \text{if } |A_v| > \epsilon, \\ \text{True tip}, & \text{if } |A_v| \leq \epsilon, \end{cases} \tag{2.15}$$

v is iteratively removed from the skeleton when it is classified as a false tip, until only true tips remain in V. The values of d and ϵ were empirically determined from five scans and set to 5 and 200 voxels, respectively.

An individual airway branch is identified by traversing a set of voxels S in the skeletal representation of the airway tree. The traversing is initiated at the first voxel of the trachea's skeleton (i.e. the voxel with the lowest z coordinate). With an exception of the first voxel, a voxel $v \in S$ can be classified as a terminal voxel, branch point, or voxel

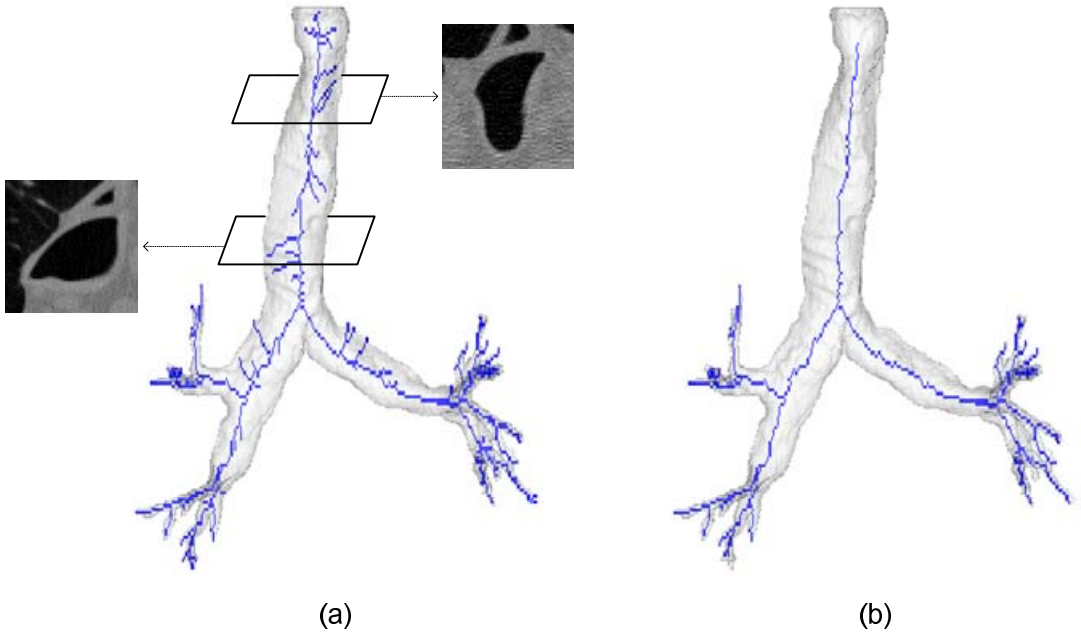

Figure 2.21: Trimming the skeleton. (a) An example with excessive amount of thinning artifacts. (b) After post-processing the skeleton. Two cross-sectional images of the trachea are shown in (a), which are not circular and have sharp tips that cause the thinning artifacts.

within a branch, as shown in Figure 2.23:

$$v = \begin{cases} \text{terminal voxel}, & \text{if } |N_v \cap S| = 1, \\ \text{within a branch}, & \text{if } |N_v \cap S| = 2, \\ \text{branch point}, & \text{if } |N_v \cap S| \geq 3, \end{cases} \tag{2.16}$$

where S is a set of voxels in the skeletal representation, and N_v is a set of 26-connected neighboring voxels of v.

The skeleton of each branch is traced through the voxels "within a branch" until either a "terminal voxel" or "branch point" is encountered. When a branch point is encountered, new branches are traced starting at the branch point. Each traversed branch is given an unique label and stored in a tree hierarchy defining parent-child relationships among the identified branches.

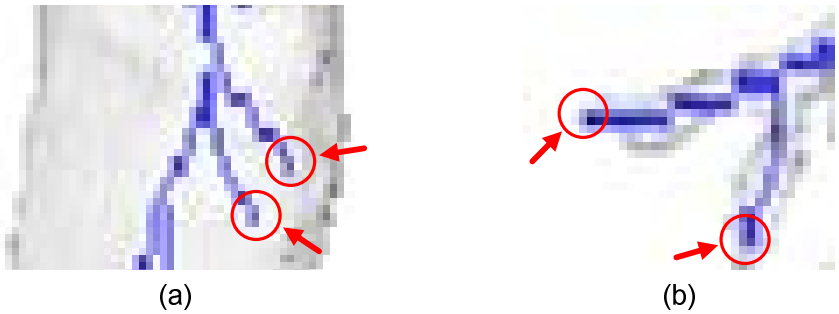

Figure 2.22: Examples of terminal branches. The clipped 3D renderings are shown for the false branches within the trachea (a) and the true branches (b). In each image, two terminal voxels are circled and identified by arrows.

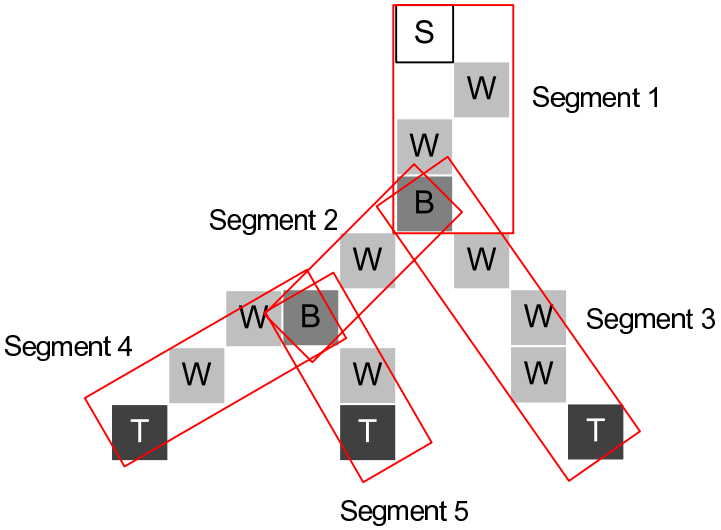

Figure 2.23: A 2D illustration of centerline traversing. The starting voxel is labeled with "S" in the figure. All other voxels are classified as a terminal voxel (T), branch point (B), or voxel within a branch (W). A rectangle is drawn for each traversed segment.

2.2.2 Intensity mapping

An airway segment is a tubular structure with a certain extent of curvature. Individual airway segments exhibit different length, orientation, and degree of curvature. It is inefficient to sample intensities from a raw scan data every time when visualizing and

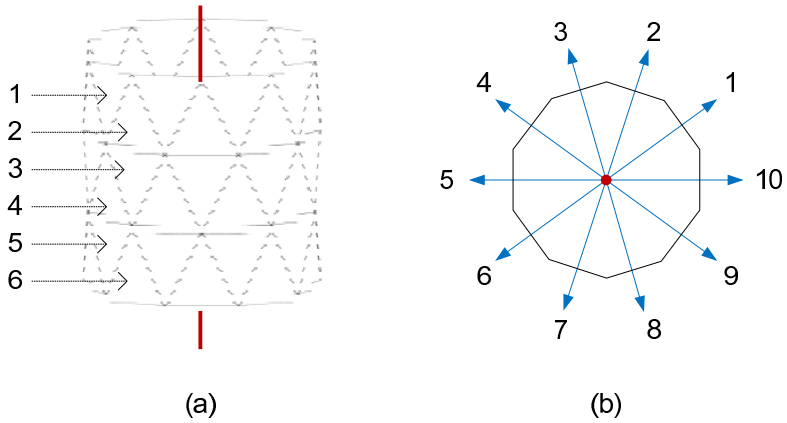

Figure 2.24: The cylindrical model for analyzing individual airway branch. (a) A cylindrical model with $l = 6$ and $m = 10$ is shown with its central axis. (b) The axial view of the model is shown, including a set of rays cast outward from the center.

measuring an airway segment. Therefore, a common segment-centric model is defined to which any airway segment can be mapped. Once the airway segment is mapped to the common model, it can then be visualized and measured using a standardized procedure regardless of the orientation and curvature of the given airway.

Segment-centric cylindrical model

The defined model has a cylindrical shape with a lateral surface that is composed of a triangular mesh (Figure 2.24). The model includes a set of rays cast outward from the central axis of the cylinder. The center of each triangle on the lateral surface defines the direction toward which a ray is cast. The quantitative measurement of an airway branch is to be performed for the rays defined in the model. The model has two parameters l and m, which corresponds to the number of layers and number of triangles per layer, respectively. An example of the cylindrical model with $l = 6$ and $m = 10$ is shown in Figure 2.24.

The value of l is determined based on the length of the given airway branch. The branch length is first estimated in mm and converted to voxels using the finest scan resolution. The value of m was selected based on the observation of the typical segmental airways. The observed outer diameter of segmental airways was approximately 10 mm, which yields the cross-sectional circumference of 31.4 mm. For the scans with the finest resolution of 0.5 mm/voxel, this corresponds to 62.8 voxels. Over-sampling was preferred in order to make use of all available image data, and m was set to 64 for the analysis.

Airway branch mapping

In order to analyze an airway branch qualitatively, the airway is first mapped to the cylindrical model by sampling intensities along the rays in 3D space. First, the centerline of the airway branch is defined using a polynomial. It has been observed that most airway branch appears with a curved trajectory with a single vertex (i.e. one turning point). However, some branches have two vertices which cannot be fitted using first or second degree polynomials. The cubic polynomial was used to approximate the curved trajectory of a single airway branch since it can be used to fit trajectories with up to two vertices.

The centerline of an airway branch is represented by $X(t)$, as shown in Figure 2.25, which is a line defined by three polynomials for each of x, y, and z coordinates:

$$X(t) = \begin{pmatrix} x(t) \\ y(t) \\ z(t) \end{pmatrix}, \tag{2.17}$$

where $x(t)$, $y(t)$, and $z(t)$ are cubic polynomials fitted for each of x, y, and z coordinates

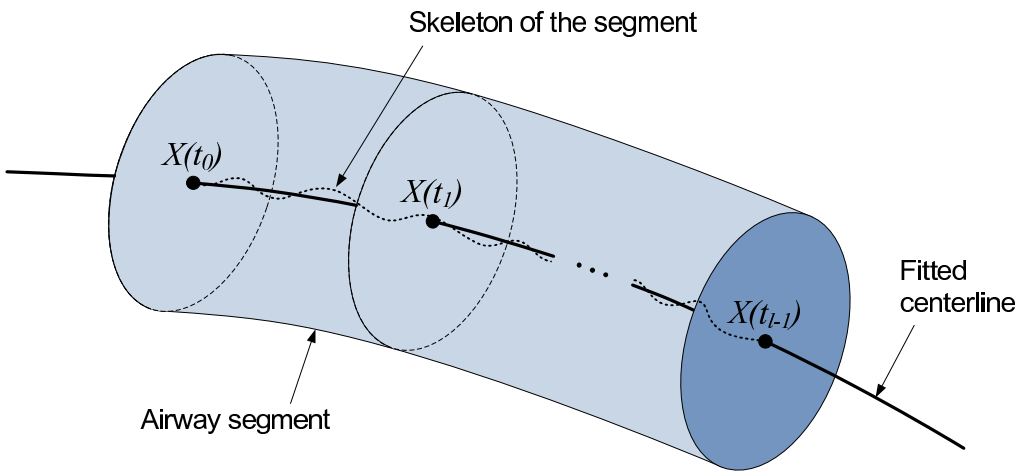

Figure 2.25: Polynomial fitting of the centerline. A line $X(t)$ is fitted to the skeleton of the airway segment using cubic polynomials for x, y, and z coordinates with respect to t.

of the segment's skeleton with respect to the independent variable t:

$$x(t) = \sum_{p=0}^{3} a_p t^p, \quad \mathbf{a} = \langle a_0\ a_1\ a_2\ a_3 \rangle, \tag{2.18}$$

$$y(t) = \sum_{p=0}^{3} b_p t^p, \quad \mathbf{b} = \langle b_0\ b_1\ b_2\ b_3 \rangle, \tag{2.19}$$

$$z(t) = \sum_{p=0}^{3} c_p t^p, \quad \mathbf{c} = \langle c_0\ c_1\ c_2\ c_3 \rangle, \tag{2.20}$$

where **a**, **b**, and **c** are the polynomial coefficients for x, y, and z coordinates, respectively.

The polynomials are fitted to the skeleton using a linear least squares fit. Linear least squares is a method for fitting a set of data points to a mathematical model by minimizing the residuals. For a set of n points, the coefficients that yields the minimum sum of squares of the residuals are found:

$$\underset{f}{\operatorname{argmax}} \left(\sum_{i=1}^{n} (x_i - f(x_i))^2 \right), \tag{2.21}$$

where $f(x)$ is a polynomial function for which the coefficients are found.

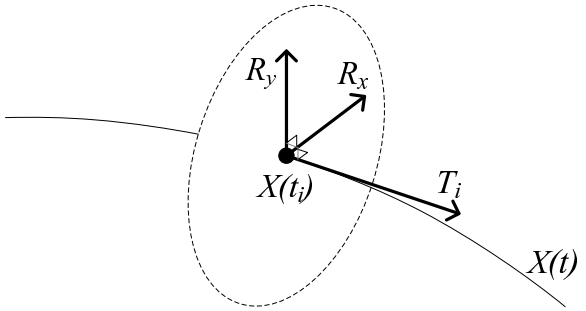

Figure 2.26: Defining the anchor vectors R_x and R_y. The vectors are constructed so that they are perpendicular to each other and to the tangent vector T_i at a point $X(t_i)$.

The independent variable t is set to range from 0.0 to 1.0. Along the fitted line $X(t)$, the discretized center points $X(t_i)$ are defined for $i = 0, 1, ..., l-1$ in such a way that t is equal to the center of individual layer defined in the cylindrical model. At each center point $X(t_i)$, the ray R_j is cast outward for $j = 0, 1, ..., m-1$ as defined in the cylindrical model. To determine the directions of R_j in CT image space, the vectors T_i, R_x, and R_y are defined at each center point as shown in Figure 2.26.

T_i is a tangent vector at $X(t_i)$, to which the cast rays should be perpendicular. For the polynomially fitted centerline $X(t)$, T_i can be computed as:

$$T_i = \left.\frac{dX(t)}{dt}\right|_{t=t_i} = \begin{pmatrix} x'(t_i) \\ y'(t_i) \\ z'(t_i) \end{pmatrix} = \begin{pmatrix} \sum_{p=1}^{3} a_p t_i^{p-1} \\ \sum_{p=1}^{3} b_p t_i^{p-1} \\ \sum_{p=1}^{3} c_p t_i^{p-1} \end{pmatrix}. \quad (2.22)$$

Two additional vectors R_x and R_y are defined and used as anchors to obtain the ray directions in 3D CT space. These vectors are used to preserve the spatial orientation of the rays in the subsequent sampling planes. R_x and R_y are defined so that they are perpendicular to T_i and to each other. For the first center point ($i = 0$), R_x is defined to be an arbitrarily oriented vector that is perpendicular to T_0, and R_y can be subsequently

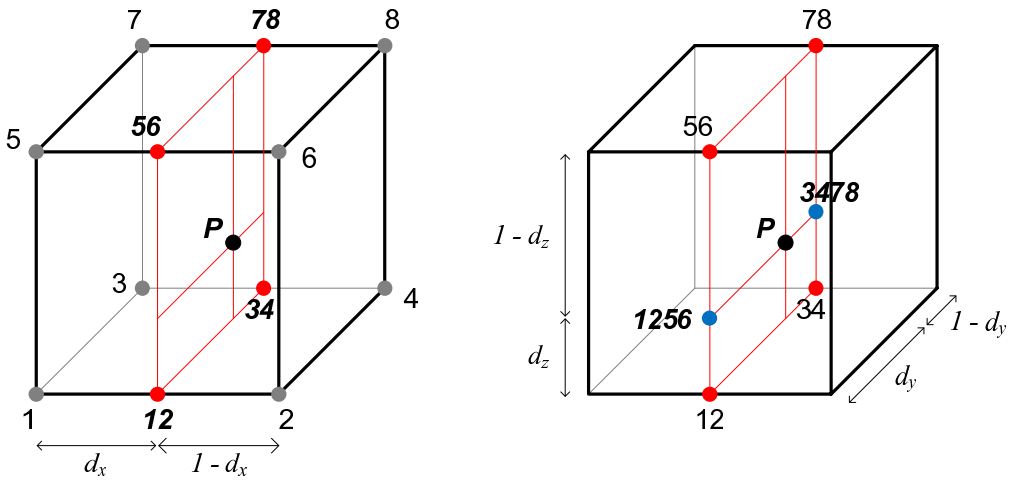

Figure 2.27: Trilinear interpolation. The weighted average of the surrounding voxel intensities is computed to estimate the intensity at a sub-voxel location p. The eight surrounding voxels are labeled 1-8. Two figures are shown for better visibility of the labeled points.

derived by taking a cross product of R_x and T_0. For all other center points ($i > 0$), the directions of R_x and R_y should be preserved. R_y is first computed based on the R_x from the previous layer (2.23), and R_x is derived from the newly-computed R_y (2.24).

$$R_y(i) = T_i \times R_x(i-1)\,, \tag{2.23}$$

$$R_x(i) = R_y(i) \times T_i\,. \tag{2.24}$$

Using R_x and R_y, a set of evenly-spaced vectors $R_j(i)$ is defined for each center point:

$$R_j(i) = \frac{R_x(i)}{\|R_x(i)\|}\cos\alpha_j + \frac{R_y(i)}{\|R_y(i)\|}\sin\alpha_j \tag{2.25}$$

where $\alpha_j = j2\pi/n$ and $j = 0, 1, ..., n-1$.

The sub-voxel intensities are sampled along each ray using trilinear interpolation. Trilinear interpolation is a widely-used technique for determining image intensity at sub-voxel location. The basic idea is to take the distance-weighted average of eight surrounding voxels in 3D space. An illustration of trilinear interpolation is shown in

Figure 2.27. To compute the interpolated intensity at sub-voxel point p, the weighted averages of four voxel pairs are first computed:

$$I_{12} = (1 - d_x) \cdot I(1) + d_x \cdot I(2) , \tag{2.26}$$

$$I_{34} = (1 - d_x) \cdot I(3) + d_x \cdot I(4) , \tag{2.27}$$

$$I_{56} = (1 - d_x) \cdot I(5) + d_x \cdot I(6) , \tag{2.28}$$

$$I_{78} = (1 - d_x) \cdot I(7) + d_x \cdot I(8) , \tag{2.29}$$

where $I(q)$ is the image intensity at a voxel q. Then, the weighted averages I_{1256} and I_{3478} are found using the computed values.

$$I_{1256} = (1 - d_z) \cdot I_{12} + d_z \cdot I_{56} , \tag{2.30}$$

$$I_{3478} = (1 - d_z) \cdot I_{34} + d_z \cdot I_{78} . \tag{2.31}$$

The interpolated value I_p at p can then be computed by taking the weighted averages I_{1256} and I_{3478}:

$$I_p = (1 - d_y) \cdot I_{1256} + d_y \cdot I_{3478} . \tag{2.32}$$

The intensities are sampled along each R_j with the sampling interval of l up to the distance d from the center point:

$$I(i, j, k) = S \left(X_i + k \cdot l \frac{R_j(i)}{||R_j(i)||} \right) , \tag{2.33}$$

where $S(p)$ is an interpolated intensity at point p, and $k = 0, 1, ..., d/l$. The value of l was set to 0.01 mm, and d was set to 15.0 mm as the radius of a segmental airway should not exceed this value.

The sampled intensities in each ray direction R_j are collected along the rays defined in the cylindrical model, effectively representing a curved airway branch using a cylindrical structure. An airway branch with any curvature and orientation may be mapped to

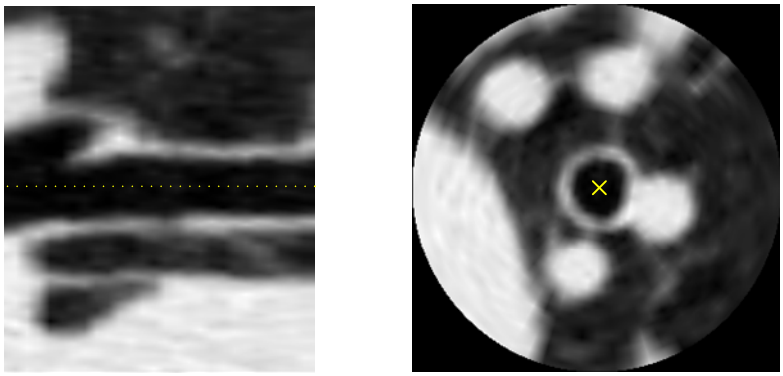

(a) (b)

Figure 2.28: Visualization of an airway branch mapped to a cylindrical model ($l = 35$, $n = 128$). The images shown are reconstructed from the sampled intensities along the rays in the model. (a) A coronal cross-sectional view is shown for the given airway branch. (b) An axial view is shown where "×" indicates the central axis.

the cylindrical model, and given the set of projected rays, cylinder outline representation of the image may be computed by remapping the ray data to airway images as shown in Figure 2.28.

2.2.3 Branch measurement

For every airway segment that has been mapped to the cylindrical model, a quantitative analysis can be performed to measure its lumen diameter and wall thickness. Measuring lumen diameter and wall thickness involves determination of airway wall boundary. Further step is required for wall thickness measurement due to the high-intensity structures adjacent to the airway.

Lumen diameter measurement

Once the intensities for an airway branch are mapped to the cylindrical model, the problem of measuring lumen diameter (LD) scales down to locating an inner wall boundary for every ray present in the model.

To determine the boundary between the airway lumen and the airway wall, the FWHM (full width at half maximum) principle is used. According to this principle, the boundary is located where the intensity value is half-way between the minimum and maximum intensities of the wall and the region adjacent to the wall as illustrated in Figure 2.29. FWHM has been a well-regarded method for measuring airway dimensions due to its simplicity. [56, 78] It has been reported that FWHM-based measurements under-estimates the lumen diameter and over-estimates the wall thickness [74]. The change in airway dimensions is the critical measurement of interest, and measurement bias was not the primary concern.

Using the sampled intensities I along a ray corresponding to a vector R in the airway model, the inner boundary b_{in} can be computed as:

$$b_{in}(R) \;=\; \underset{d}{\operatorname{argmin}} \left| I(d) - \frac{min_1 + max}{2} \right|, \quad d_{min_1} < d < d_{max}, \tag{2.34}$$

where max is the maximum intensity along the ray, min_1 is the minimum intensity along the ray before reaching the maximum intensity, and d_{max} and d_{min_1} are the locations on the ray where max and min_1 are observed, respectively. The distance to the inner boundary b_{in} is computed for every ray corresponding to a vector $R_j(i)$ in the model. The inner boundary is an estimate of the lumen radius, and the lumen diameter is estimated by doubling the value. For a given airway branch, the average lumen diameter is computed:

$$LD \;=\; \frac{2}{l \cdot m} \sum_{i=0}^{l-1} \sum_{j=0}^{m-1} b_{in}(R_j(i)) \tag{2.35}$$

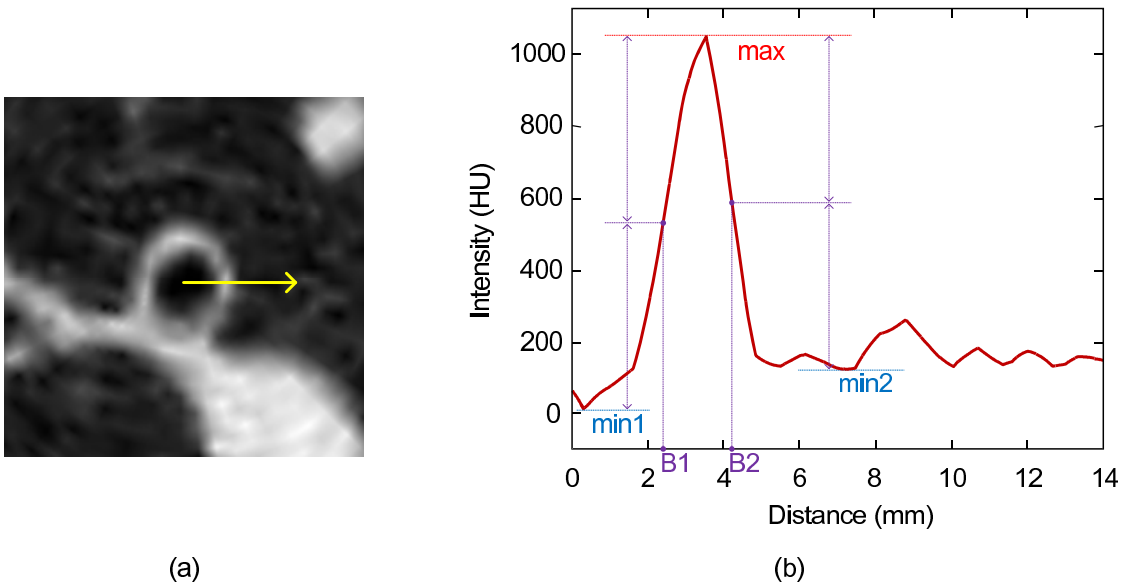

Figure 2.29: Full width at half maximum measurement. Along the ray annotated in (a), the image intensities are plotted (b). The airway wall boundary is identified by locating a voxel with the intensity that is half-way between the minimum and maximum intensity ranges on each side of the boundary region.

Wall thickness measurement using skewness minimization

For measuring the wall thickness (WT), the outer boundary must be located in addition to the inner boundary for every ray present in the model. The outer boundary b_{out} is identified using the FWHM principle, and the distance between the outer and inner boundaries for each ray is an estimate of the wall thickness:

$$b_{out}(R) = \underset{d}{\operatorname{argmin}} \left| I(d) - \frac{max + min2}{2} \right|, \quad d_{max} < d < d_{min2}\,, \tag{2.36}$$

$$WT(i, j) = b_{out}(R_j(i)) - b_{in}(R_j(i))\,, \tag{2.37}$$

where max is the maximum intensity along the ray, min_2 is the minimum intensity along the ray beyond the maximum intensity, and d_{max} and d_{min_2} are the locations on the ray where max and min_2 are observed, respectively. Then, the wall thickness of a given

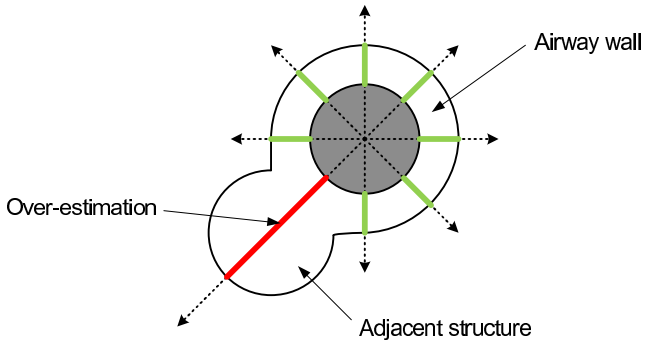

Figure 2.30: Over-estimation of wall thickness due to the adjacent structure. An illustration is shown with 8 rays cast outward from the center. The wall thickness estimation for one of the rays is affected by the adjacent structure.

segment can be computed by taking the average of all rays present in the model:

$$WT = \frac{1}{l \cdot m} \sum_{i=0}^{l-1} \sum_{j=0}^{m-1} b_{out}(R_j(i)) - b_{in}(R_j(i)) \tag{2.38}$$

Unlike lumen diameter measurement, wall thickness assessment is prone to over-estimation due to the high-intensity structures adjacent to the airway that can affect the wall thickness. An example of an adjacent pulmonary artery is shown in Figure 2.28b. The rays that go through these structures will result in erroneous over-estimation of the wall thickness as illustrated in Figure 2.30, therefore affecting the average wall thickness estimate for the corresponding airway branch.

In order to reduce the effect of adjacent structures, the distribution of the wall thickness measurements from all cast rays is considered. In an ideal case where there is no attachment to the airway, a normal distribution of wall thickness measurements is expected.

The wall thickness distribution for an airway segment is plotted as a histogram in Figure 2.31. The over-estimation caused by the adjacent structures affects the distribution as it pulls the distribution toward the right (i.e. positively-skewed distribution). The

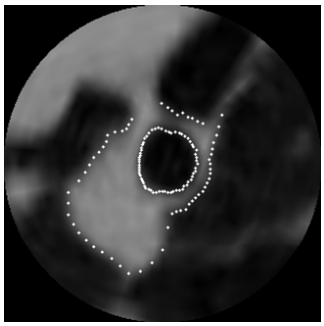

(a)

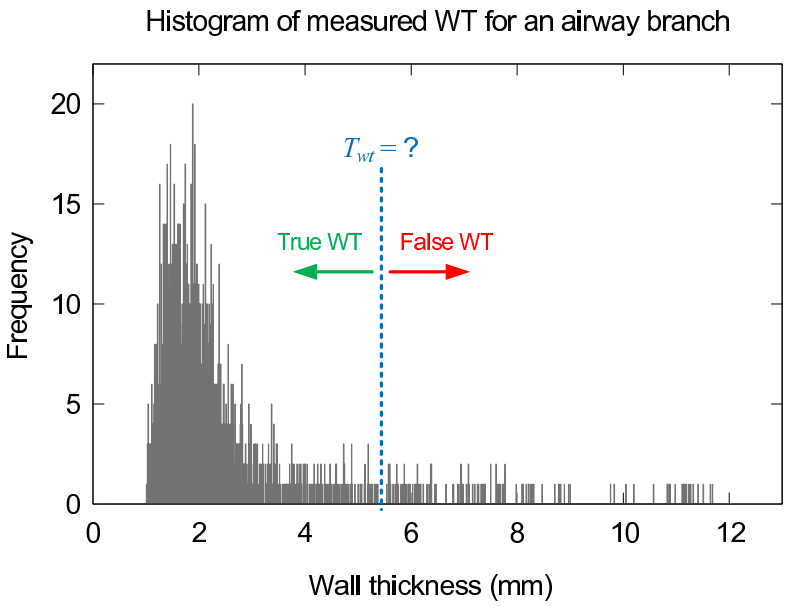

(b)

Figure 2.31: Histogram of all measured wall thicknesses for an airway segment. The distribution is positively skewed due to the high-intensity structures adjacent to the airway. To avoid the over-estimation of the airway's average wall thickness, false measurements must be ignored by determining a wall thickness threshold T_{wt}.

effect of over-estimation is reduced by determining a wall thickness threshold T_{wt} and taking only the measurements that are below the threshold. The wall thickness threshold T_{wt} is determined by using skewness of the distribution.

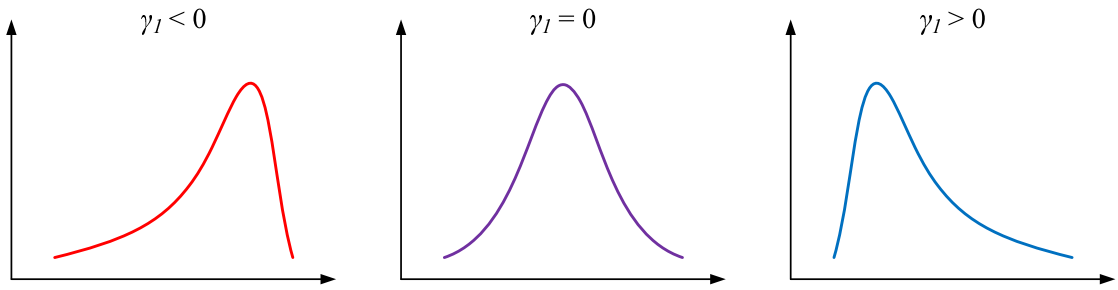

Figure 2.32: Skewness γ_1 of a distribution. The distributions with negative, zero, and positive skewness are shown.

Skewness γ_1 measures the asymmetry of the distribution, as shown in Figure 2.32, and is defined as:

$$\gamma_1 = \frac{\mu_3}{\sigma^3}, \tag{2.39}$$

where σ is the standard deviation, and μ_3 is the third central moment which can be computed for the wall thickness distribution as:

$$\mu_3 = \sum_w (w - \mu)^3 f(w), \tag{2.40}$$

where μ is the mean of the distribution, w is the wall thickness, and $f(w)$ is the frequency of the wall thickness w. In (2.40), the summation is performed for all wall thickness measurements in the distribution.

For an ideal case, the wall thickness would be uniform along the given segment, and there would be no adjacent high-intensity structures. In such a case, the variation in wall thickness measurements within a segment would be caused by image noise. To validate this concept, the synthetic image of a hollow tube was created by subtracting an image of small circle ($r = 20 voxels$) from an image of large circle ($r = 30 voxels$). The resulting binary image included a hollow tube with 10-voxel wide wall. The inner region of the tube had the image intensity of 0, and the tube wall had the image intensity of 255. The final image was created by adding Gaussian noise of $\sigma = 40$ to the binary

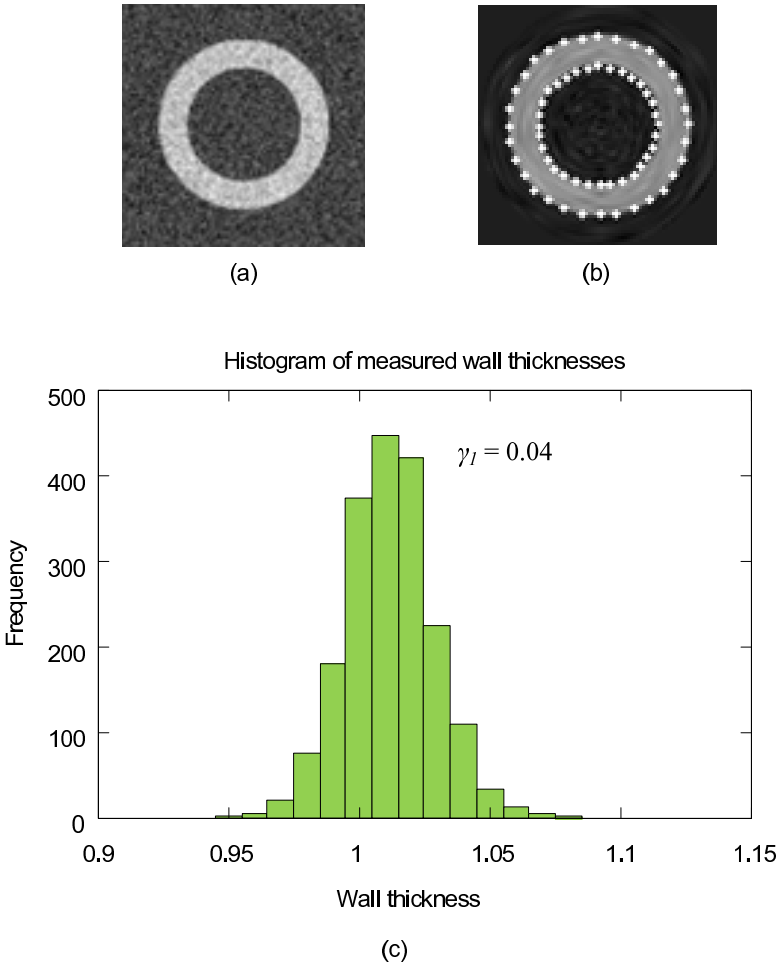

Figure 2.33: Wall thickness distribution of a synthetic tube. (a) A synthetic image of a hollow tube with Gaussian noise (σ = 40). (b) The radially reconstructed axial view with the measured points. Different windowing function is used from the image shown in (a) to highlight the measured points. (c) The histogram of the measured wall thicknesses (γ_1 = 0.04).

tube image and had the image intensities ranging from -218 to 469.

When there are adjacent structures, the distribution of an airway's wall thickness, as shown in Figure 2.31, is likely to be positively skewed ($\gamma_1 > 0$) due to erroneous overestimations. The algorithm determines the final wall thickness threshold by finding a

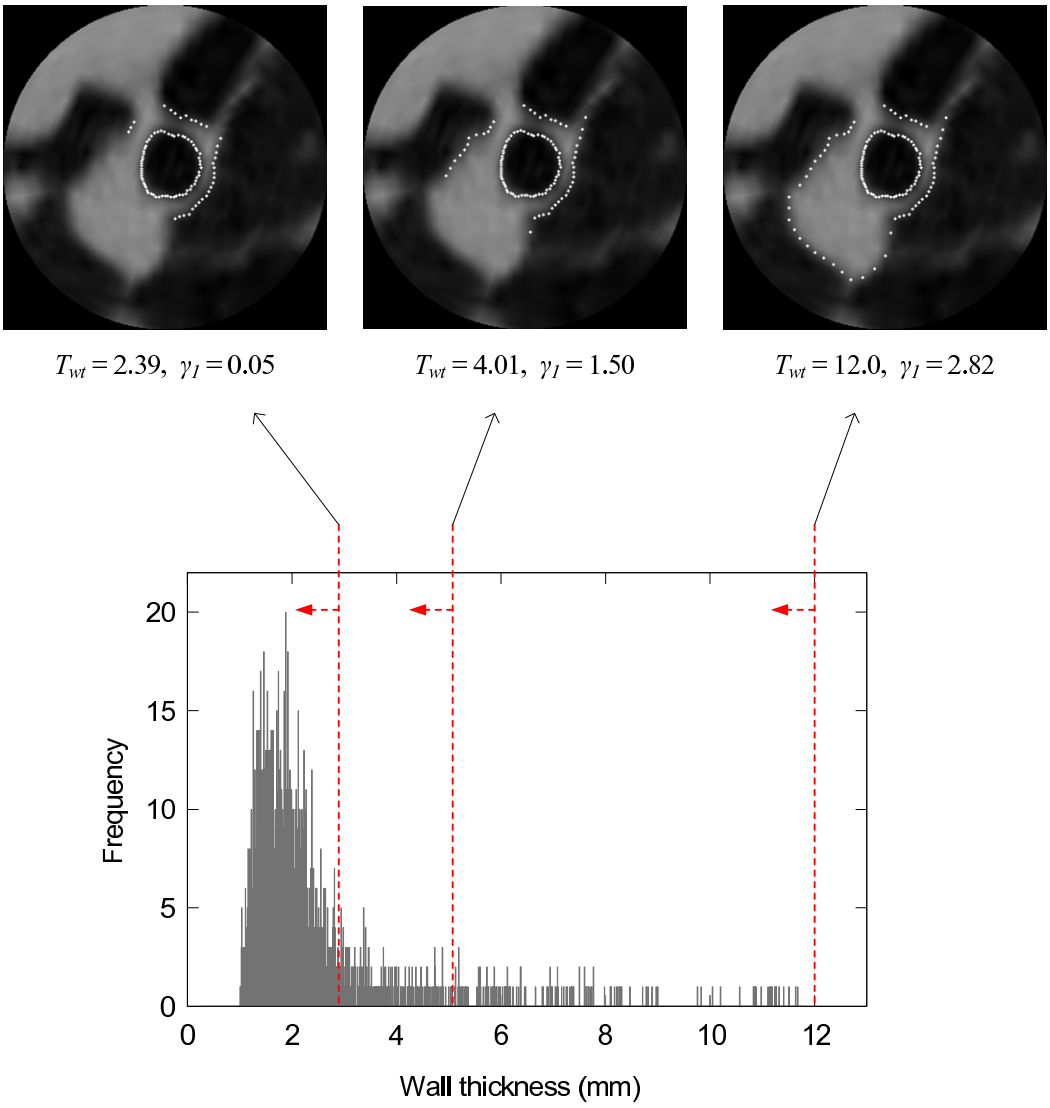

Figure 2.34: Skewness minimization. An axially-reconstructed views of an airway segment with the measured points are shown for three different values of T_{wt} for which the dotted vertical lines are shown on the histogram. As γ_1 is minimized, the effect of over-estimation caused by the adjacent structures is reduced.

value of x that minimizes the skewness:

$$T_{wt} \;=\; \underset{x}{\text{argmin}} \left\{ \frac{\sum_{w=0}^{x} (w - \mu_{w<x})^3 \; f(w)}{\sigma^3_{w<x}} \right\}. \tag{2.41}$$

The effect of skewness minimization for an airway branch is shown in Figure 2.34. For the given airway branch, minimizing wall thickness threshold eliminates the false measurements caused by the adjacent structure.

2.3 Segment matching for comparative measurements

In order to assess segmental change in airway dimension using repeat scans, each airway branch must be matched across the scans. The variation in segmentations from serial scans, due to differences in patient orientation, degree of inspiration, acquisition parameters, and image noise, poses a challenge when matching the corresponding segments across the scans. There may be branches that are segmented in one scan and not segmented in another, and simply using a skeletal airway tree representation for segment matching is likely to result in false matches.

Each airway branch has a starting and ending point. For every airway branch, the starting point corresponds to the end point of its parent branch. If the matching process is initiated from the lower generation branches and proceeds toward the higher generation, only the end point of each branch needs to be matched. The matching algorithm uses the original image intensities in the local region of interest (ROI) around the end point, as well as the tree hierarchy to guide the traversing of the match candidates.

2.3.1 3D image registration

A 3D registration algorithm is used to determine if two end points, referred to as match candidates, belong to the same airway branch. Spherical volumes of interest are established around the end points as shown in Figure 2.35 and registered to each other in

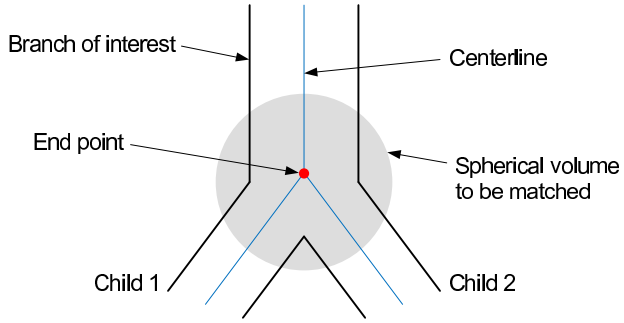

Figure 2.35: 2D illustration of segment matching. The end points are matched to find the corresponding segments. The spherical volume is established around the end point of the airway branch to be matched. The radius of the sphere is chosen to cover the parenchyma region around the airway.

order to assess the similarity of the image intensities within the volumes. To account for difference in scan resolutions the spheres are sampled as isotropic volumes with same resolutions.

The similarity metric used is the mean squared error (MSE) between the voxel intensities of two spherical regions:

$$MSE(C_1, C_2) = \frac{1}{|C_1 \cap C_2|} \sum_{C_1 \cap C_2} (I_1(i, j, k) - I_2(T(p, q, r)))^2, \tag{2.42}$$

where I_1 and I_2 are the CT images, and $T(p, q, r)$ is the transform function (i.e. translation and rotation) that maps a spherical region C_2 to spherical region C_1.

The registration algorithm finds the optimal transform (i.e. translation and rotation) that minimize the MSE between the two spherical volumes. A simple hill-climbing search [77] is used to find local minima. Since the airway tree of the same patient is being considered, the end point of the same airway branch should not have a large variation in location and orientation. To optimize algorithm and minimize errors, the translation and rotation search ranges were limited to 3.5 mm and 10 degrees around each axis, respectively, since the variations observed from the training cases were well

within these values. The step sizes for translation and registration were 1 voxel and 1 degree, respectively.

The size of the sphere was based on the branch generation and was chosen so that the spherical volume includes the parenchyma region around the branch point. The cross-sectional radii of the airways at different generations were observed in the training cases, and 5 mm was added to include parenchyma region. The sphere radii used by matching algorithm were 35, 25, 20, 15 mm for 1st, 2nd, 3rd, and >4th generations, respectively.

2.3.2 Matching procedure

A flowchart showing the matching process is shown in Figure 2.36. The outline of the algorithm is as follows:

1. Identify match candidates.
2. Perform 3D image registration of the candidate regions.
3. Evaluate similarity and classify as a match or non-match.
4. If a match, then form new match candidates and repeat steps 1-3.
5. If a non-match, then adjust match candidates and repeat steps 1-3.

The matching begins with the trachea and proceeds in a depth-first manner. The matching algorithm first identifies match candidates from a given CT scan pair and performs 3D registration to assess similarity of the candidates. When a match is found the algorithm must identify new match candidates for which the search space is constrained to the subtree under the matched branch.

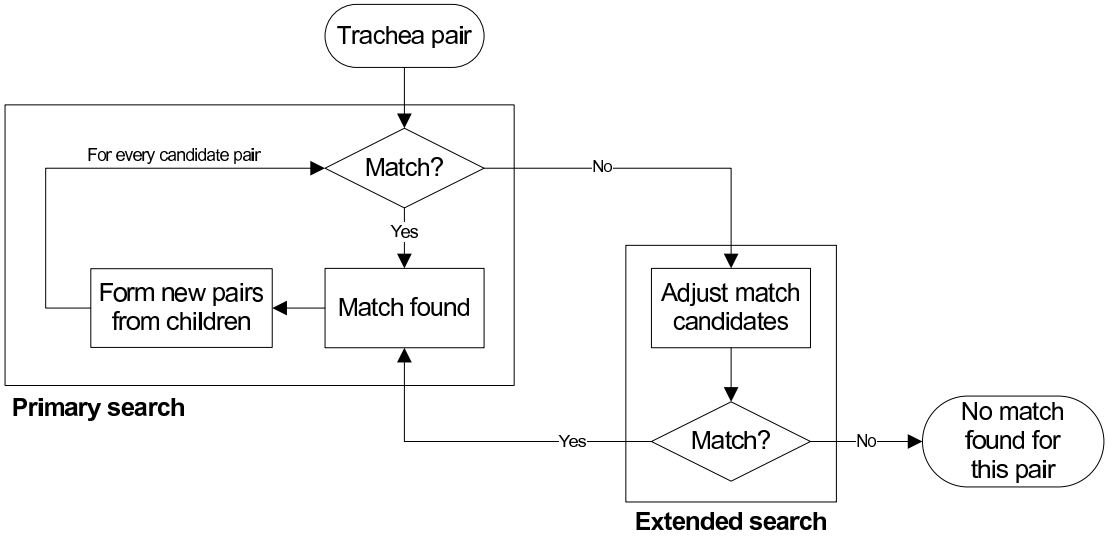

Figure 2.36: Flowchart for airway branch matching. The algorithm is initiated by matching trachea's from a pair of scans and proceeds toward higher generation branches. An extended search is performed when no match is found in a primary search.

When there are two children branches under the matched branch, there are two possible scenarios of forming match candidates. The candidates are paired based on the orientation of the branches since identical branches should have similar orientations. The scenario that yields the minimum angle difference is chosen as shown in Figure 2.43, and the candidate pairs are formed accordingly.

$$C = argmin_{X \in S}\{min\{Angle(p), p \in X\}\}, \tag{2.43}$$

where X is a scenario in a set S of all possible scenarios, p is a pair of match candidates, $Angle(p)$ is the angle between a candidate pair p, and C is the final candidate pairing scenario used by the algorithm.

Each pair of match candidates is classified as a match or non-match based on the similarity metric used by the registration (i.e. MSE):

$$p = \begin{cases} \text{Match, if } MSE(p) \leq \tau, \\ \text{Non-match, if } MSE(p) > \tau, \end{cases} \tag{2.44}$$

where MSE is the mean squared error between the registered ROIs, and τ is a threshold. The trachea can be identified reliably without using image registration in most CT scans, and the value of τ is adaptively determined for a given scan pair based on MSE between the registered end points of trachea:

$$\tau = MSE(E_{trach1}, E_{trach2}) + tolerance, \tag{2.45}$$

where E_{trach1} and E_{trach2} are the end points of the tracheas from scan 1 and scan 2, respectively, and MSE is the mean squared error between the registered ROIs around the end points. The term *tolerance* was introduced in order to account for MSE variations in different pairs of ROIs and reduce false negatives. The value of *tolerance* was determined by observing the MSE variations of different end points in the training cases.

When a match is found, the algorithm proceeds by forming new match candidates in depth-first manner. In the case of a non-match, the algorithm performs an extended search by adjusting the candidate locations as shown in Figure 2.37. A non-match would mean that the end points of the given airway segment pair are at different locations within the airway tree. The starting point, on the other hand, is already matched since it is the end point of the parent. This would mean that the two airway segments have different length, as shown in Figure 2.37a. Such a case may be frequently encountered due to the variation in airway tree segmentation for two CT scans.

The algorithm performs the extended search by introducing a “dummy” end point to the longer airway segment, as shown in Figure 2.37b. The location of a “dummy” end

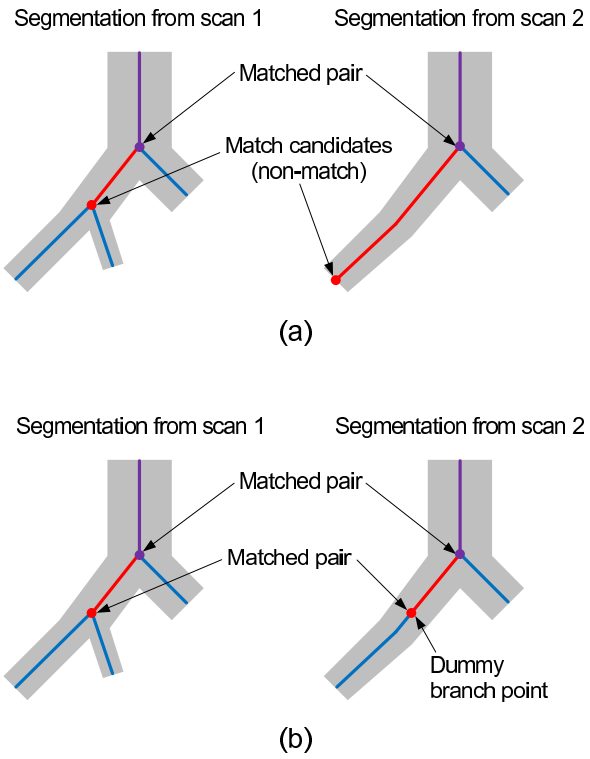

Figure 2.37: Extended search for branch matching. (a) Illustration of a non-match. Variation in tree segmentations may cause a non-match between the match candidates, and the extended search is necessary. (b) Extended search by adjusting a match candidate. To overcome segmentation variation a "dummy" branch point is placed on the under-segmented airway tree.

point is determined by considering the length of the shorter segment. The newly-formed match candidates, using a "dummy" end point, are then matched using 3D registration.

2.3.3 Experiment to evaluate the airway branch matching

The goal of this experiment was to evaluate the accuracy of the automated branch matching. The airway branch matching algorithm must have high accuracy since the automated measurements are to be performed on the matched airway pairs.

The matching algorithm was run on a set of CT scan pairs, and 3D visualizations were created for both trees where the matched branch was rendered with a same color and label across the airway trees from the two scans. In a pair of 3D visualizations, each of the matched branches was then evaluated visually to determine correctness of the matching. The accuracy of the matching algorithm was quantified as the percentage of the correct matches from the total number of matches.

The dataset used for the experiment was 120 low-dose whole-lung CT scan pairs from a screening database. All scans were taken with low radiation dose (120 kVp, 40 mAs) and had a slice thickness of 1.25 mm and in-plane resolution ranging from 0.53×0.53 to 0.82×0.82 mm per pixel. Each scan pair was taken from a same patient, and the time interval between two scans was 16.5 ± 7.1 months (mean $\pm$ SD). Six cases were used for optimizing the algorithm parameters, and the remaining 114 cases were used for the evaluation of the algorithm.

2.3.4 Results and discussion

The result of running the automated branch matching algorithm on 114 scan pairs is shown in Table 2.3. On average, the branch-finding algorithm located 46 airway segments per scan, and the matching algorithm correctly matched 31 segments across the scans. All airway branches up to 4th generation were matched successfully. An example of matching output on a scan pair is shown in Figure 2.38 where the matched end points are labeled with the same number.

A high matching accuracy (99.7%) was achieved by using both image intensity and the skeletal structure. The algorithm performance was especially good with larger airway branches, as 100% accuracy was observed for the airway branches up to 4th gener-

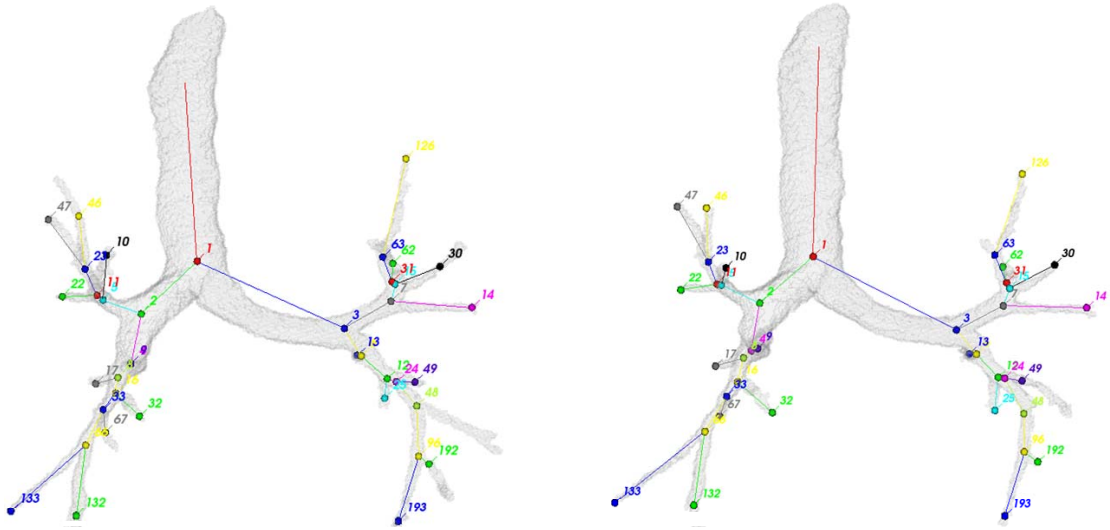

Figure 2.38: Airway branch matching result on a scan pair. Coronal visualization of the segmented airway trees are shown. The matched end points are labeled with the same number and color. The straight lines connecting the end points are shown.

Table 2.3: Accuracy of Automated Segment Matching

Generations	Matched segments	Correct match	Match per case
All	3591	3581 (99.7%)	31
up to 4th	1553	1553 (100%)	13

ation.

On average 31 airway segments were matched across the scan pair, while more than 40 segments have been identified in individual scans. Frequently, an airway branch identified in a first scan was not identified in a second scan due to the variation in segmentation outcome. Another reason why all identified segments were not matched was that once the algorithm failed to match a given airway segment, all subsequent branches

could not be matched. Although the algorithm did not match all segments identified in each scan, 31 matched segments correspond to the airway branches up to 5th generation.

2.4 Quantitative Experiments

Two experiments were conducted to evaluate the precision of the presented method and to correlate airway measurements to PFT scores. In the first experiment, the precision of quantitative measurements was quantified using a zero-change dataset. In the second experiment, the inter-generation lumen diameter measurements were compared to the airway branching models. In the third experiment, measured airway dimensions were correlated to PFT scores.

2.4.1 Precision of airway measurement

The goal of this experiment was to evaluate the precision of the automated airway measurement. The evaluation of quantitative measurements is challenging since it is difficult to establish manual ground truth. In this experiment serial CT scan pairs were used for validating the precision of the quantitative analysis. For the scan pair of the same patient taken within a short time interval, the segmental dimensions are not expected to change significantly, since the patient did not develop any chronic disease in the interim. Therefore any difference in measurement across a scan pair would be attributed to measurement variation, or precision.

Method

The automated algorithm measured the average lumen diameter and wall thickness for each branch matched across the scan pair. Only the airways beyond the 4th generation were considered since these airways are located inside the lungs. The measurement precision was quantified by computing the limits of agreement for the measured branches in the scan pairs. The precision was evaluated for individually matched segment (per-segment precision) as well as for individual patient (per-patient precision). For per-patient analysis, the measurement changes for all matched segments in the patient were averaged. For wall thickness measurements, the F-test was used to compare measurement precisions for conventional FWHM method and the γ_1 minimization method.

For evaluating the precision of quantitative measurements the scan pairs with a time interval of less than two months were selected from the 120 cases used for the branch matching. The final dataset included 44 scan pairs with the time interval of 38 ± 9 days (mean ± SD).

Results and discussion

A total of 809 matched airway segments beyond the 4th generation were considered. The average measurement was 4.91 mm for lumen diameter and 1.80 mm for wall thickness. The 95% limits of agreement for the measurements on the scan pairs are reported in Table 2.4.

The mean and the 95% limits of agreement (LoA) for the wall thickness measurements with and without γ_1 minimization are reported in Table 2.5. F-test showed a statistically significant difference ($p<0.01$) between the precisions of two methods. The examples showing the effect of the new method are shown in Figure 2.39.

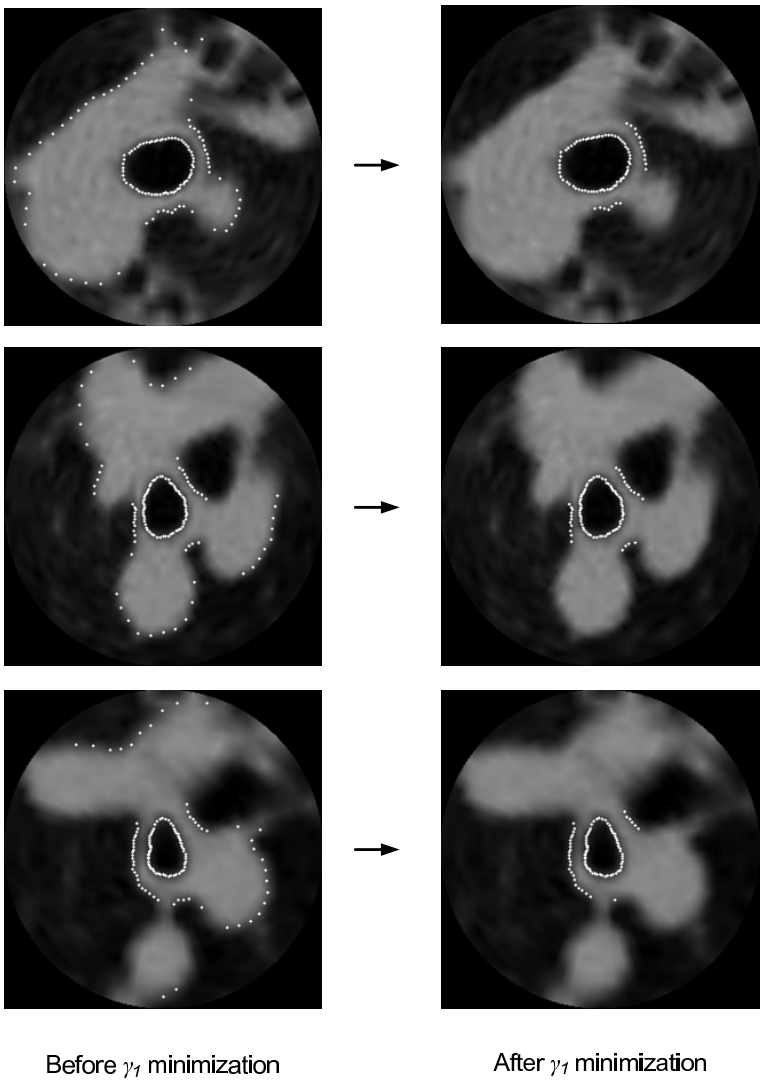

Figure 2.39: Examples showing the effect of γ_1 minimization. Left images show the measured points using conventional FWHM, and the right images show the measured points after applying γ_1 minimization.

Bland-Altman plots of the lumen diameter measurements are shown in Figure 2.40. For wall thickness measurements, Bland-Altman plots are shown for both measurements with and without γ_1 minimization in Figure 2.41.

The 95% limits of agreement were computed for measuring individual airway segment and for measuring individual patient. Per-patient precision was computed since all

Table 2.4: 95% Limits of Agreement (LoA) for Airway Measurements

		Lumen diameter (mm)		Wall thickness (mm)	
	n	95% LoA	Bias	95% LoA	Bias
Per-segment variation	809	[-0.83, 0.90]	0.03	[-0.49, 0.48]	-0.01
Per-patient variation	44	[-0.51, 0.53]	0.05	[-0.16, 0.16]	-0.05

Table 2.5: Effect of γ_1 minimization on Wall Thickness (WT) Measurements

	Mean WT (mm)	95% LoA (mm)	Bias (mm)
FWHM	5.16	[-1.14, 1.04]	-0.05
FWHM with γ_1 minimization	1.80	[-0.49, 0.48]	-0.01

airway segments were expected to exhibit similar changes for a patient with systemic airway disease. As expected per-patient variation of measurements across the scans was less than per-segment variation for both lumen diameter and wall thickness. From the Bland-Altman plots shown in Figures 2.40 and 2.41, it was observed that there was no apparent variation in measurement precision across different airway sizes.

The γ_1 minimization approach for measuring wall thickness was compared to the conventional FWHM method. FWHM method expectedly over-estimated the wall thickness as the mean wall thickness measurement was 5.16 mm, compared to 1.80 mm when γ_1 minimization was used. More relevant observation was that the 95% limits of agreement on the wall thickness measurements were narrower for the new method as shown in Figure 2.41, meaning that the precision of the wall thickness measurements using γ_1 minimization was better than that of the conventional FWHM method. There was a statistically significant difference ($p<0.01$) between the precisions of two methods according to F-test.

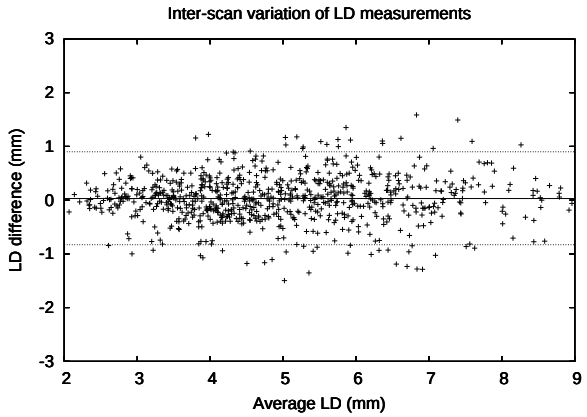

Figure 2.40: Bland-Altman plot of lumen diameter measurements (n=809). Differences in measurements across the scan pairs are plotted against the average measurements. The lines are drawn for the bias in LD difference (solid line) and 95% limits of agreement (dotted line).

2.4.2 Comparison with airway tree model

The goal of this experiment was to compare the measured diameters of different branch generations to the airway branching model presented by others. The generation-based lumen diameter measurements were compared to the expected diameters computed using two different airway branching models that were presented in the previous literature [41, 89].

Method

Using the diameter ratio derived from the models, the expected diameter was computed from the average diameter measurement from the previous generation. The expected diameters were computed using two different models by Kitaoka and Tawhai.

Kitaoka et al. [41] proposed a 3D model of the human airway tree based on a flow division model. Based on the relationship between diameter and flow rate that they have

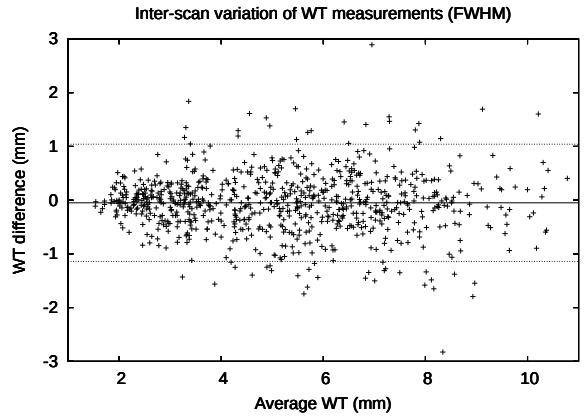

(a)

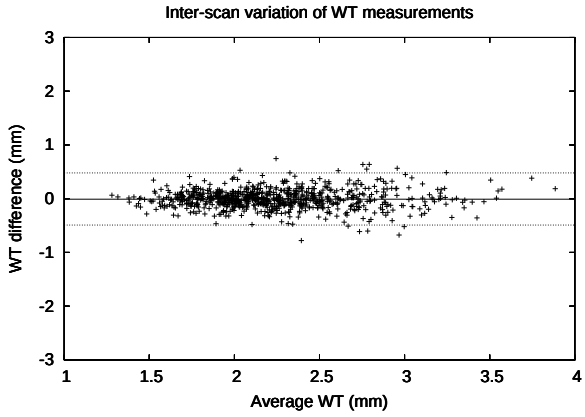

(b)

Figure 2.41: Bland-Altman plots of wall thickness measurements (n=809). The plots are shown for two measurement methods: (a) without γ_1 minimization and (b) with γ_1 minimization (p<0.01). Differences in measurements across the scan pairs are plotted against the average measurements. The lines are drawn for the bias in WT difference (solid line) and 95% limits of agreement (dotted line).

proposed, the diameter ratio between each of two branches and its parent may be derived as shown in (2.46) and (2.47).

$$\frac{d_1}{d_0} = r^{1/n}, \tag{2.46}$$

$$\frac{d_2}{d_0} = (1 - r)^{1/n}, \tag{2.47}$$

where $d1$ and $d2$ are the diameters of two child branches, d_0 is the diameter of a parent,

r is ratio of flow rate in the first child branch, and n is the diameter exponent. Based on a minimum energy loss principle, Kitaoka et al. [40] estimated the value of n to be 2.8 in human lungs. The average diameter ratio between two consecutive branch generations may then be derived as the following:

$$\frac{d_i}{d_0} = \frac{d_1 + d_2}{2d_0} = \frac{r^{1/n} + (1-r)^{1/n}}{2}. \tag{2.48}$$

Assuming that the air flow is distributed evenly in diverging branches (i.e. $r = 0.5$), the diameter ratio between two consecutive generations is estimated to be 0.78.

Tawhai et al. [89] presented a different airway model and computed the diameter ratio between child and parent branches. The three-dimensional conducting airway model was generated and used to simulate air flow in the airway tree. The value of the diameter ratio for their generated model was reported to be 1.109. Since they used the airway ordering scheme that counted up from the terminal branches, the inverse of the reported ratio (i.e. 0.902) was used to compute the expected diameter.

Results and discussion

The average measurements for different airway generations are shown in Table 2.6. The lumen diameter and wall thickness measurements, as expected, were smaller for higher generation airway segments.

The box-whisker plots of the lumen diameter measurements are shown in Figure 2.42, along with the expected diameter computed using two airway models. The root mean squared error (RMSE) between the actual measurement and the expected diameter was 0.47 mm for Kitaoka model and 0.36 mm for Tawhai model. The RMSE between the diameters expected from two models was 0.60 mm. For all airway generations, the expected diameters were within one standard deviation from the mean of the measured

Table 2.6: Measurement for different generations (Mean ± SD)

Generation	n	Lumen diameter (mm)	Wall thickness (mm)
4th	440	6.17 ± 1.39	2.14 ± 0.57
5th	450	4.96 ± 1.28	1.81 ± 0.48
6th	372	4.12 ± 1.08	1.66 ± 0.36
7th	194	3.88 ± 1.21	1.56 ± 0.37
8th	108	3.60 ± 0.92	1.50 ± 0.31
≥9th	54	-	-

diameters.

The diameter measurement was in better agreement with Kitaoka model for 5th and 6th generations, while it agreed better with Tawhai model for 7th and 8th generations, as shown in Figure 2.42. This may be due to lack of measurement accuracy at 7th and 8th generation branches, given that the radius of these airways correspond to approximately two image voxels at scan resolution.

2.4.3 Correlation of PFT scores with image measurements

The goal of this experiment was to correlate airway dimensions to PFT scores and investigate the contribution of other image-based measures in estimating PFT scores. PFT is the standard method for diagnosing COPD. CT imaging is more expensive than PFT but often is taken for other purposes. The existing CT images may be used to estimate degree of COPD in a patient, in order to complement PFT measures and obtain further information that may be relevant to disease.

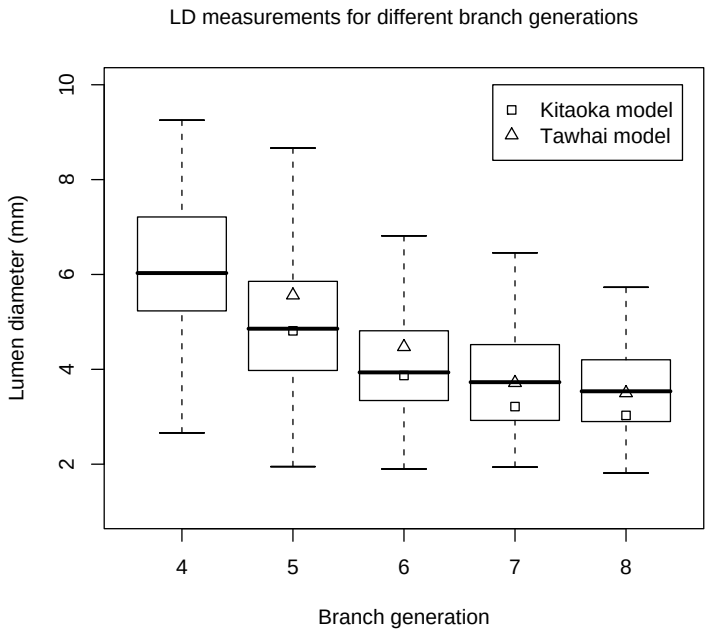

Figure 2.42: The box-whisker plots of lumen diameter measurements for different generations. The expected diameters, computed from two different airway models, are shown for 5th, 6th, 7th, and 8th generations.

Emphysema is a major type of COPD and is characterized by destruction of alveolar air sac walls. Alveolar destruction results in reduced surface for gas exchange, reduced lung compliance, and hyper-inflation. Previously, people have attempted to measure emphysema severity using low-dose CT images [33, 35]. The measures of emphysema that can be retrieved from CT images include emphysema index, mean lung density, fractal dimension, and lung-diaphragm height ratio. The emphysema index and mean lung density use CT image intensity within the lungs to estimate degree of emphysema. The fractal dimension is a measure based on the size of destructed air sac observable from CT images. The lung-diaphragm height ratio is used to measure lung compliance by computing the ratio between lung and diaphragm heights. It has been suggested that these measures have moderate correlation to PFT scores [34]. In this experiment, the contribution of airway dimensions is investigated, in addition to the emphysema

measures, when a multivariate model is used to estimate PFT scores.

Method

The automated algorithm measures the lumen diameter and wall thickness for each branch identified from the scans in the dataset. For each of 4th, 5th, and 6th generation airways, WT/LD ratio was computed and correlated with the PFT scores. The normalized PFT measures, including FEV1/FVC and FEV1%, were used.

Further, the contribution of combining airway measures with other image-based measures are investigated using a multivariate regression model. Along with airway WT/LD ratio (A), three other terms were included in the model:

$$Y = a + b_1A + b_2F + b_3D + b_4V \tag{2.49}$$

- Fractal dimension (F): density-based measure of emphysema
- Lung-diaphragm height ratio (D): measure of lung hyperinflation
- Lung volume (V): inspiration volume of the lung

To train and evaluate the model, 4-fold cross-validation was used.

The dataset included 388 low-dose chest CT scans where PFT scores were available for all patients. The degree of COPD in the patients ranged from mild to moderate, as the FEV1% showed mean and standard deviation of 94 ± 16.

Results and discussion

The scatter plots between WT/LD ratio and PFT scores are shown in Figures 2.43 and 2.44 for FEV1/FVC and FEV1%, respectively. The correlation coefficients between

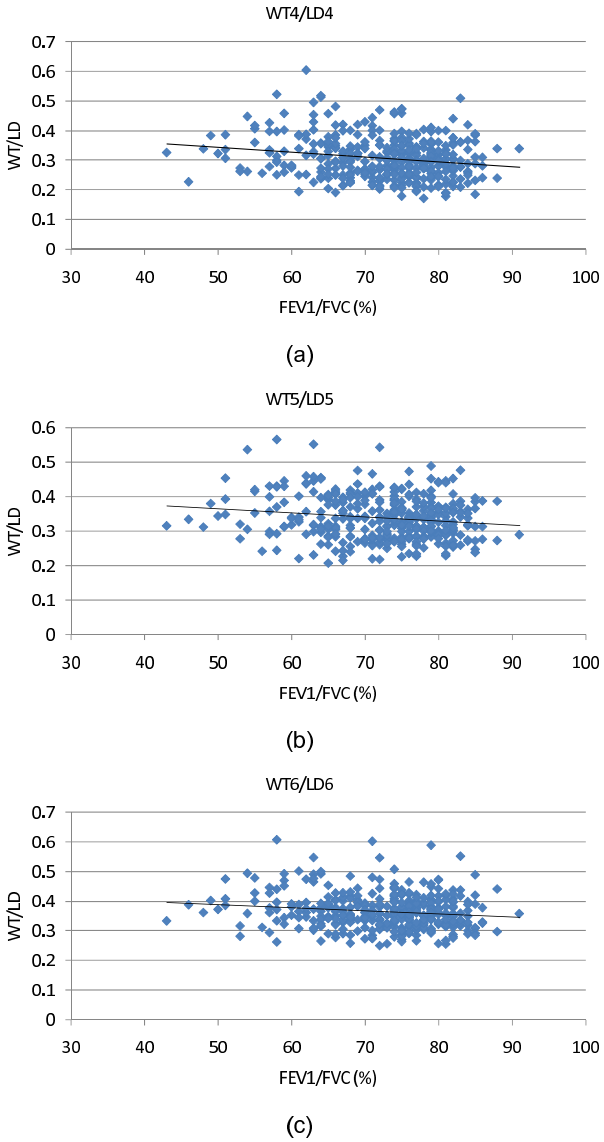

Figure 2.43: Scatter plots showing WT/LD ratio vs. FEV1/FVC (%). The plots are shown for (a) 4th, (b) 5th, and (c) 6th generation airways. The correlation coefficients (*r*) were -0.193, -0.163, and -0.147 for 4th, 5th, and 6th genrations, respectively.

WT/LD ratio at different airway generations and PFT scores are reported in Table 2.7.

The scatter plots between multivariate estimation and true PFT scores are shown in Figure 2.45. The correlation coefficients between different image-based measures and PFT scores as well as the multivariate estimation and true PFT scores are shown in Table

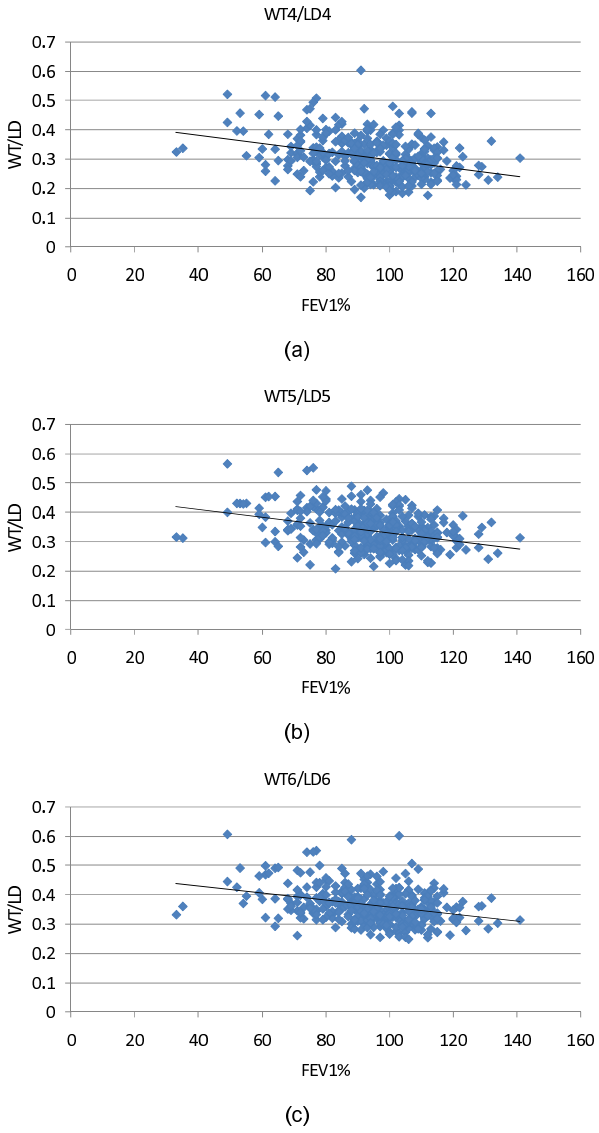

Figure 2.44: Scatter plots showing WT/LD ratio vs. FEV1%. The plots are shown for (a) 4th, (b) 5th, and (c) 6th generation airways. The correlation coefficients (r) were -0.328, -0.350, and -0.335 for 4th, 5th, and 6th generations, respectively.

2.8.

As expected, airway WT/LD ratio showed negative correlation with both PFT scores. However, weak correlation coefficient was observed when using airway dimension by itself. For all three airway generations used, the correlation coefficient $|r| < 0.20$ was ob-

Table 2.7: Correlation coefficients between WT/LD ratio and PFT scores

	FEV1/FVC	FEV1%
WT/LD of 4th generation	-0.193	-0.328
WT/LD of 5th generation	-0.163	-0.350
WT/LD of 6th generation	-0.147	-0.335

Table 2.8: Correlation coefficients between different measures and PFT scores

	FEV1/FVC	FEV1%
Airway WT/LD	-0.15	-0.33
Fractal dimension	-0.37	-0.08
Diaphragm height ratio	-0.24	-0.17
Lung volume	-0.40	-0.02
Multivariate	**0.52**	**0.35**

served between WT/LD and FEV1/FVC, and $|r| < 0.35$ was observed between WT/LD and FEV1/FVC.

When multivariate regression model was used, improvement over any single measure was observed in terms of correlation with both FEV1/FVC and FEV1%, as shown in Table 2.8. The correlation coefficient $r = 0.52$ and $r = 0.35$ were observed for FEV1/FVC and FEV1%, respectively.

Nakano et al. [57] have correlated different image-based measures with PFT scores. The comparison of correlation coefficients is shown in Table 2.9. They observed similar correlation between airway measures and PFT scores as ours but higher correlation between emphysema measure and PFT scores. As a result, the reported correlation co-

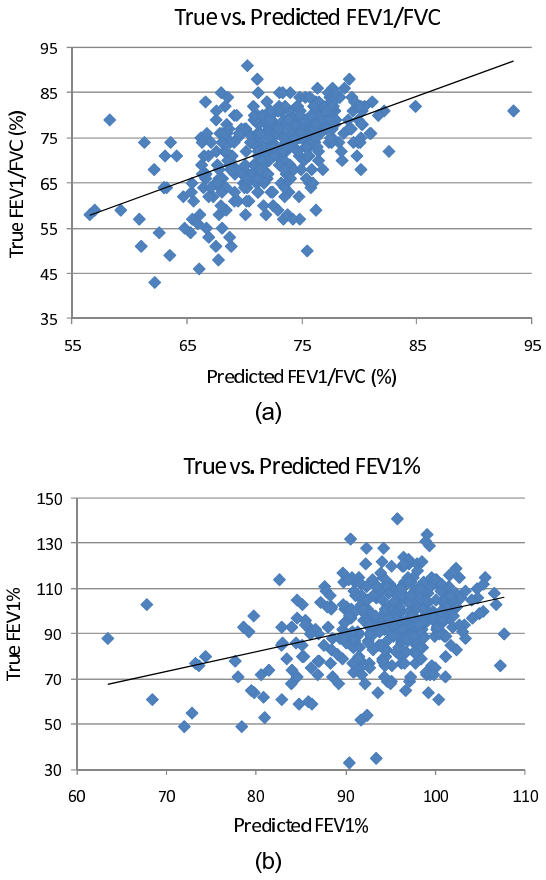

Figure 2.45: Scatter plots showing multivariate estimation of PFT. The plots are shown for (a) FEV1/FVC and (b) FEV1%. The correlation coefficients (r) were 0.52 and 0.35 for FEV1/FVC and FEV1%, respectively.

efficient for their multivariate estimation was higher than ours for both FEV1/FVC and FEV1%.

The experimental setup used by Nakano was compared with ours to investigate the cause of differences. While Nakano et al. has manually selected 2D image slices to take cross-sectional measurement of airways, our measurement method was fully-automated. The CT images in their dataset were taken at clinical radiation dose, compared to low radiation dose for our dataset. Density-based emphysema measures are sensitive to image noise, and using low-dose images can affect correlation. More importantly, their

Table 2.9: Comparison of correlation coefficients

	PFT	Airway measure	Emphysema measure	Multivariate
Nakano	FEV1/FVC	-0.19	-0.65	0.70
	FEV1%	-0.34	-0.53	0.66
Our method	FEV1/FVC	-0.15	-0.37	0.52
	FEV1%	-0.33	-0.17	0.35

dataset consisted of patients with wide range of COPD severity. The FEV1% of the patients had the mean and standard deviation of 48±28, compared to 94±16. Including healthy patients as well as the patients with very severe COPD in the dataset is likely to yield high correlation.

CHAPTER 3

SEGMENTATION OF ANATOMICAL STRUCTURES

Segmentation of chest organs and biological structures create a labeled atlas of the chest. The labeled atlas of the chest not only provides quantitative information to radiologists, but also serves as basis for comparing across population and different scans of same patient. Further, it provides foundation for surgical planning and computer-guided surgery.

A fully-automated top-down approach is used with the ultimate objective of segmenting all visible anatomical entities. The relatively simple structures that can be robustly identified are segmented first, and other structures are segmented using pre-segmented structures as a foundation. In this chapter, the automated algorithms for segmenting various anatomical structures, including airways (presented in Section 2.1), spinal canal, ribs, and vertebrae, are presented. Each algorithm has been evaluated using large datasets of low-dose chest CT scans.

3.1 Segmentation of spinal canal and ribs

An axial CT image showing spinal canal and ribs is shown in Figure 3.1. The spinal canal can be robustly identified from chest CT image and serve as a basis for segmenting other bone structures. The rib segmentation may be used as a baseline reference for locating other organs and features within the chest. Typically an individual has 24 ribs, 12 on each side of the chest. In this section, a fully automated algorithm to segment the spinal canal and individual ribs from a chest CT scan is presented. The challenges for automatically segmenting individual ribs are their proximity to a corresponding vertebra and the intensity variation within a rib due to bone marrow and bone density variations.

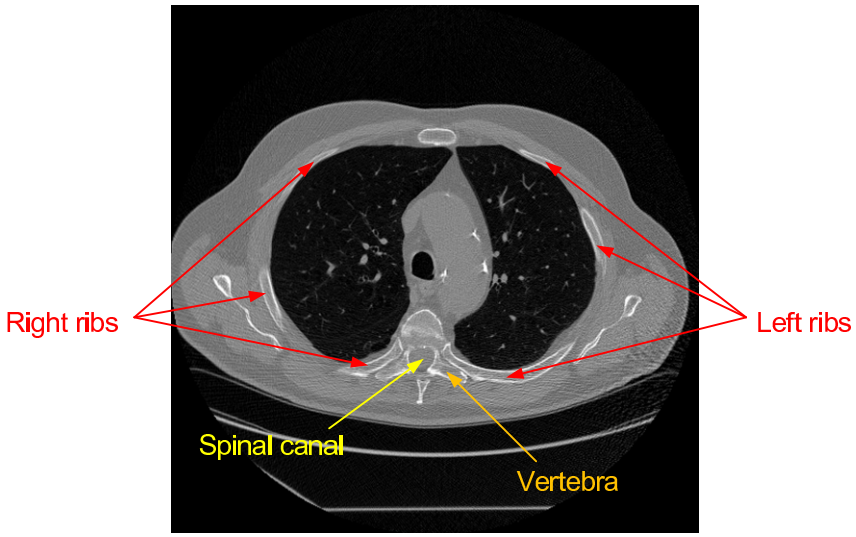

Figure 3.1: Spinal canal and ribs in a CT scan. An axial image slice is shown where the ribs, vertebra, and spinal canal are labeled.

3.1.1 Strategy for rib segmentation

There has been little work reported in the literature on the rib segmentation task, and two references are of interest. Staal et al. and Klinder et al. have proposed rib segmentation methods using chest CT images. Staal et al. [86] reconstructed ribs from the classified rib primitives. Their algorithm however is sensitive to adjacent bone structures has been tested on only 18 CT scans. Klinder et al. [43] detected rib centerline from pre-established rib cage model. Their method is heavily dependent on initial global model and has only been tested on 20 CT scans.

To segment each rib, it is necessary to separate the rib from the corresponding vertebra. Figure 3.2 illustrates our approach for growing a rib. For each rib to be segmented, a seed region is identified on the rib, and the rib is traced toward both inward and outward directions. Segmenting the inner portion of the rib is more challenging than segmenting the outer portion due to the proximity to the vertebra. Different techniques are used to

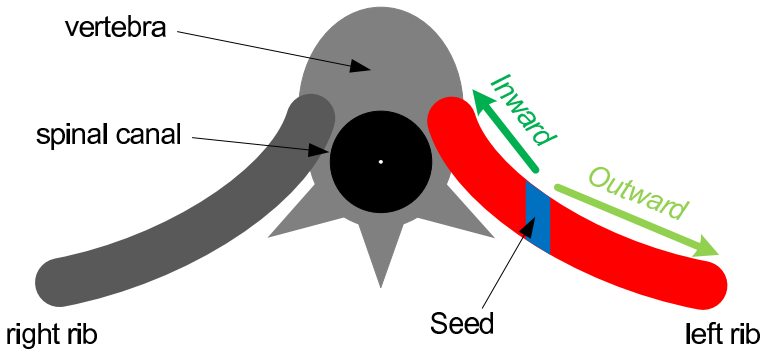

Figure 3.2: The illustration of the rib segmentation approach. The rib is grown in both directions from a seed. Inner portion is adjacent to the vertebra, and different techniques are used to segment inner and outer portions.

trace the ribs toward inward and outward directions.

3.1.2 Rib segmentation algorithm

The algorithm to segment individual ribs is outlined with a flowchart in Figure 3.3. The algorithm to segment individual ribs employs a stepwise approach and consists of four stages. First, all the bone structure present in the scan is segmented. Second, the centerline of the spinal canal is identified. Then, based on the identified centerline and the segmented bone, a seed region for every rib is detected. Finally, individual ribs are grown from each seed and separated from the corresponding vertebra.

1. Bone segmentation

The first step is to segment the bone structures in the given CT scan. The outcome of bone segmentation includes all the bone structures visible in the chest CT including the rib cage, scapula, sternum, and clavicle.

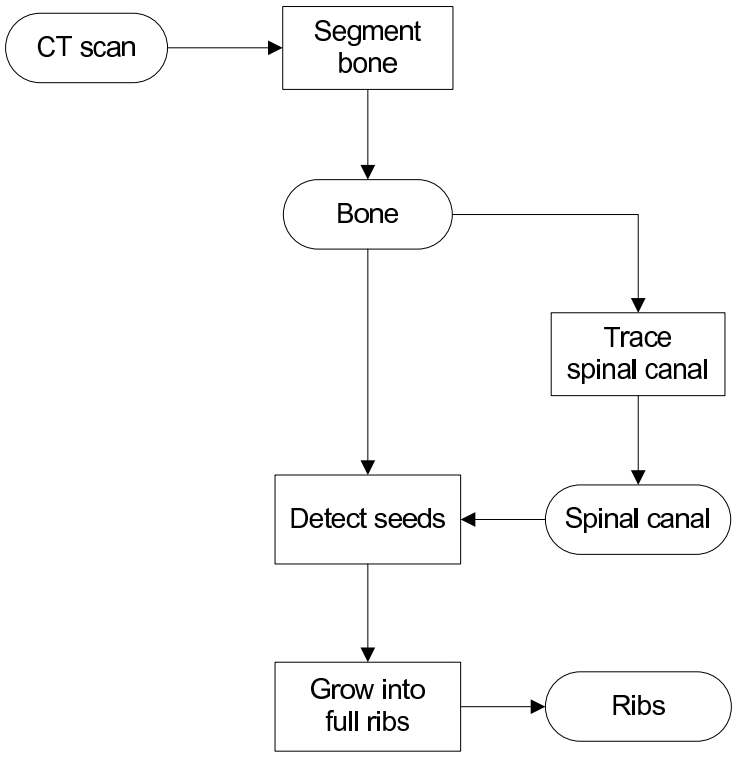

Figure 3.3: Flowchart for the proposed method. Bone and spinal canal are found first and used to detect the seed for every rib. Stepwise approach yields segmentation of ribs as well as spinal canal and other bones.

The algorithm to segment bones is as follows:

1. Filter each axial image with a 3x3 mean filter to reduce noise.
2. Threshold the image at T_i to capture high-intensity voxels.
3. Connected component analysis.
4. Remove any connected components that are smaller than T_v.
5. Remove the scan table that may be present in the image and has a higher intensity than T_i.

The effect of the mean filter on the thresholded output is shown in Figure 3.4. Applying mean filter diminishes the effect of high-intensity streaking noise present in low-

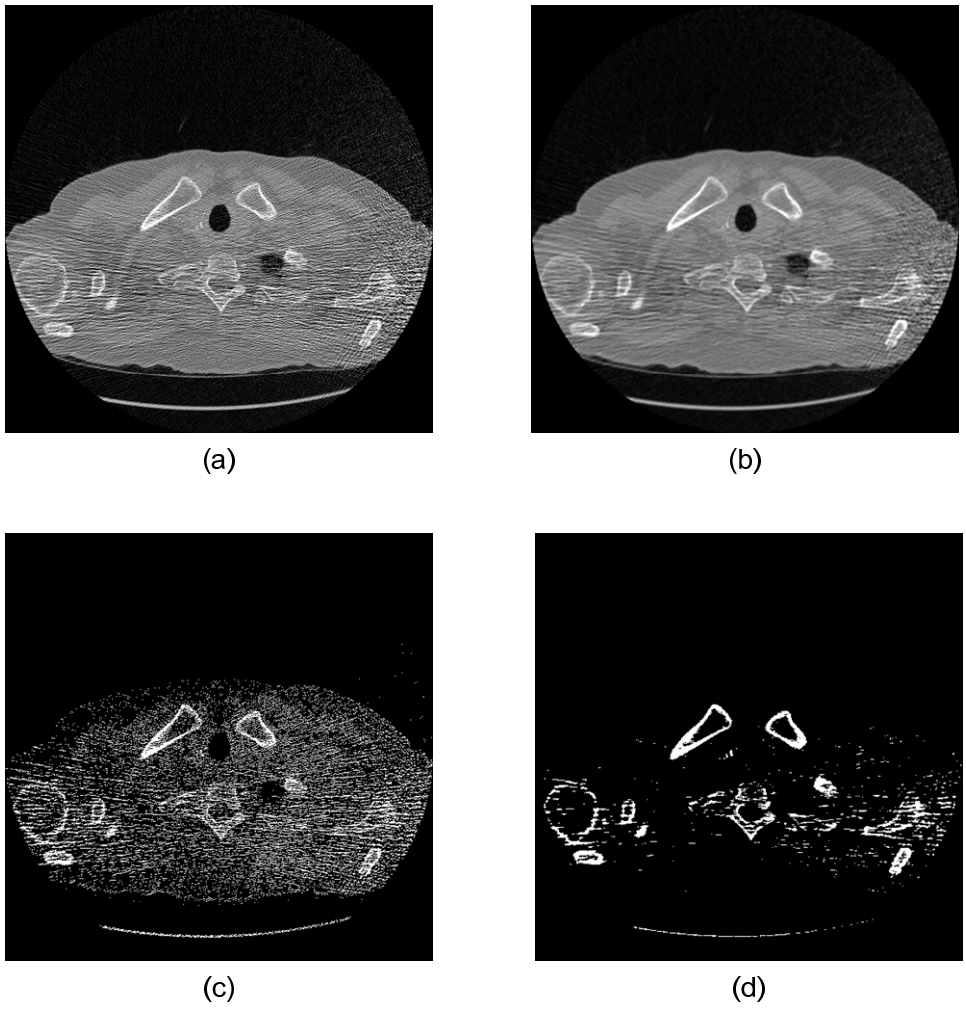

Figure 3.4: Effect of mean filter on thresholded output. An axial image is shown for: (a) raw CT image, (b) CT image after mean filtering, (c) raw image thresholded at 270 HU, (d) filtered image thresholded at 270 HU. Applying mean filter diminishes the effect of high-intensity noise, and bones are more distinguishable when thresholding.

dose CT images, and as a result, bones become more distinguishable when the image is thresholded.

The scan table often appears in a CT image, as shown in Figure 3.4a. The scan table appears as a high-intensity object and is not removed in Step 4 of the algorithm due to a large volume. The center of mass $(\overline{x}, \overline{y})$ of each connected component is used to detect

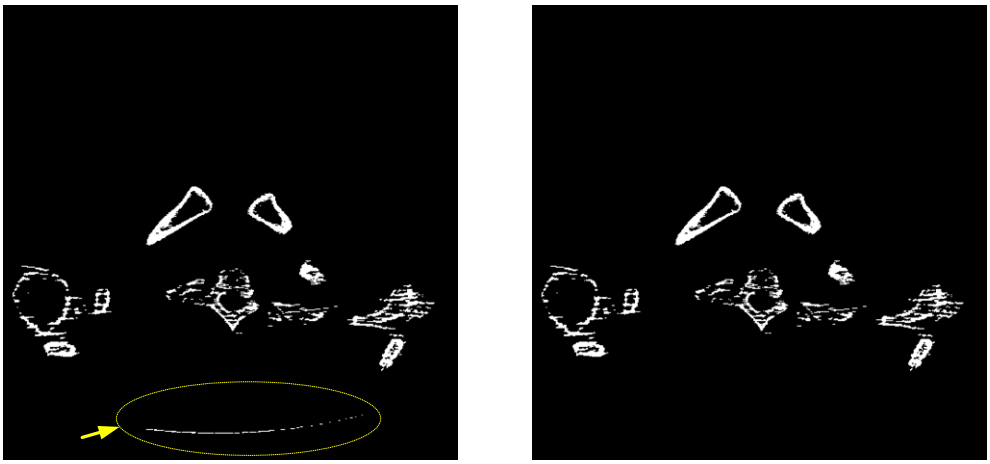

Figure 3.5: Scan table removal. An axial image is shown for: (a) after removing noise voxels and (b) final bone segmentation after removing scan table. The scan table is indicated with an oval and arrow on (a).

and remove a scan table. The table should be located toward the bottom in the axial image and should have small $\bar{y}$. A component with $\bar{y} < \epsilon$ is considered a scan table and removed from the bone segmentation. Upon the observation of the training cases, the value of ϵ was set to one fifth of the y dimension of the image:

$$\epsilon = 0.2 \cdot (y_h - y_l), \tag{3.1}$$

where y_h and y_l are the highest and lowest y coordinates of the image, respectively. An example of the scan table removal is shown in Figure 3.5.

The values of T_i and T_v were determined empirically by experimenting with the training cases. The intensity threshold T_i was set to 270 HU. The value was chosen to include all bones in the scan and to be high enough so that the hollow region of the rib corresponded to approximately one third of the external rib diameter. The volume threshold T_v was chosen to exclude high-intensity noise components and set to 4500 mm^3 since the volumes of all valid bone components were well within this value.

Figure 3.6: Tracing of spinal canal's centerline. The traced line is shown in a sagittal projection of the spine. The extracted center line is used to locate the seed points for individual ribs.

2. Spinal canal tracing

In this section, the algorithm to trace the center of the spinal canal using the segmented bone structure is presented. Figure 3.6 shows the extracted center line of the spinal canal in sagittal view.

Entire canal is traced upward using an iterative algorithm starting at the seed point in the lowest axial image. The tracing algorithm is outlined as a flowchart in Figure 3.7. A seed point is automatically identified from the projection of a set of *n* lowest image slices. Each iteration of the algorithm involves identification of a point at an image slice using the point located in the previous iteration.

An example of the axially-projected image is shown in Figure 3.8. To find a seed point from the projected image, the largest connected component *L* is found, and the largest hole within *L* is identified. The center of mass of the identified hole is used as an initial seed point. The algorithm to identify the largest hole is as follows:

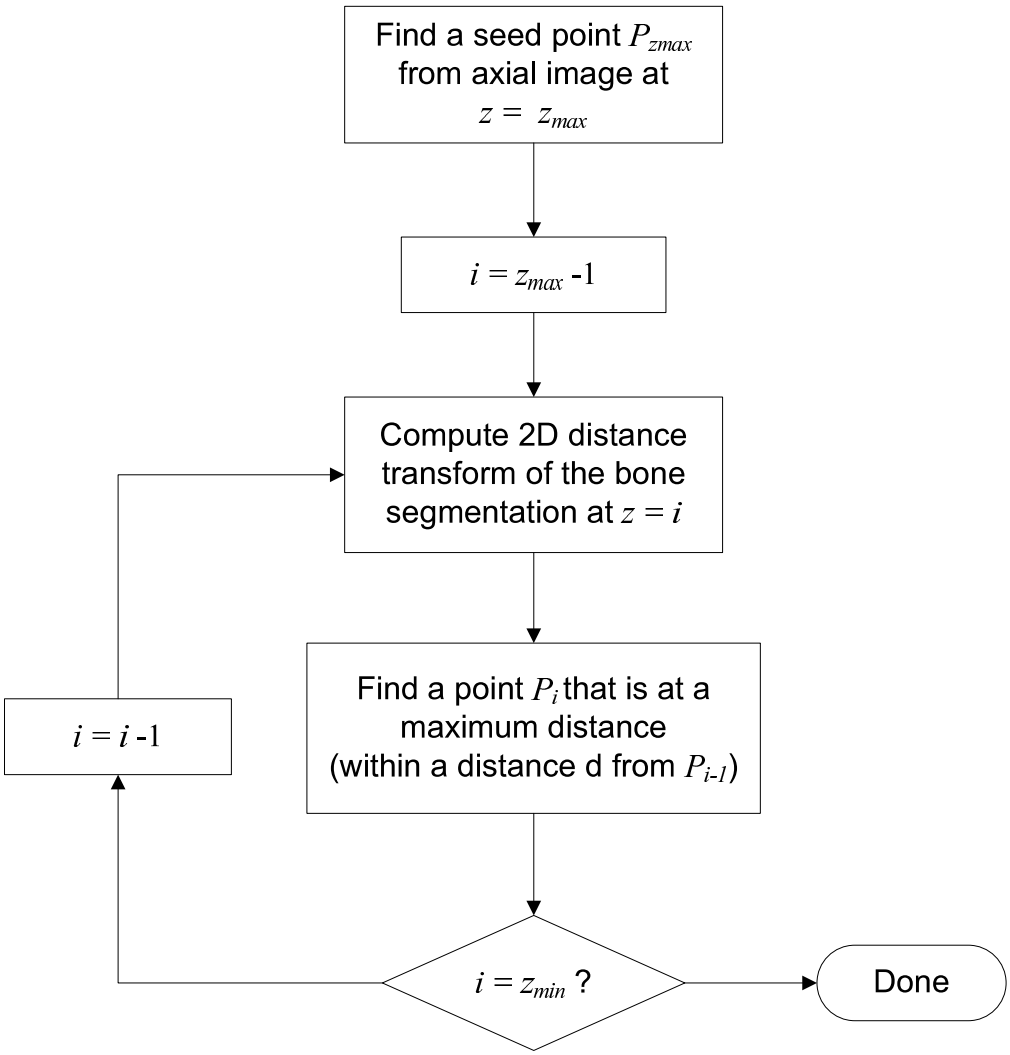

Figure 3.7: Spinal canal tracing algorithm. Spinal canal is traced upward using the distance transform starting from the lowest axial image.

1. Clip the image around the largest component *L*.
2. Invert the image.
3. Perform connected component analysis.
4. Find the largest component not touching the image border.

The 2D distance transform of the bone segmentation is performed to locate the center of the spinal canal in each axial image. A distance transform is labeling of each pixel

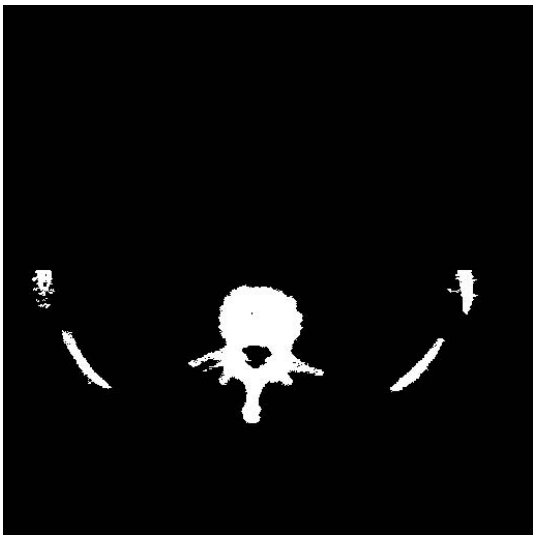

Figure 3.8: Axial projection of lowest 30 mm of the scan. A seed point for spinal canal tracing is identified from the projected image.

with the distance to the nearest non-zero pixel in the image, as illustrated in Figure 3.9. The spinal canal appears approximately circular in an axial view, and the center can be approximated by looking for the maximum distance from the bone. A sequential two-pass method was used to compute distance transform [76].

When performing a distance transform, a distance metric must be defined. Three common metrics are Euclidean, Manhattan, and Chessboard distances:

$$d_{Euclidean} = \sqrt{(x_2 - x_1)^2 + (y_2 - y_1)^2}\ , \tag{3.2}$$

$$d_{Manhattan} = |x_2 - x_1| + |y_2 - y_1|\ , \tag{3.3}$$

$$d_{Chessboard} = \max\{\ |x_2 - x_1|,\ |y_2 - y_1|\ \}\ , \tag{3.4}$$

for two points in the image (x_1, y_1) and (x_2, y_2). Using Euclidean distance gives the most accurate estimation of the distance, but due to high computational cost of computing Euclidean distance, Manhattan distance metric was used for the distance transform.

The bone segmentation and its distance transform are shown in Figure 3.10 for three

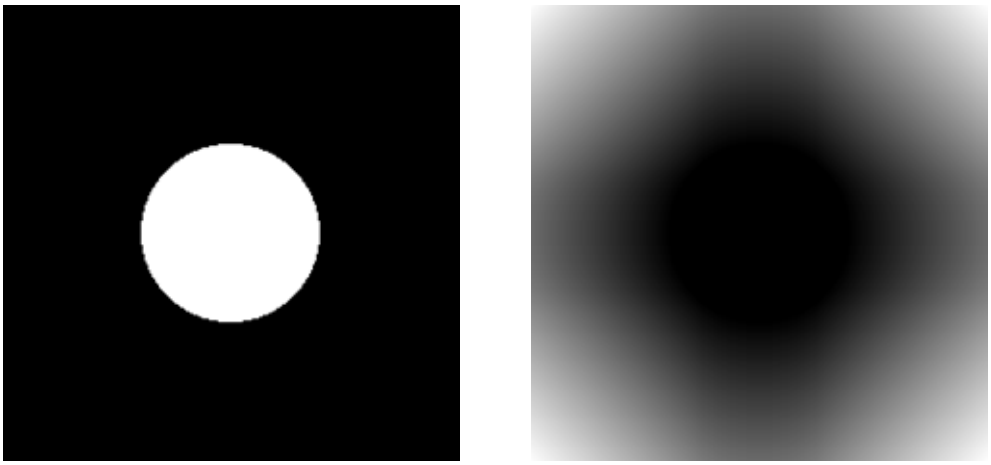

Figure 3.9: Distance transform of an image. (a) Binary image of a circle. (b) Distance transform of (a) using Manhattan distance. In (b), the image intensity indicates the distance to the closest non-zero pixel.

different axial images. The distance transform is performed within a subregion around the spine, as opposed to the entire image, to reduce computational cost. The algorithm parameters were determined using the training cases. The distance d was set to 2.0 mm, and the number of the projected images n was set to the number of slices that correspond to 30.0 mm in thickness:

$$n = \frac{30.0}{r_z}, \tag{3.5}$$

where r_z is the z resolution of the scan (i.e. slice thickness).

3. Seed point detection

The outcome of the bone segmentation in the first stage includes high-intensity bone structures, where different bone structures appear adjacent to each other. To separate ribs from other bones, a seed point is first found, and the complete rib is grown from the seed point. An illustration for detecting a seed region is shown in Figure 3.11. A seed

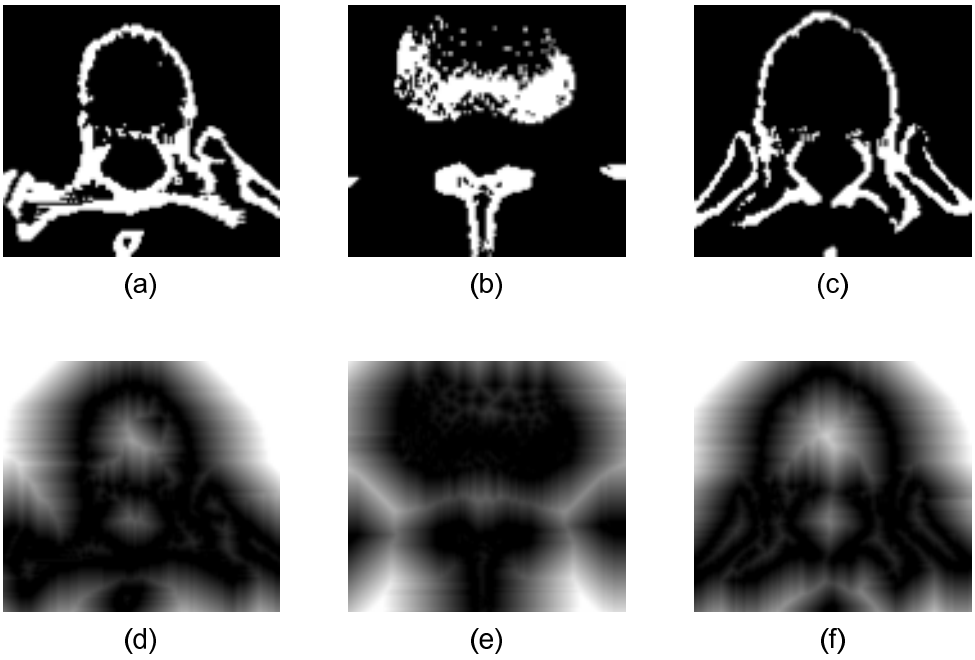

Figure 3.10: Distance transform of bone segmentation. (a)-(c) show the binary images showing bone segmentations in different image slices, and (d)-(e) show the corresponding distance transform.

region *R* for each rib is identified by screening the segmented image region at a distance δ to the left and right of the spinal canal's centerline. The value of δ was set to 45 mm based on observation of the training cases. The value was selected so that the planes do not intersect the tails of vertebrae.

Within each plane, any voxel that belongs to a bone as segmented in the previous section is found, and a 3D connected component is grown within the plane starting at that voxel to identify a set of voxels *R*. The detected region is considered noise and excluded from a set of seed regions if it does not span through the entire width of the bounding plane as shown in Figure 3.11.

A seed point *p* is then found by taking a center of mass of the seed region *R*.

$$p = (\bar{x}, \bar{y}, \bar{z}), \tag{3.6}$$

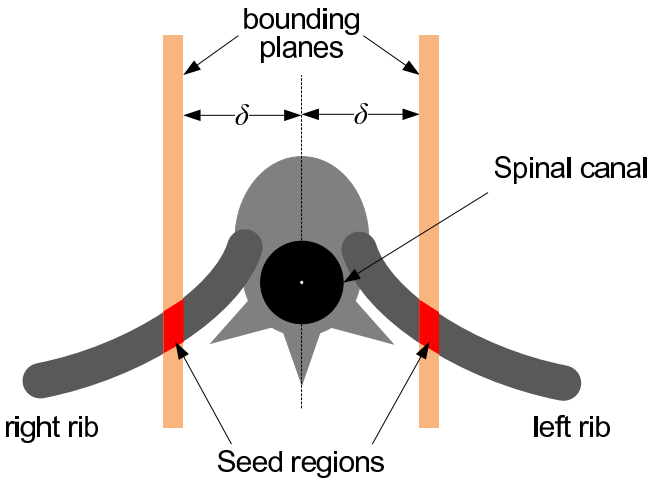

(a)

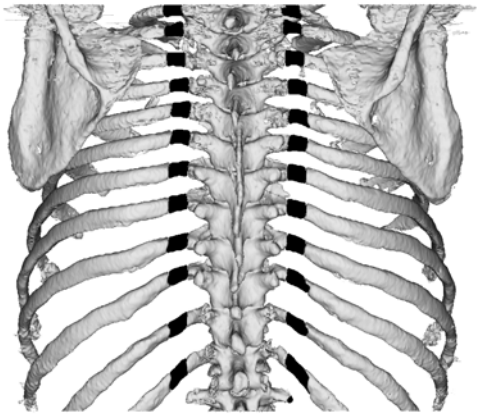

(b)

Figure 3.11: Seed region identification for rib segmentation. (a) A seed is identified for every rib using bounding planes established on both sides of a spinal canal's center point. (b) Detected rib seed regions. Coronal posterior visualization of the segmented bones is shown, with the rib seeds highlighted in black.

where $\overline{x}$, $\overline{y}$, and $\overline{z}$ are computed as:

$$\overline{x} = \frac{\sum_{x,y,z \in R} x}{|R|}, \tag{3.7}$$

$$\overline{y} = \frac{\sum_{x,y,z \in R} y}{|R|}, \tag{3.8}$$

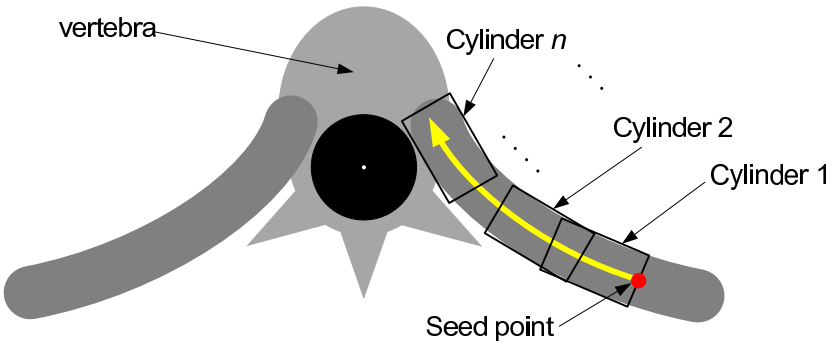

Figure 3.12: Tracing the rib toward vertebra. Starting at a seed point, a cylindrical template is iteratively advanced along the rib.

$$\bar{z} = \frac{\sum_{x,y,z \in R} z}{|R|}. \tag{3.9}$$

4. Rib region growing from a seed point

Every detected seed region is grown into a full rib and given a unique label. The portion of the rib near the vertebra is traced using cylindrical template matching, and the outward portion of the rib is segmented using a simple connected component analysis. The outer portion of the rib is segmented using 3D connected component analysis starting at the seed point using six-connectivity.

The inner portion of the rib is traced by fitting a hollow cylindrical volume along the rib, as illustrated in Figure 3.12. Starting at the seed region, a cylindrical volume is iteratively advanced until it reaches the expected length of the inner rib portion. The expected length is computed by taking the Euclidean distance between the seed region and the center of spinal canal.

Each iteration determines the directional vector v of the cylinder by finding the high-

est cross-correlation to the pre-filtered CT image:

$$v = \underset{dir}{\operatorname{argmax}} \left(\sum_{x,y,z} C_{dir}(x,y,z) \cdot I(x,y,z) \right), \tag{3.10}$$

where C_{dir} is the binary image with a hollow cylindrical template oriented toward *dir*, and I is the mean-filtered CT image.

A hollow cylinder is used to trace along the rib since bone marrow appears in low intensity when compared to the bone surface. The parameters for the cylindrical template, shown in Figure 3.13, include the following:

- d - cylinder diameter (mm)
- w - cylinder wall thickness (mm)
- l - cylinder length (mm)
- δ - inter-cylinder overlap (fraction of l)
- θ_a - search angle in anterior directions (°)
- θ_p - search angle in posterior directions (°)

3.1.3 Experiment to evaluate rib segmentation

The goal of the experiment was to train and evaluate the performance of the automated rib segmentation algorithm. A large dataset composed of > 100 chest CT was used to evaluate the algorithm.

Training the rib segmentation algorithm

The scans of 5 individuals with different rib cage sizes and appearances were selected from the dataset and used to optimize algorithm parameters. The diameter of different

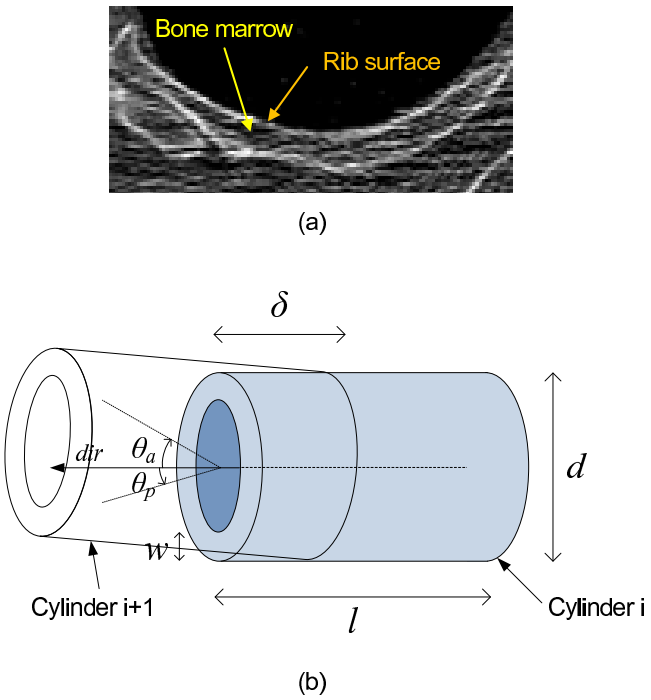

Figure 3.13: Cylindrical template for rib tracing. (a) Bone marrow appears in low intensity compared to the surface, and the hollow cylinder is used to trace the rib. (b) Parameters for the hollow cylinder template include diameter, thickness, height, and search angles.

ribs was observed to vary among different individuals and even within a patient, and d was adaptively adjusted for each rib by finding the value yielding the highest correlation for the first iteration. It has also been observed that the bone marrow region corresponded to approximately one third of the rib thickness, and w was set to 1/3 of d. The search angles were set differently for anterior (θ_a) and posterior (θ_p) directions. A small search angle was used toward posterior direction since the ribs should curve toward anterior direction as it approaches the vertebra. Based on the observation of the training cases, the values of θ_a and θ_p were set to 45° and 2°, respectively.

The parameters l and δ were optimized by performing the segmentation using 20 parameter sets summarized in Table 3.1.3. The segmentation outcomes were visually

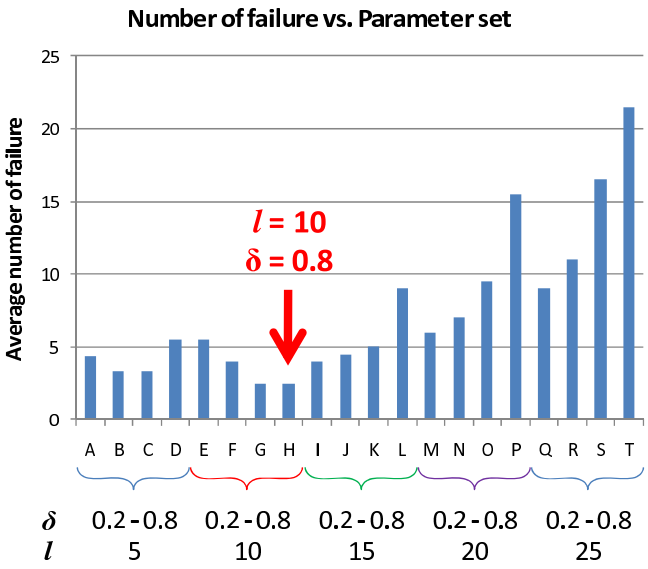

Figure 3.14: Average number of incorrect rib segmentations for different parameter settings.

inspected for incorrect segmentations, and the parameter setting with the smallest number of failure was selected. The number of failures for different parameters is shown in Figure 3.14. The final algorithm parameters were set to $l = 10$ and $\delta = 0.8$, as these values resulted in the lowest number of incorrectly-segmented ribs.

Table 3.1: Parameter settings used for optimization.

Parameter	Description	Range	Δ
l	Cylinder length (mm)	[5, 25]	5
δ	Inter-cylinder overlap (fraction of l)	[0.2, 0.8]	0.2

Evaluation of the rib segmentation algorithm

Each of the CT scans was carefully inspected visually to establish the number of ribs present in each scan. The fully automated method was then run to segment the individual

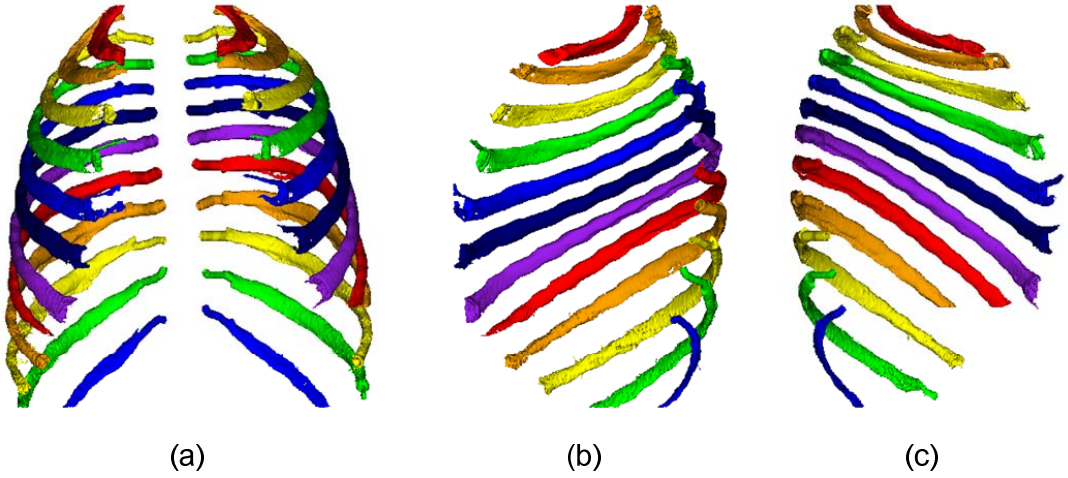

Figure 3.15: 3D visualizations of segmented and labeled ribs. Three different views are shown: (a) coronal view, (b) sagittal view of the right ribs from the center, and (c) sagittal view of the left ribs from the center

ribs. For each case, the outcome was visually inspected to confirm correct segmentation. The algorithm's performance was evaluated by comparing the number of segmented ribs to the number established by the inspector.

The dataset included 115 whole-lung chest CT scans with various parameters from public databases [69, 70]. From the dataset, 5 scans were used for determining algorithm parameters, and the remaining 110 scans were used to evaluate the algorithm performance. All of the scans were taken with low radiation dose (120 - 140 kVp, 40 - 80 mAs) with slice thicknesses varying from 1.25 mm to 2.5 mm. In-plane resolution of the scans ranged from 0.55×0.55 mm to 0.82×0.82 mm. Upon visual inspection of the scans, 24 ribs were present in 106 scans, and only 22 ribs were visible in 4 scans due to scan truncation.

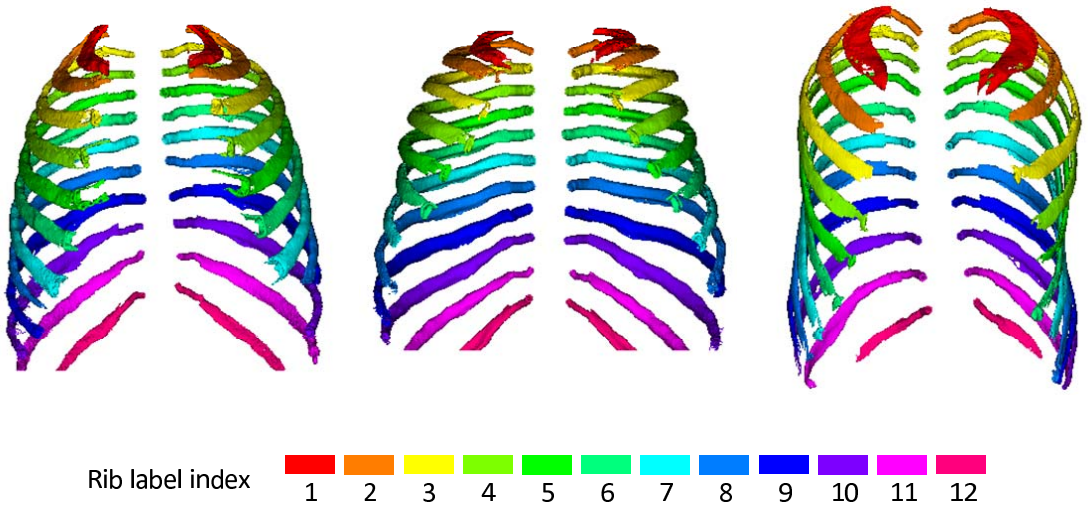

Figure 3.16: 3D visualizations of segmented and labeled ribs. The segmentations from three different CT scans are shown, where each rib is labeled with a unique color.

3.1.4 Results and discussion

Examples of segmentation outcomes are shown in Figure 3.16 as 3D visualizations. The spinal canal was traced successfully with an exception of one case due to incorrect seed point detection. A manually identified seed was used in this case to proceed with the rib segmentation. A total of 2632 ribs were present in 110 CT scans, and the algorithm correctly segmented 2600 ribs (98.8%). All ribs other than the highest and lowest ribs were successfully segmented; of the 32 ribs that were not correctly segmented, 6 were the highest ribs, and 26 were the lowest ribs.

The distribution of cases is shown in Table 3.2, where the cases are categorized into two groups according to the number of ribs present in the scan (24 and 22). For each group, the cases are divided according to the number of ribs that were correctly segmented. There were 90 cases where all ribs present in the scan were correctly seg-

Table 3.2: Distribution for number of segmented ribs

Segmented ribs	Scans with 24 ribs	Scans with 22 ribs
24	86 (81%)	-
23	8 (8%)	-
22	12 (11%)	4 (100%)
Total	106	4

mented.

The presented rib segmentation algorithm is fully automatic without any need for manual intervention. The algorithm was capable of segmenting at least 22 ribs in all cases. Further, the total number of ribs present in all 110 cases was 2632, of which 98.8% (2600 ribs) were successfully segmented. The main cause of missed ribs was the short length of the lowest ribs (Figure 3.17a). Other missed ribs were due to the top-most ribs that were partly truncated (Figure 3.17b). In both situations the algorithm failed to detect the seed since the bounding planes did not intersect the rib.

The segmented ribs may be used to establish a chest frame of reference that defines a common coordinate system for the chest. Such a reference frame will allow for normalization of the chest regions across the CT images of different individuals and facilitate the study of spatial distribution of various anatomical points within chest.

3.2 Segmentation of vertebrae

The vertebrae span along the back of the body and can provide further baseline reference in addition to the ribs. In this section, a fully automated algorithm to segment the

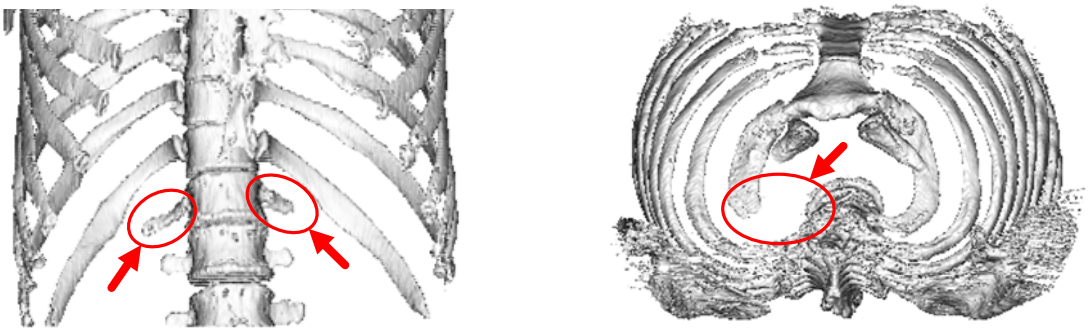

(a) (b)

Figure 3.17: Examples of missed ribs (pointed with arrows). (a) A coronal visualization of the lower rib cage is shown. The lowest ribs with short length were often missed. (b) An axial visualization of the rib cage is shown. The top-most left rib was truncated in the CT image and missed by the algorithm.

individual vertebra from a chest CT scan is presented.

A set of vertebrae form a spine, and each vertebra is composed of a vertebral body, spinous process, and transverse process, as shown in Figure 3.18. The vertebrae are located in the lower central region of an axial CT image. The vertebra is a high-density bone and appears in high intensity, while intervertebral discs appear in low intensity as shown in Figure 3.19.

3.2.1 Strategy for vertebrae segmentation

The presented algorithm separates each vertebra locally without requiring a pre-established appearance model. Previously, Mastmeyer et al. and Klinder et al. have proposed vertebrae segmentation methods using chest CT images. Mastmeyer et al. [53] performed vertebra segmentation using deformable model initiated from the manually marked seed point. Their algorithm however only segmented vertebral body and was not

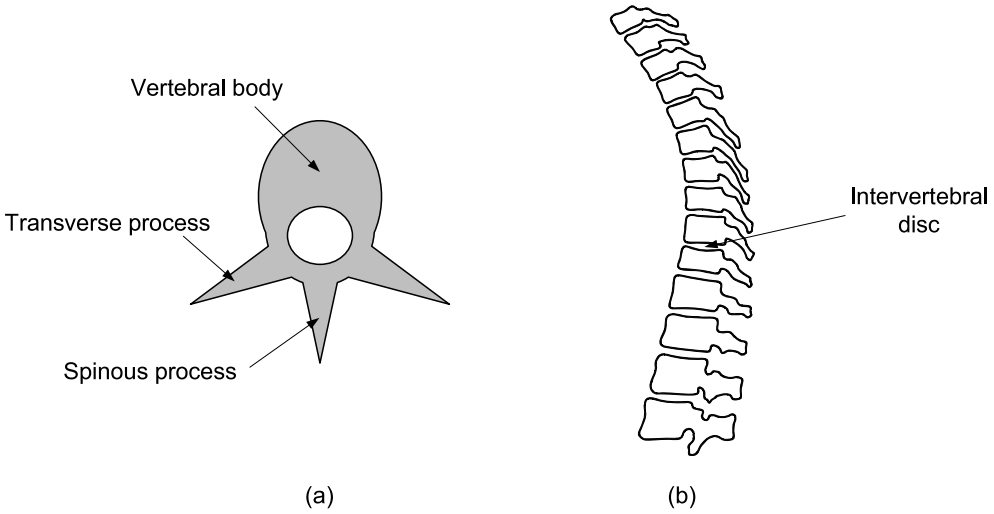

Figure 3.18: Illustration of vertebrae. (a) A vertebra in axial view showing vertebral body, transverse process, and spinous process. (b) A sagittal view of spine showing individual vertebrae and intervertebral disc.

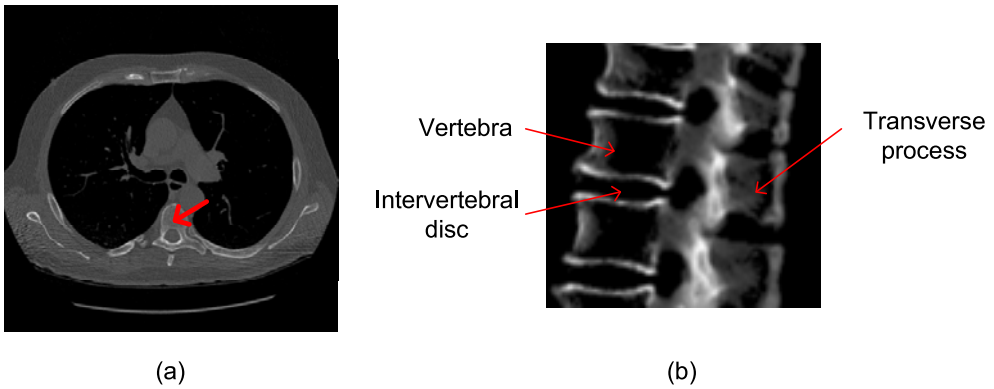

Figure 3.19: Vertebrae in Chest CT. (a) An axial CT image is shown with the vertebra pointed with an arrow. (b) Sagittal view of the lower region of the spine with vertebral body, intervertebral disc, and spinous process labeled.

fully automated. Klinder et al. [44] proposed model-based segmentation and labeling of vertebra. The performance of their algorithm was dependent on the initial model and has failed to work in 14% of the cases.

To segment each vertebra, every pair of consecutive vertebrae is separated by finding

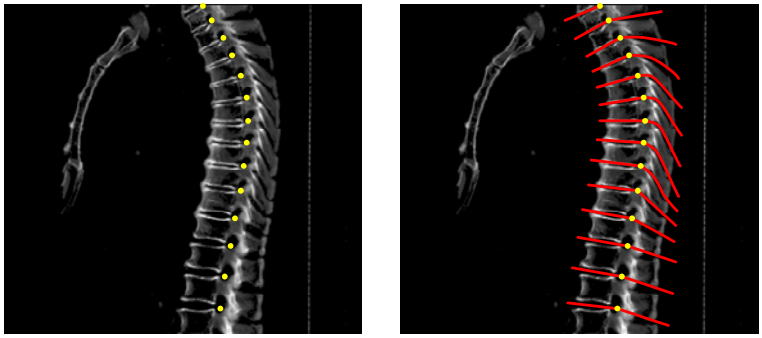

Figure 3.20: The illustration of the vertebrae segmentation approach. For every pair of consecutive vertebrae, a splitting surface is traced from a seed. (a) Seed points identified for every intervertebral disc. (b) Splitting surfaces traced from seed points.

a splitting surface between them. The approach for separating vertebrae is shown in Figure 3.20. First, the spine is identified by excluding the rib segmentation from the bone structure. For every pair of consecutive vertebrae, a seed point is found, and a splitting surface is identified from each seed.

3.2.2 Vertebrae segmentation algorithm

The algorithm to segment individual vertebrae is outlined with a flowchart in Figure 3.21. First, the spine is identified by removing the rib segmentation from the bone structures. Then, a seed point is identified for every splitting surface, and splitting surfaces are traced from the seeds. Finally, individual vertebrae are separated from one another by cutting the spine with splitting surfaces.

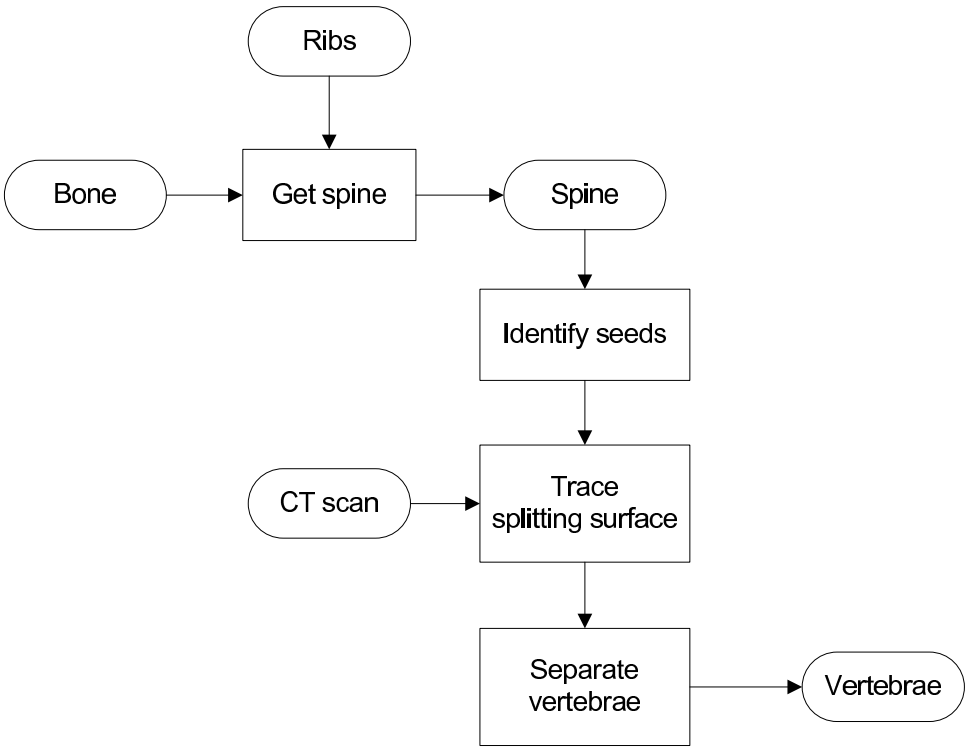

Figure 3.21: Flowchart for the proposed vertebrae segmentation. The spine is identified first and used to identify seed for splitting surface. Once splitting surfaces are identified, the vertebrae are separated from one another.

1. Seed point identification

A seed point is identified for every splitting surface using the fact that the intervertebral discs appear in low intensities. First, intervertebral discs are enhanced by performing morphological closing operation and image subtraction:

$$E = (B \bullet K) - B, \tag{3.11}$$

where E is the disc-enhanced image, B is the bone segmentation, and K is the kernel. The subtraction operation performs simple voxel-to-voxel subtraction of the image. The reason for performing the closing operation was to fill in the intervertebral gap which is adjacent to the vertebrae above and below, and therefore a spherical kernel with ex-

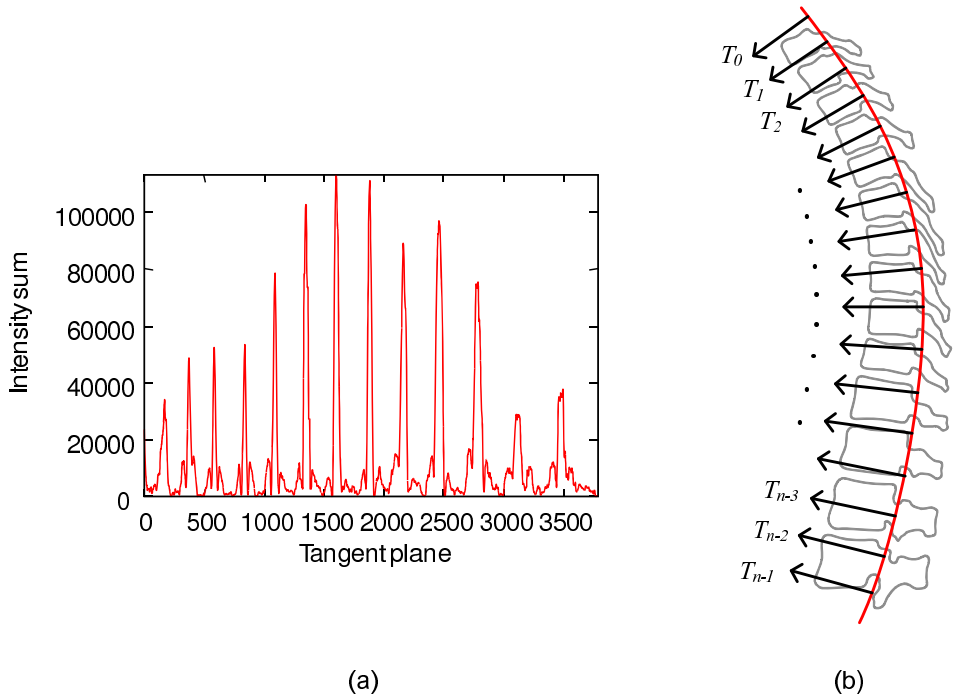

Figure 3.22: Seed point identification. Seed points are identified along the spinal canal's centerline using tangent planes toward anterior directions. (a) Plot of intensity sums for tangent planes along the spinal canal. (b) Illustration of tangent planes in sagittal view. The figure is only for illustration purpose and does not reflect inter-plane interval used by the algorithm.

panded length in z dimension (i.e. $1 \times 1 \times L$ mm) was used. The value of L was set to 6 mm based on the observation of intervertebral discs in the training dataset.

Along the spinal canal's centerline, tangent planes are placed toward anterior direction, as shown in Figure 3.22(b), with 0.1 mm interval. The sampling interval of 0.1 mm was selected conservatively, considering that typical dimension of a scan was $0.5 \times 0.5 \times 1.25$ mm. Then, the sum of the voxel intensities on the enhanced image at each plane is computed. An example plot of intensity sums for tangent planes is shown in Figure 3.22(a).

From a series of intensity sums, the tangent planes where the sums are the local

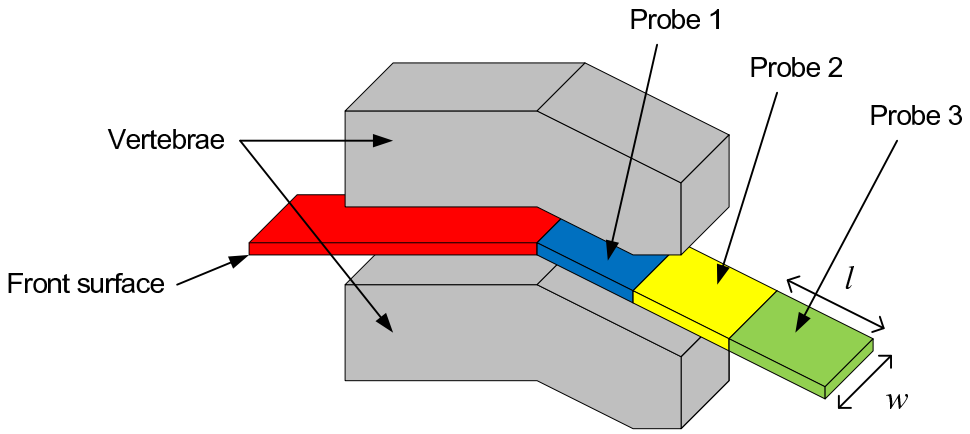

Figure 3.23: Illustration of splitting surface tracing. A rectangular probe is iteratively advanced to trace the posterior splitting surface.

maximas are identified. The intersection of every identified plane and the spinal canal's centerline is then identified as a seed point. This stage of the algorithm not only yields a set of seed points but also provides splitting surfaces (i.e. tangent planes at local maximas) for anterior portions of the vertebrae.

2. Splitting surface tracing and vertebrae separation

This stage of the algorithm traces the splitting surface toward posterior direction in order to separate spinous processes of consecutive vertebrae. The spine is then cut into individual vertebrae using the traced splitting surface.

The posterior surface is traced by iteratively advancing a rectangular probe toward low-intensity gap region as illustrated in Figure 3.23. Each iteration of the algorithm seeks the probe direction that yields the minimum sum of CT intensities:

$$direction = \underset{d}{\operatorname{argmin}} \left(\sum_{x,y,z \in probe_d} I(x,y,z) \right), \tag{3.12}$$

where $probe_d$ is the probe placed toward direction d, and I is the CT image. The al-

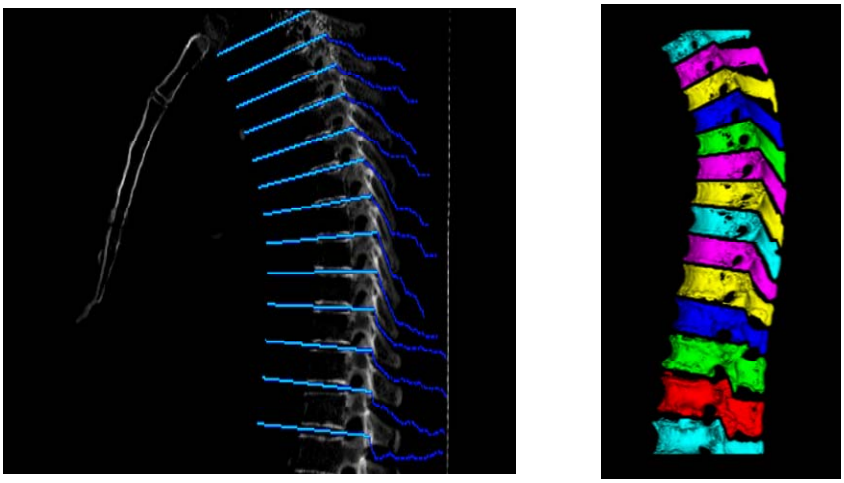

Figure 3.24: Vertebrae separation using splitting surface. (a) The traced splitting surfaces are shown on top of the sagittal bone projection. (b) 3D rendering of separated vertebrae.

gorithm parameters included the width (w) and length (l) of the probe which were optimized using the training dataset.

Once the splitting surface is traced, individual vertebrae may be identified by cutting the spine through the splitting surfaces. In order to achieve this, 3D connected component analysis is performed on the spine using the traced surface as a hard barrier as shown in Figure 3.24. The identified components are then enumerated from top to bottom.

3.2.3 Experiment to evaluate vertebrae segmentation

The goal of the experiment was to train and evaluate the performance of the automated vertebrae segmentation algorithm. A dataset composed of 50 chest CT was used to evaluate the algorithm.

Training

The scans of 5 individuals with different vertebrae sizes and appearances were selected from the dataset and used to optimize algorithm parameters. The parameters w and l were optimized by performing the segmentation using 25 parameter sets summarized in Table 3.2.3.

Table 3.3: Parameter settings used for optimizing vertebrae segmentation.

Parameter	Description	Range	Δ
w	Probe width (mm)	[5, 25]	10
l	Probe length (mm)	[1, 5]	2

The segmentation outcomes were visually inspected for incorrect segmentations, and the parameter setting with the smallest number of failure was selected. The number of failures for different parameters is shown in Figure 3.25. The final algorithm parameters were set to $w = 10$ and $l = 2$, as these values resulted in the lowest number of incorrectly-segmented vertebrae.

Evaluation

Each of the CT scans was carefully inspected visually to establish the number of vertebrae present in each scan. The fully automated method was then run to segment the individual vertebrae. For each case, the outcome was visually inspected to confirm correct segmentation. The algorithm's performance was evaluated by comparing the number of segmented vertebrae to the number established by the inspector.

The dataset included 50 whole-lung chest CT scans. From the dataset, 5 scans were

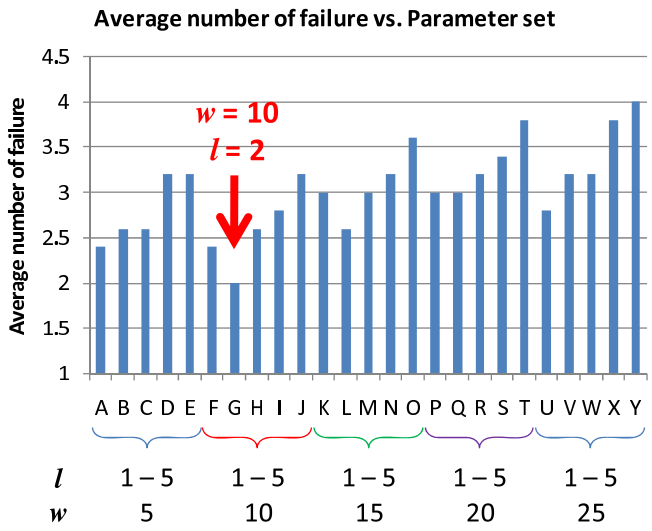

Figure 3.25: Average number of incorrect vertebrae segmentations for different parameter settings.

used for determining algorithm parameters, and the remaining 45 scans were used to evaluate the algorithm performance. All of the scans were taken with low radiation dose (120 kVp, 40 mAs) with slice thickness of 1.25 mm. Upon visual inspection of the scans, total of 575 vertebrae were visible in 45 scans.

3.2.4 Results and discussion

Examples of segmentation outcomes are shown in Figure 3.26 as 3D visualizations. A total of 573 vertebral bodies (99.7%) were correctly identified in 45 CT scans. The algorithm failed to correctly separate 2 vertebral bodies due to small gaps between vertebrae. The algorithm was able to correctly segment 563 spinous processes (96.3%). The incorrect segmentations of the spinous processes were observed where the posterior splitting surface cutting through the vertebra tails.

Our algorithm was able to segment over 95% of vertebrae, including both vertebral

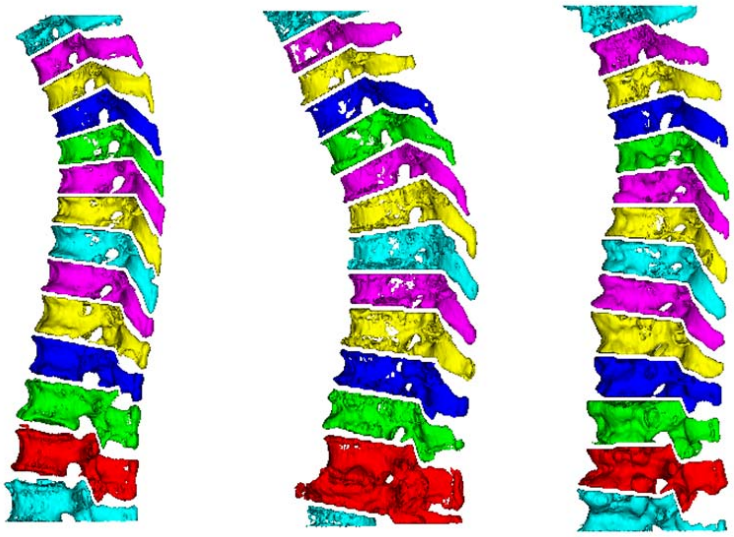

Figure 3.26: 3D visualizations of segmented vertebrae. The segmentations from three different CT scans are shown, where vertebrae are labeled with different colors.

bodies and spinous processes. The limitations of the previously-proposed algorithm [53] were that it required manual seed point for each vertebra and that it segmented vertebral body only. Klinder et al. [44] proposed a segmentation algorithm using global model which failed to work in 14% of the cases. The limitation of the global approach is that it may fail catastrophically on the scans of the patients with unusual skeletal appearances. The presented algorithm separates consecutive vertebrae locally by tracing a surface between them and is not affected by global appearance of a patient.

CHAPTER 4

CHEST FRAME OF REFERENCE

The standardized chest frame of reference (CFOR) is a common reference grid for the chest region. Such a grid provides a mechanism to refer to a specific location within the chest. It can be used to match locations of organs and anatomical features across the scans of same patient and perform comparative studies for a group of subjects. The common reference grid has been established previously to describe a location within human brain, but there was no previous attempt on establishing standardized grid for chest region.

In this chapter, the standard chest frame of reference (CFOR) is defined, and the experiments performed with CFOR are presented. The presented CFOR is defined using the rib cage of a subject and may be used to normalize the size and location of chest region in different CT images and to produce a prior map for an organ of interest. Through inter- and intra- subject experiments using anatomical points of interest, the CFOR scheme is evaluated for its performance as a common chest reference grid.

4.1 Chest frame of reference definition

The chest frame of reference is defined with the coordinate system where for each dimension the frame extents are defined at -1.0 and +1.0. For each scan, the rib cage is used to define the frame extents. The CFOR space is not limited to ±1.0 extent since some anatomical structures may be located outside of the frame. The frame extents are defined for each dimension as shown in Figure 4.1:

- Axial dimension of the chest (z): the bottom-most rib root (z_l) will be -1.0 and the top-most rib root (z_h) will be +1.0.

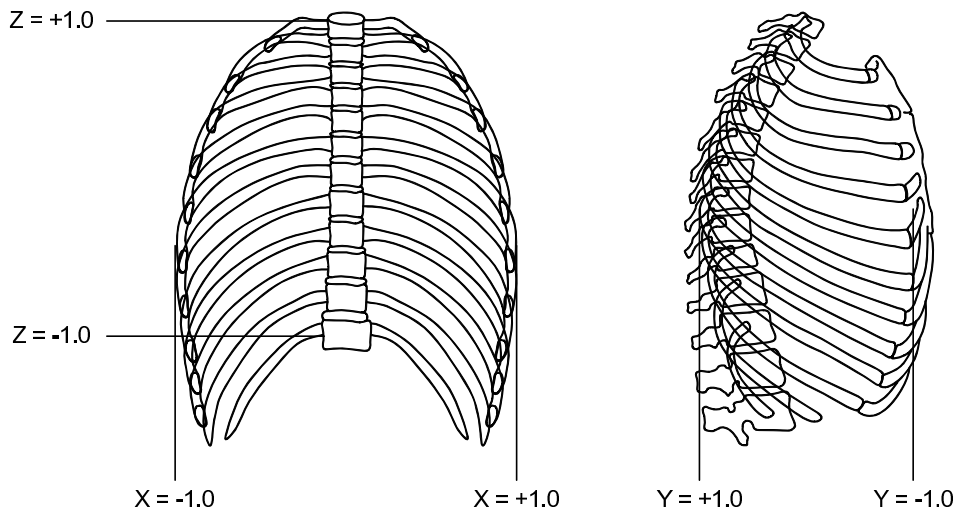

Figure 4.1: Chest frame extents definition using the rib cage. For each dimension, -1.0 and +1.0 extents in the chest frame of reference are defined. Coronal Anterior view of the back half of the rib cage is shown on the left, and a sagittal view of the entire rib cage is shown on the right.

- Sagittal dimension of the chest (x): the patient's right-most extent of the rib cage (x_l) will be -1.0 and the left-most extent of the rib cage (x_h) will be +1.0.
- Coronal dimension of the chest (y): the most anterior extent of the rib cage (y_l) will be -1.0 and the most posterior extent of the rib cage (y_h) will be +1.0.

An example of CT images mapped to the CFOR space is shown in Figure 4.2.

4.2 The scale-translation vector

Figure 4.3 shows how a frame of reference is defined for a chest CT scan. For a given CT scan, a scale-translation vector (STV) is derived using the scale and location of the rib segmentation:

$$STV = \begin{pmatrix} xs & ys & zs & xt & yt & zt \end{pmatrix} . \quad (4.1)$$

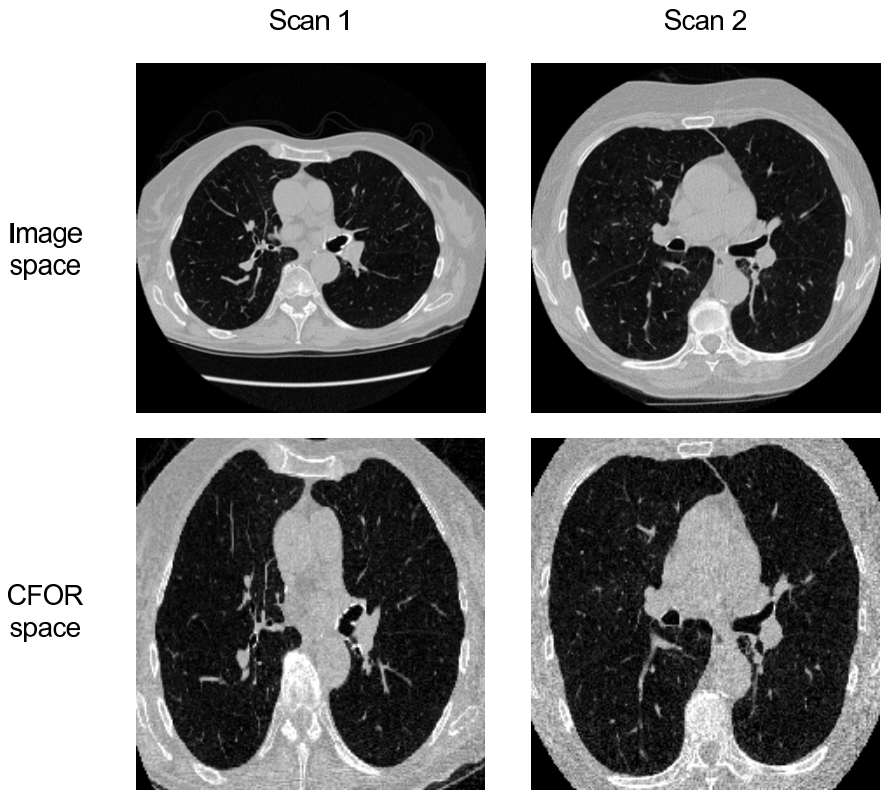

Figure 4.2: Examples of CFOR mapping. Two scans of different patients are mapped to the CFOR space. The CFOR normalizes for different individuals based on their rib size and position within CT images.

The elements of scale-translation vector (STV) are derived using the rib extents, x_l, x_h, y_l, y_h, z_l, and z_h, as defined in Section 4.1:

$$xs = \frac{2}{x_h - x_l}\,, \tag{4.2}$$

$$ys = \frac{-2}{y_h - y_l}\,, \tag{4.3}$$

$$zs = \frac{-2}{z_h - z_l}\,, \tag{4.4}$$

$$xt = \frac{(x_l + x_h)}{2}\,, \tag{4.5}$$

$$yt = \frac{(y_l + y_h)}{2}\,, \tag{4.6}$$

$$zt = \frac{(z_l + z_h)}{2}\,. \tag{4.7}$$

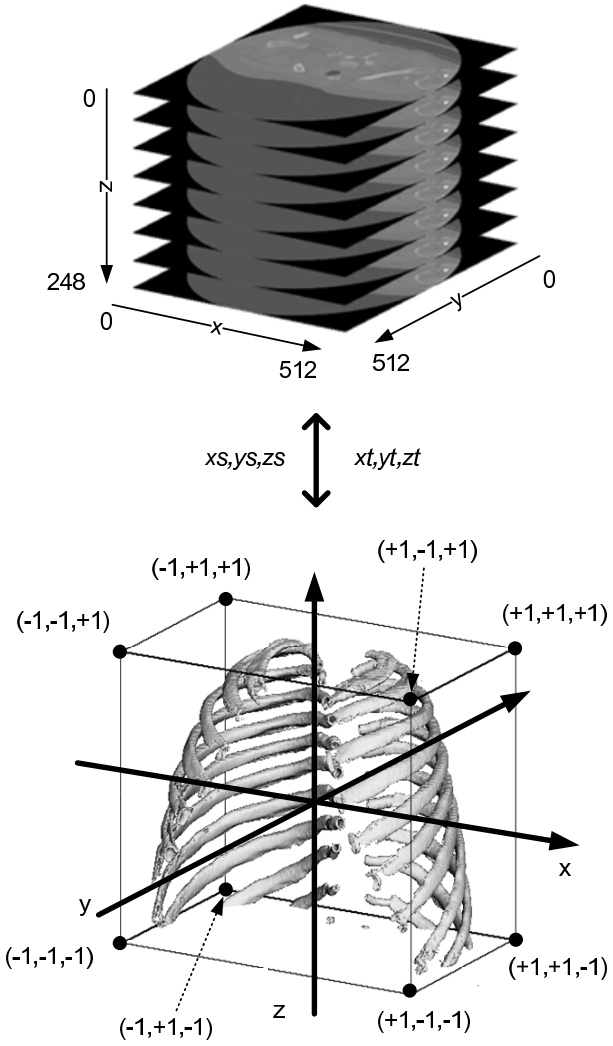

Figure 4.3: Chest frame of reference. A point in a 3D volumetric image (left) can be mapped to a point in the standardized frame of reference (right) using the STV (scale-translation vector). An STV is defined for each CT scan using the segmented rib cage. Note that coordinates outside of ±1 extent for the frame of reference are valid as some parts of the CT image may lie outside of the frame.

Using the elements of STV, a scale matrix **S** and a translation vector **t** are defined as:

$$\mathbf{S} = diag\begin{pmatrix} xs & ys & zs \end{pmatrix}, \tag{4.8}$$

$$\mathbf{t} = \begin{pmatrix} xt & yt & zt \end{pmatrix}^T. \tag{4.9}$$

The elements of STV are specified in terms of millimeters and can be used to map a point between the scan's original coordinate system and the chest frame of reference. An image coordinate may be mapped to and from a CFOR coordinate:

$$\mathbf{c}_{cfor} = \mathbf{S} \cdot (\mathbf{c}_{img} + \mathbf{t}) , \tag{4.10}$$

$$\mathbf{c}_{img} = (\mathbf{S}^{-1} \cdot \mathbf{c}_{cfor}) - \mathbf{t} , \tag{4.11}$$

where $\mathbf{c}_{img}$ is an image coordinate in millimeters, and $\mathbf{c}_{cfor}$ is a CFOR coordinate.

4.3 Experiment to quantify inter-subject variation

The goal of this experiment was to quantify the spatial variation of an anatomical point among different individuals using the established CFOR.

4.3.1 Method

The proposed CFOR scheme was used to obtain the distribution of an anatomical point of interest in the CFOR space over a large number of patients. The tracheal bifurcation point was used as an anatomical point of interest, which was defined in this paper as the point at which the centerline of the airway tree diverges. For each scan, the tracheal bifurcation point was automatically detected as the end point of the first generation branch from a set of airway segments which were identified using the method described in Section 2.2.1.

In order to estimate what the variation within CFOR corresponded to in the real space (i.e. in mm), the mean CFOR coordinate of tracheal bifurcation point was mapped

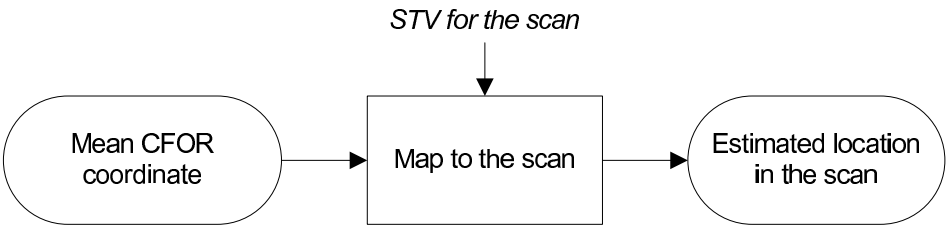

Figure 4.4: Overview of inter-subject evaluation. The mean CFOR coordinate is used to estimate an anatomical point in each scan.

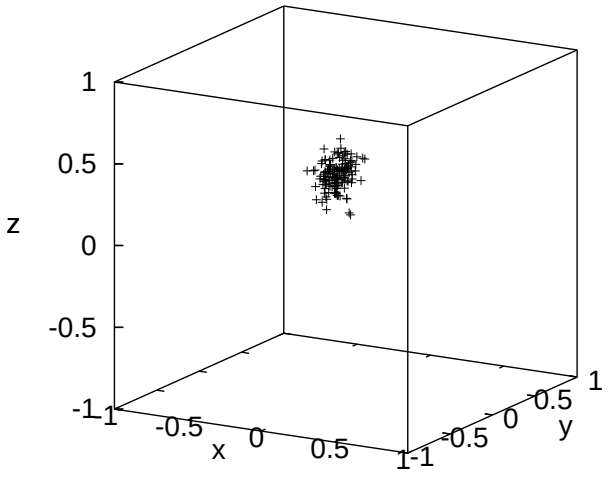

Figure 4.5: Inter-subject distribution of tracheal bifurcation point. The CFOR coordinates of bifurcation points in 134 subjects are plotted in 3D space.

to each scan as shown in Figure 4.4. Then, the distance from the mapped location to the actual location was measured in x, y, and z dimensions.

The dataset included 134 whole-lung CT scans taken with low radiation dose (120 kVp, 40 mAs) and had the slice thickness of 1.25 mm. In-plane resolution of the scans ranged from 0.55×0.55 mm to 0.82×0.82 mm.

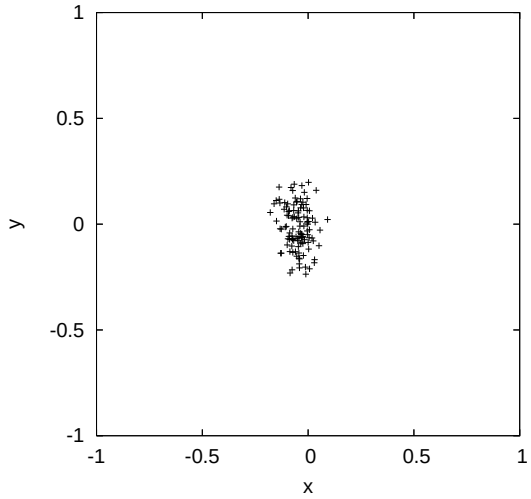

Figure 4.6: Inter-subject distribution of tracheal bifurcation point. The distribution of the CFOR coordinates in axial view is shown.

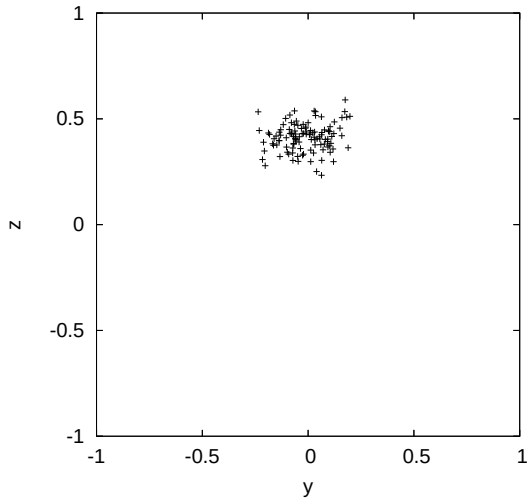

Figure 4.7: Inter-subject distribution of tracheal bifurcation point. The distribution of the CFOR coordinates in sagittal view is shown, and it can be observed that the bifurcation points tend to be located in upper z dimension (i.e. $z > 0$).

4.3.2 Results and discussion

For inter-subject evaluation, the distribution of CFOR coordinates for tracheal bifurcation point in 134 subjects is shown in Figure 4.5. The mean CFOR coordinate was

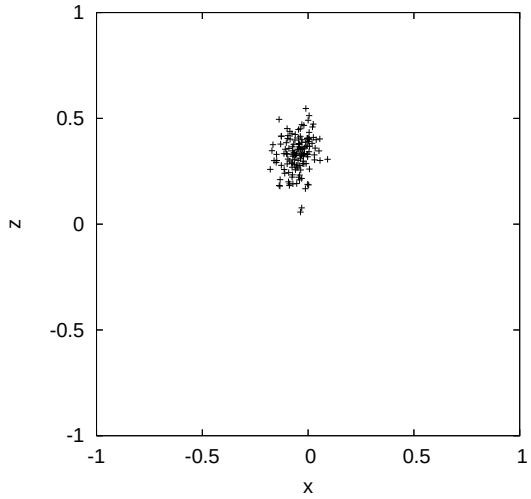

Figure 4.8: Inter-subject distribution of tracheal bifurcation point. The distribution of the CFOR coordinates in coronal view is shown, and it can be observed that the bifurcation points tend to be located in upper z dimension (i.e. z > 0).

(-0.0494, 0.0202, 0.3280). The distance from the actual point to the mean coordinate is shown in Table 4.1, where the Euclidean distance is reported along with the distances in x, y, and z dimensions. On average the bifurcation point was located within 15.40 mm from the mean coordinate.

Table 4.1: Inter-subject localization of tracheal bifurcation point (Mean ± SD)

Measure	Inter-subject variation (mm)
Euclidean distance	15.40 ± 6.73
Distance in X	6.07 ± 4.57
Distance in Y	8.84 ± 5.97
Distance in Z	8.14 ± 6.72

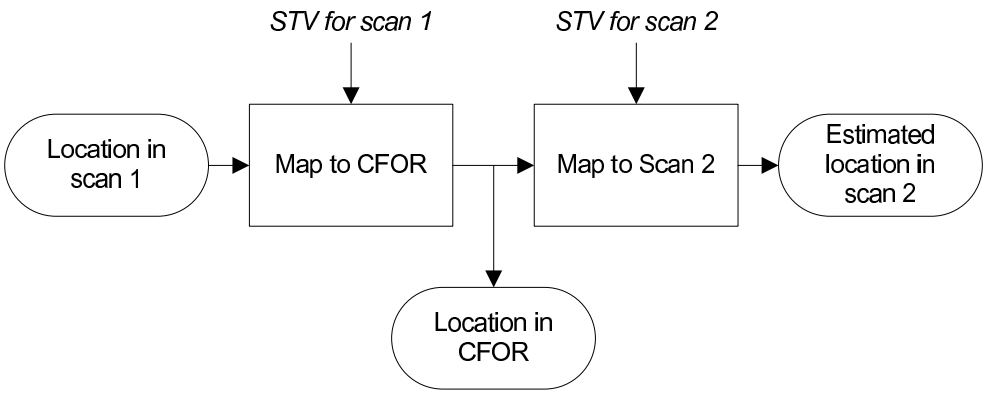

Figure 4.9: Overview of intra-subject evaluation. Given a location in the first scan, the corresponding location in the second scan is estimated using the chest frame of reference.

4.4 Experiment to quantify intra-subject prediction accuracy

The goal of this experiment was to quantify accuracy of predicting anatomical point in a follow-up scan using the established CFOR.

4.4.1 Method

Using the CT scan pair of a same patient, the displacement of the anatomical points within the CFOR space, which would ideally be zero, was measured. First, the anatomical points of interest were separately identified in each scan. In order to estimate what the displacement in CFOR space corresponded to in the actual CT space (i.e. in mm), a point from scan 1 in the CFOR space was mapped to scan 2 as shown in Figure 4.9. The anatomical point in the first scan was mapped to a point in CFOR, and the location of the corresponding point was estimated in the second scan by mapping the CFOR coordinate to the second scan. The accuracy of the prediction was quantified with the distance to the actual location in the second scan.

Since the CFOR was defined separately for each scan, different prediction error was obtained when two scans were swapped (i.e. the second scan's location is mapped to the first one). Since the purpose was to establish a standardized coordinate system for any scan regardless of the acquisition time, the errors for the worst case are reported in this paper.

The CFOR was evaluated using two anatomical points:

- Tracheal bifurcation Point: The bifurcation point described in Section 2.2.1 was used.
- Center of Pulmonary Nodule: Pulmonary nodules with the diameters larger than 2.5 mm were considered for the experiment. The center of the nodule was manually identified in each scan.

4.4.2 Dataset

The dataset included 134 CT scan pairs for the intra-subject evaluation of the bifurcation point. For estimating the nodule's center point, 21 CT scan pairs were used, where a benign pulmonary nodule was manually located in each scan pair.

All CT scans used for the experiments were whole-lung CT scans taken with low radiation dose (120 kVp, 40 mAs) and had the slice thickness of 1.25 mm. In-plane resolution of the scans ranged from 0.55×0.55 mm to 0.82×0.82 mm. The time interval and lung volume change between the scan pair for the intra-subject experiment is shown in Table 4.2. The nodule location was expected to be sensitive to the inspiration, and cases with a lung volume change greater than 20% were excluded from the analysis.

Table 4.2: Dataset for intra-subject evaluation (Mean ± SD)

	Bifurcation point	Nodule center
Number of scan pairs	134	21
Time interval (days)	411 ± 344	667 ± 473
Lung volume difference (%)	4.8 ± 5.2	6.6 ± 6.7

4.4.3 Results and discussion

For intra-subject evaluation, the deviation of the estimated point from the actual location in shown in Table 4.3. The Euclidean distance is reported along with the deviations in x, y, and z dimensions. On average the tracheal bifurcation point was localized to within 10.25 mm from the estimated point, and the nodule center was localized to within 12.33 mm.

In the inter-subject experiment, variability of the bifurcation point location was evaluated using the CFOR. On average the actual bifurcation point deviated by 1.54 cm from the established CFOR coordinate. The most variation was observed in y direction of the scan (mean=8.84 mm), and the least variation was in x direction (mean=6.07 mm).

The CFOR scheme was used to localize a point of interest across the scan pair in the intra-subject experiment. Two anatomical points of interest used in the paper included the bifurcation point of a trachea and the center of a nodule. On average, both anatomical points were localized to within 1.3 cm.

The prediction error of 1.23 cm for the nodule location may be relatively large considering that the mean diameter of the nodules used in the experiment was around 7

Table 4.3: Intra-subject localization of anatomical points (Mean ± SD)

Measure	Bifurcation point (mm)	Nodule center (mm)
Euclidean distance	10.25 ± 4.98	12.33 ± 5.75
Distance in X	5.76 ± 4.64	5.80 ± 4.40
Distance in Y	4.94 ± 3.69	5.48 ± 4.86
Distance in Z	4.54 ± 4.08	7.37 ± 5.09

mm. However, lungs are non-rigid structures and their morphologies may change while breathing. The CFOR scheme still provides a good initial prediction from which the nodules may be further registered using a template matching as shown in [85].

The focus of this study was to establish a standardized chest frame of reference for identifying an anatomical region of interest within entire chest area and provide a framework that may facilitate further registration. The proposed CFOR scheme is preliminary as it does not account for possible rotation of a patient body. The orientation of the body may affect how a CFOR is defined and account for some of the observed prediction errors. The preliminary results show that the proposed CFOR scheme works well in providing a standardized coordinate system.

Figure 4.10 shows the relationship between the prediction errors for the bifurcation point and the nodule center. The prediction errors were plotted for 21 cases in which the nodules were identified. The plot shows that the bifurcation points are better estimated than the nodules but indicates low correlation between the two prediction errors, suggesting that the prediction errors for the two points are not caused by a common scan attribute.

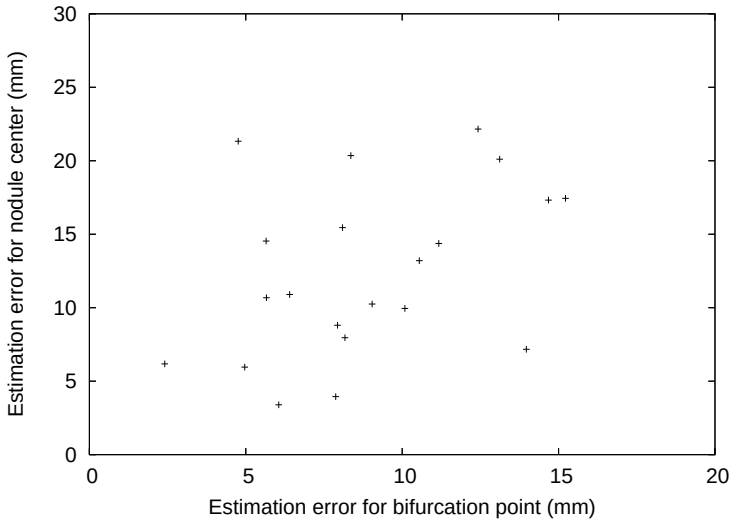

Figure 4.10: Intra-subject deviations of pulmonary nodule and tracheal bifurcation point. For each patient with a documented pulmonary nodule, the estimation error for the nodule center is plotted against the estimation error for the bifurcation point.

4.5 Prior map generation using CFOR

An application of the CFOR is the prior map for an organ of interest. Since CFOR space is normalized for CT images of different subjects, it may be used to build a probability map for an organ. An organ prior map labels each voxel with the probability that the voxel belongs to the organ in the CFOR space. Such a prior map would be useful not only as an initial estimate for locating an organ of interest but also as a reference for segmenting other organs. This section describes how an organ prior map can be generated using CFOR scheme and shows examples of several organs.

4.5.1 Mapping to prior space

The CT image is mapped to the common CFOR space, which is then mapped to the prior map space. The illustration of different image spaces is shown in Figure 4.11. Since the

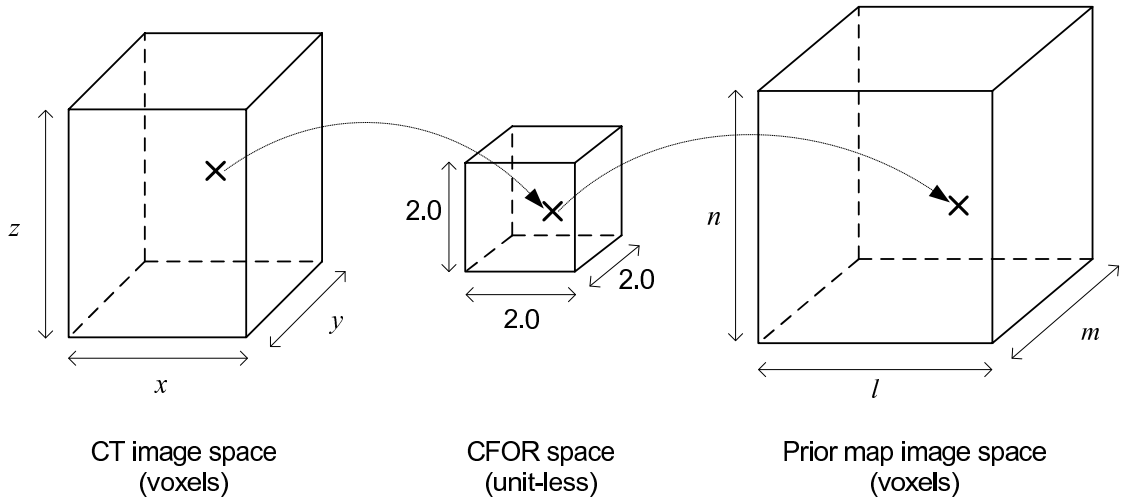

Figure 4.11: Illustration of different image spaces. A $x \times y \times z$ voxels CT image can be normalized using CFOR and mapped to a $l \times m \times n$ voxels prior map. Note that the CFOR is a continuous space that is used to identify a location only and ranges from -1.0 to +1.0 for each dimension.

dimensions of the CT images often vary from one another, the prior map must have a fixed image dimension. The dimension of the prior map may be set arbitrarily, and in this section, *l*,*m*, and *n* are used to note the pre-set dimension of $l \times m \times n$ voxels image.

The prior map P can be thought as an image with its own STV. For a $l \times m \times n$ voxels map P, the STV can be computed as:

$$STV_P = \begin{pmatrix} 0 & 0 & 0 & 2.0/l & 2.0/m & 2.0/n \end{pmatrix}. \tag{4.12}$$

Deriving STV_P this way will result in a prior map image with the dimensions that range from $-l/2$ to $+l/2$, from $-m/2$ to $+m/2$, and from $-n/2$ to $+n/2$ for x, y, and z directions, respectively.

The mapping process is outlined in Figure 4.12. When mapping from CT image space to the CFOR space, the scale-translation vector STV_{CT} associated with the given CT image is used as shown in Section 4.2. Then, the mapped CFOR coordinate is

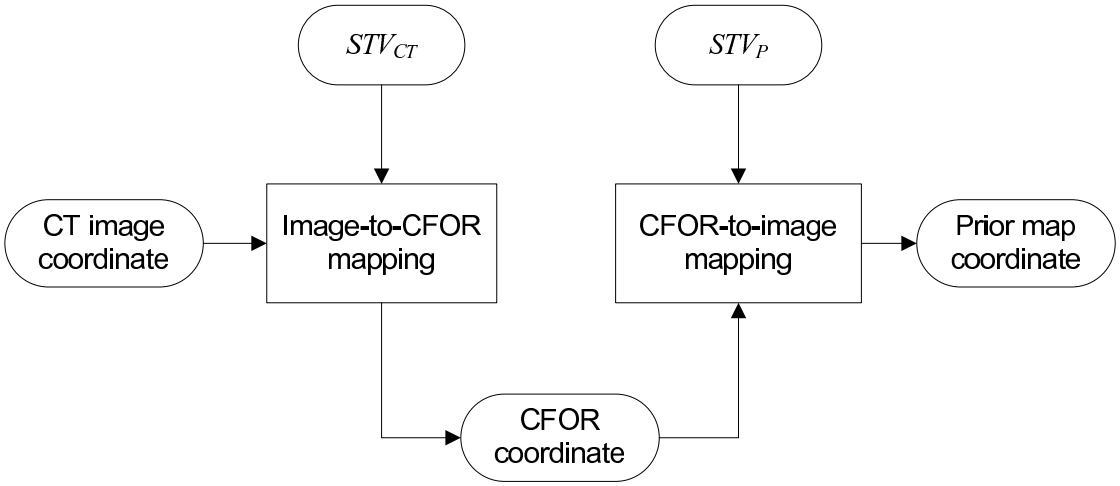

Figure 4.12: Flowchart for coordinate mapping. STV_{CT} and STV_P are used to map a CT image to a prior map using the CFOR.

reverse-mapped onto the prior map using STV_P.

4.5.2 Building an organ prior

A set of CT images can be used to build a prior map for an organ. For each CT images in the dataset, an organ of interest is segmented and represented as a binary image which is then mapped to the prior map space. Each voxel in the prior map is a floating point value representing a fraction of the cases for which the voxel is identified as a part of the organ. In this section, the organ priors are generated for 3 different anatomical structures: lungs, airway tree, and bones. The dataset included 50 low-dose chest CT images from ELCAP public database [69].

For each CT scan, the lungs are automatically segmented using a simple threshold-based algorithm [11]. Further, the airway trees and bone structures are segmented from each CT scan using the algorithms described in Sections 2.1 and 3.1.2, respectively. The

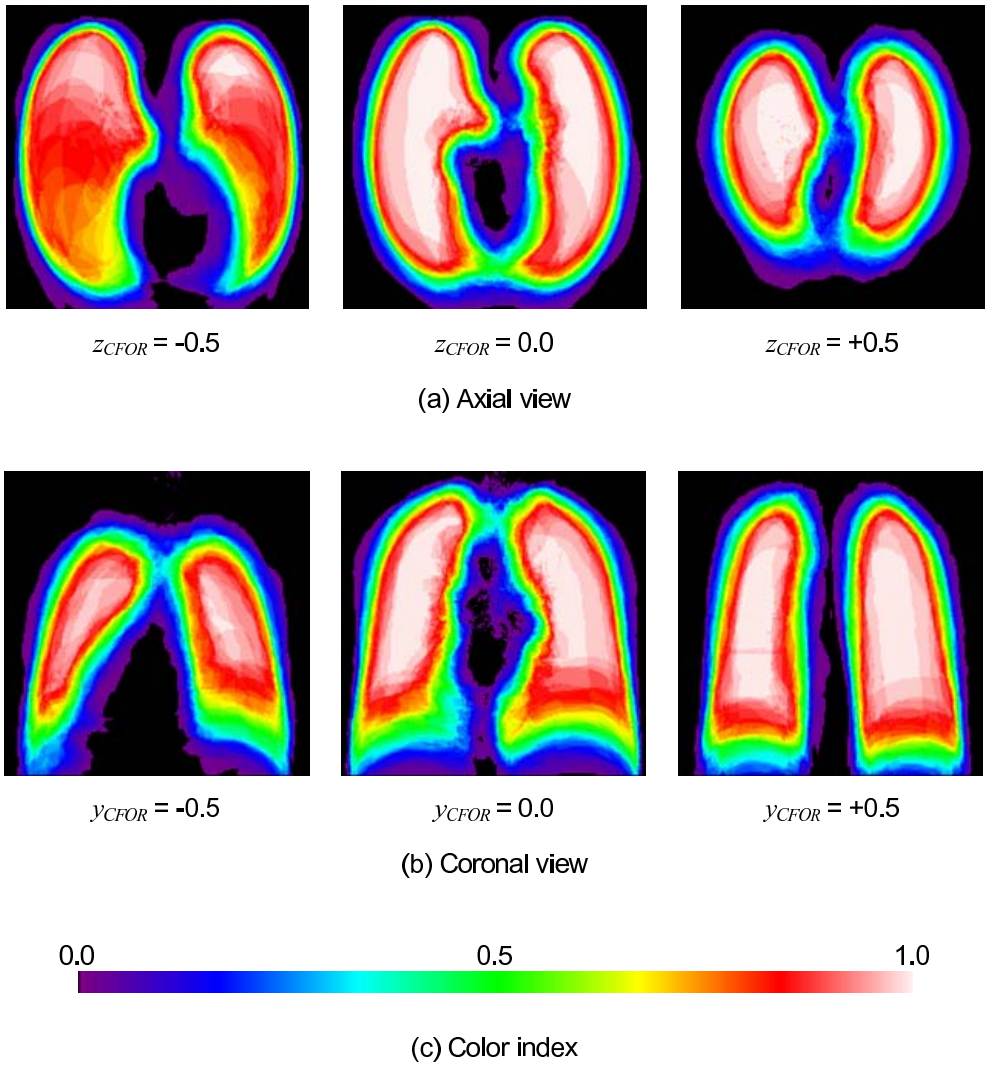

Figure 4.13: Prior map of the lungs.

segmented lungs, airway trees, and bones are then mapped to prior map of 200 × 200 × 200 voxels using the CFOR as described in Section 4.5.1.

The lung segmentation algorithm [11] is as follows:

1. Pre-filter the image with 3×3 median filter.
2. Threshold the image at T_{lung}.
3. Identify a region touching the image border (i.e. background) and remove it.

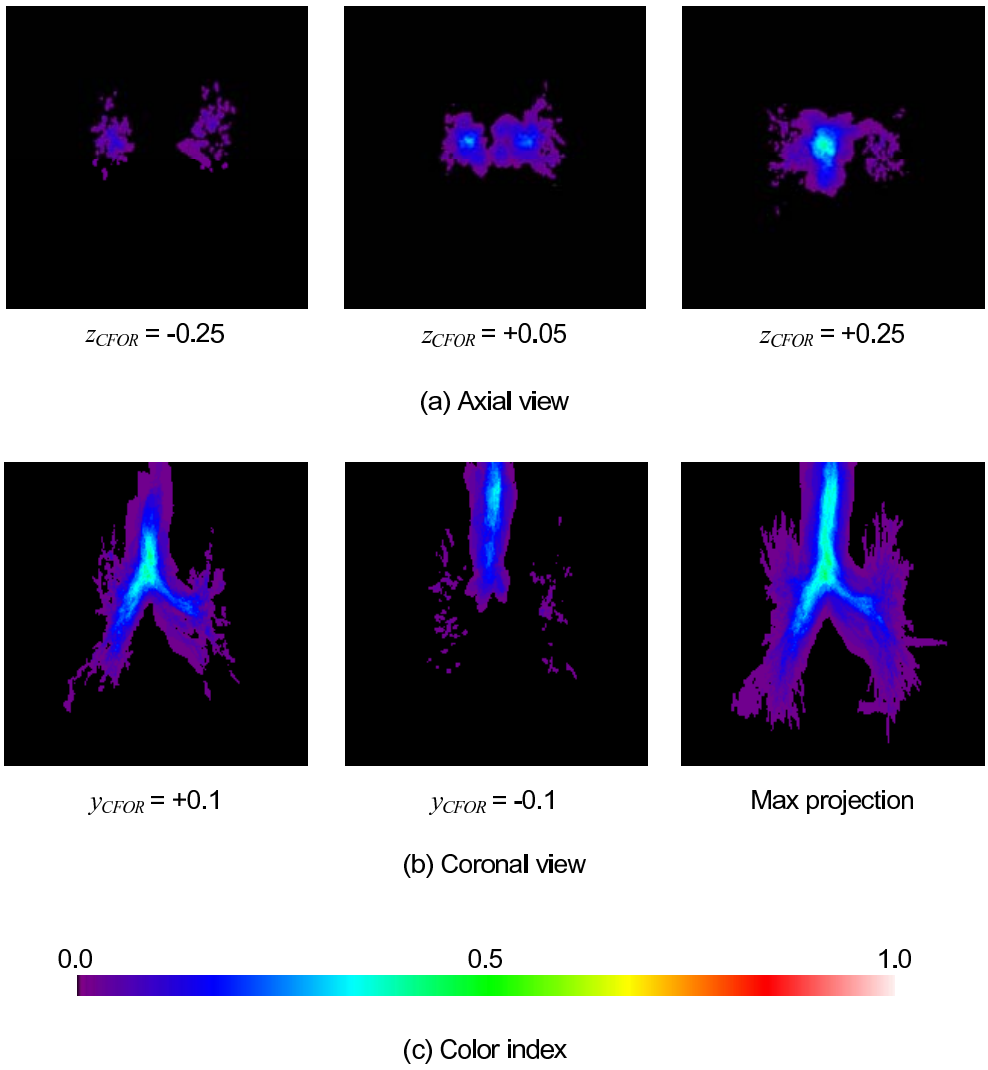

Figure 4.14: Prior map of the airway tree.

4. Invert the image and perform connected component analysis.

5. Remove components with the volume < V_{lung}.

The value of T_{lung} was set to -574 HU to separate regions between densities of soft tissue and air [72]. The lung volume varies depending on several factors such as the age, gender, and height. The typical volume of the lung is 2.5 cm^3 after the end expiratory level of breathing and 5 cm^3 after a full inspiration. For the lung segmentation algorithm, V_{lung} value of 2.0 cm^3 was used.

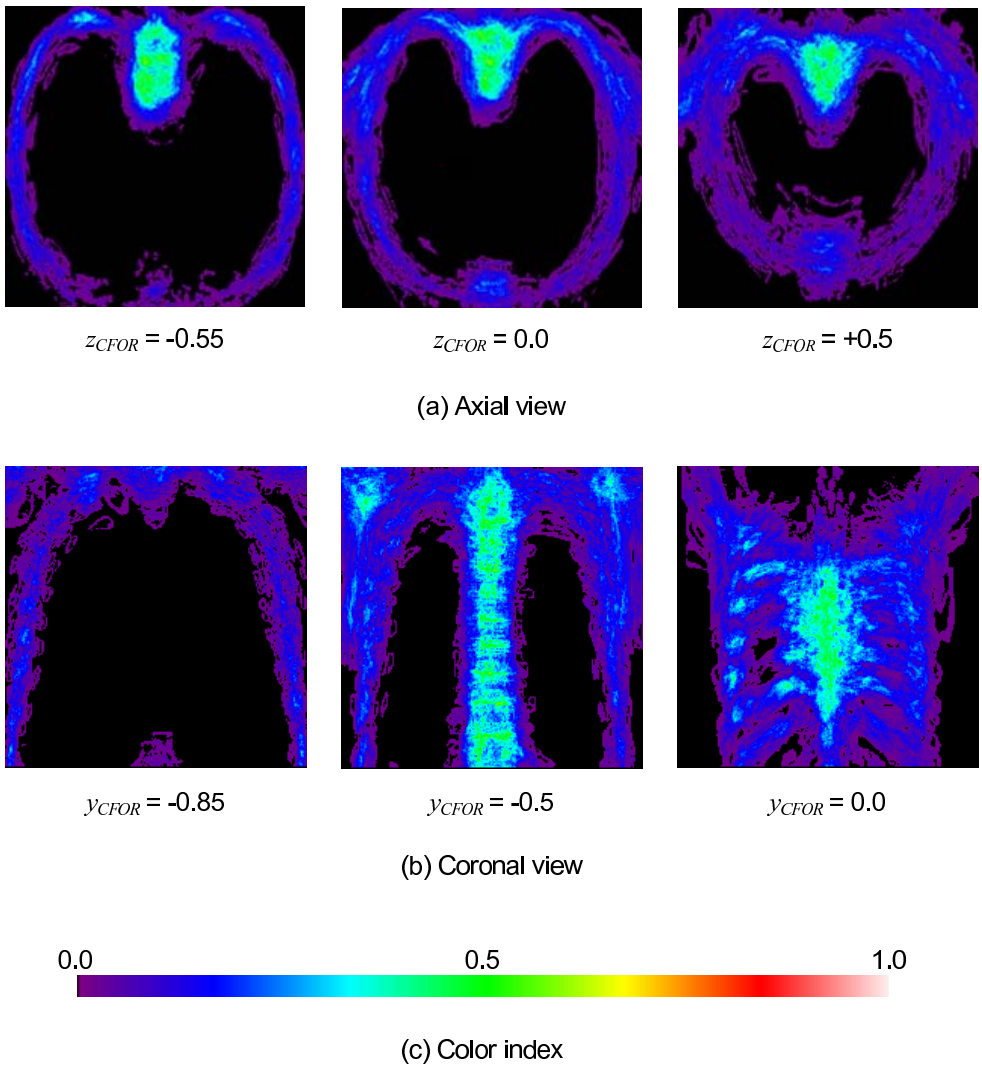

Figure 4.15: Prior map of the bones.

4.5.3 Results and discussion

The prior map of the lungs, airway tree, and bones generated using 50 images are shown in Figures 4.13, 4.14, and 4.15, respectively. The figures show axial and coronal views at different CFOR coordinates.

The lung prior map showed a high probability of 1.0 at the center of each lung, as expected, since lungs in different patients are expected to span through the central

region. In the prior maps for the airways and bones, however, the highest observed probability was approximately 0.6. This indicates that there are less overlap in airway and bones among different patients than lungs.

For the airway tree prior map, the highest probabilities were observed at trachea and two main bronchi, and low probabilities were observed for smaller airways. For bone prior map, the spine and sternum regions showed the highest probabilities.

CHAPTER 5

CONCLUSION

The main focus of this dissertation was to develop computer methods to analyze anatomical structures from low-dose CT images. This work focused on analyzing "low-dose" CT images to obtain diagnostic information. All automated analysis methods presented have been designed for and evaluated on CT images taken with low radiation exposure to the patients. The same methods should work for standard-dose images, as the low-dose scans contain more image noise. The majority of previously-published analysis methods have been designed for and evaluated on standard-dose CT images, and have not been tested or validated for noisy low-dose CT images.

The fully-automated method was developed for analyzing intrathoracic airways, and the precision of the automated measurement was quantified. The algorithms to segment various anatomical structures, including the airway tree, spinal canal, ribs, and vertebrae were presented, and large datasets were used to experiment with the presented algorithms. The segmented rib cage was used as a reference for defining a common chest frame of reference (CFOR).

The ultimate goal of this research is to develop an automated system which retrieves all patient information that can be extracted from a given CT image and are relevant for monitoring health condition. 3D imaging technique is rapidly advancing, and in the near future, such a system may be used to perform a quick automated diagnosis of a patient and will impact how diseases are diagnosed. The automated algorithms presented in this work represent different aspects of such a system. Automated measurements of airways allows for assessment of patient's respiratory health, while segmented skeletal structures may be used to measure bone mineral density. The CFOR scheme allows for both comparison among different patients and monitoring of a same patient at different

times. The presented algorithms collectively serve as important elements in a health-monitoring system.

The novel contributions of this work include:

- Airway segmentation technique with low leakage level
- Precise airway wall thickness measurement technique
- Comparative measurement of airways using repeat scans
- Fully-automated segmentations of anatomical structures, including spinal canal, ribs, and vertebrae
- Establishment of chest frame of reference (CFOR)

5.1 Analysis of intrathoracic airways

The 3D volumetric representation of the airways is available in the chest CT images, and it provides means to quantitatively analyze airway dimensions. A fully-automated method to measure lumen diameter and wall thickness of individual airway branches was developed. The precision of the presented algorithm was validated using a large dataset of 120 serial CT scans.

A method for measuring airway's wall thickness was presented, which showed 55% improvement in measurement precision over the conventional full-width half-maximum (FWHM) based measurements. The presented γ_1 minimization method precisely measures the wall thickness in presence of the adjacent high-intensity structures. The measurement precision, as quantified by 95% limits of agreement of measured pairs, were ±0.9 mm and ±0.5 mm for lumen diameter and wall thickness, respectively.

In order to study intra-subject variation of airway dimensions or to monitor change in a patient's respiratory condition, it is necessary to first match the corresponding airway branches in a serial CT scan pairs. Previous studies have proposed a skeleton-based airway branch matching, where each branch was matched across the scan pair using their geometric locations and inheritance relationships with other branches. A new matching technique that further explored the image voxel values around the airway branch point was presented. Using local image correlation in addition to the skeletal graph resulted in over 99% matching accuracy for intra-subject serial CT scan pairs.

The current practice of assessing patient's respiratory health is to perform a pulmonary function test (PFT). Studying the relationship between the PFT scores and measured airway dimensions may lead to the estimation of PFT scores from low-dose CT scans taken for the screening purpose. The airway measurements were used to estimate PFT scores, and the effect of combining other image-based measures along with the airway measurements was studied. Using multivariate regression model with three other measures, correlation coefficient of 0.52 was achieved for FEV1%/FVC, which was an improvement over using any single measure.

5.2 Segmentation of anatomical structures

Segmentation is a frequent first step in the automated analysis of the anatomical structures. The fully-automated algorithms to segment various anatomical structures were developed and validated using a large dataset of 115 cases. Specifically, the methods to segment the structures including airway tree, spinal canals, ribs, and vertebrae were presented.

The airway tree segmentation algorithm was designed to avoid leakage into lung

parenchyma, which is a well-known issue with a growing-based segmentation, by using strict criteria for growing each voxel. It is essential to minimize leakage level since the resulting segmentation would be used for subsequent measurements. The algorithm performed with a very low leakage level, as less than 1 leakage per case was observed on average of 79 correct segments.

The segmentation of bone structures is important for anatomical analysis of the CT images, as these segmented structures may be used as a reference locations for other organs within a chest as well as for measuring any geometric abnormalities in the bones. Specifically, automated algorithms to segment spinal canal, individual ribs and vertebrae were developed. The spinal canal was correctly segmented in over 99% of the scans. The rib segmentation algorithm correctly segmented 98% of ribs present in the scans, and the vertebrae segmentation algorithm segmented 99.7% of vertebral bodies and 96.3% of spinous process.

5.3 Establishment of chest frame of reference (CFOR)

The chest frame of reference (CFOR) is useful for normalizing chest regions for different-sized individuals, for studying spatial distribution of a certain anatomical locations of interest, or for matching anatomical locations across different intra-subject CT scans. A method to establish a CFOR using the segmented ribs is presented.

Using the presented CFOR scheme, inter-subject experiments was performed for the tracheal bifurcation points, and intra-subject experiments were performed for the tracheal bifurcation point and pulmonary nodule. The results show that the presented CFOR performs well as a standardized grid for chest region as it can localize anatomical points to small subregions. In 136 subjects, 1.5 cm of spatial variation was observed for

tracheal bifurcation point. For intra-subject scans, both tracheal bifurcation point and pulmonary nodule locations were predicted to within 1.2 cm when CFOR was used.

An organ prior map provides an initial estimate for locating an organ of interest and serves as a reference for segmenting other organs. The organ prior maps were generated in the normalized chest space using the presented CFOR scheme.

5.4 Future work

The presented anatomical segmentations are the first steps in building a complete chest atlas. Possible future work is to extract other organs and structures. Heart is located in the middle of the chest, and the entire heart is visible in a chest CT scan. Automated segmentation of heart will provide an opportunity to automatically analyze clinically-relevant measure such as coronary artery calcification. The main challenge in heart segmentation from low-dose chest CT is that it is difficult to separate heart from other structures in the mediastinum due to the similarity in image intensities. Segmentation of vascular structures, including aorta and pulmonary arteries and veins, may aid physicians in detection of aortic disease and pulmonary vascular disease. Automated segmentation of vascular structures are especially challenging due to complex structures of vascular trees.

The presented CFOR is defined on a linear scale where the reference points are defined at low and high extents of each dimension. A possible future direction for the CFOR scheme is to refine the current CFOR scheme that is based on entire rib cage. Individually-labeled ribs and other anatomical structures may be used to define more precise reference points within such a chest frame and establish non-linear definition of the chest frame.

APPENDIX A

EXACT09 DATASET

The acquisition parameters of the testing dataset is shown in Table A.1 [48]. Dosage is presented as x-ray tube current (kVp) and exposure (mAs) pair. The breathing status indicates full inspiration (Insp.) or full expiration (Exp.). Contrast indicates whether intravenous contrast was used during acquisition. The abbreviations for the scanner models are as follows: Siemens Sensation (SS), Siemens Volume Zoom (SVZ), Philips Mx8000 IDT (PMI), Philips Brilliance (PB), Toshiba Aquilion (TA) and GE LightSpeed (GEL). * indicates that the scan is from the same subject as the previous scan.

Table A.1: Acquisition parameters of the 20 test cases [48].

	Thickness (mm)	Scanner	Convolution kernel	Dosage	Breathe state	Contrast
CASE21	0.6	SS64	B50f	200/100	Exp.	No
CASE22*	0.6	SS64	B50f	200/100	Insp.	No
CASE23	0.75	SS64	B50f	200/100	Insp.	No
CASE24	1	TA	FC12	10/5	Insp.	No
CASE25*	1	TA	FC10	150/75	Insp.	No
CASE26	1	TA	FC12	10/5	Insp.	No
CASE27*	1	TA	FC10	150/75	Insp.	No
CASE28	1.25	SVZ	B30f	300/100	Insp.	Yes
CASE29*	1.25	SVZ	B50f	300/100	Insp.	Yes
CASE30	1	PMI16	D	120/40	Insp.	No
CASE31	1	PMI16	D	120/40	Insp.	No
CASE32	1	PMI16	D	120/40	Insp.	No
CASE33	1	SS16	B60f	321/200	Insp.	No
CASE34	1	SS16	B60f	321/200	Insp.	No
CASE35	0.625	GEL16	Std.	441/6209	Insp.	No
CASE36	1	PB16P	C	206/130	Insp.	No
CASE37	1	PB16P	B	64/30	Insp.	No
CASE38*	1	PB16P	C	51/20	Exp.	No
CASE39	1	SS16	B70f	436/205	Insp.	Yes
CASE40	1	SS16	B70s	162/105	Insp.	No

APPENDIX B

EXACT09 RESULTS

The presented airway tree segmentation algorithm's performance is summarized in Table B.1, and the performance of every algorithm evaluated in EXACT09 challenge is summarized in Table B.2 where the performance of our algorithm is indicated in bold.

Table B.1: Evaluation measures for the 20 testing cases.

	Branch count	Branch detected (%)	Tree length (cm)	Tree length detected (%)	Leakage count	Leakage volume (mm^3)	False positive rate (%)
CASE21	76	38.2	43.6	39.5	0	0.0	0.00
CASE22	175	45.2	131.4	39.7	4	155.2	1.09
CASE23	152	53.5	106.8	41.0	2	26.8	0.22
CASE24	53	28.5	46.7	28.7	0	0.0	0.00
CASE25	75	32.1	58.2	23.1	0	0.0	0.00
CASE26	31	38.8	20.9	31.8	0	0.0	0.00
CASE27	33	32.7	23.9	29.5	0	0.0	0.00
CASE28	41	33.3	30.3	27.6	0	0.0	0.00
CASE29	60	32.6	36.5	26.4	0	0.0	0.00
CASE30	43	22.1	28.9	18.9	0	0.0	0.00
CASE31	59	27.6	40.6	23.1	0	0.0	0.00
CASE32	72	30.9	50.5	23.2	1	60.4	0.61
CASE33	62	36.9	44.5	30.3	0	0.0	0.00
CASE34	221	48.3	150.0	42.0	0	0.0	0.00
CASE35	99	28.8	66.5	21.5	1	42.9	0.36
CASE36	44	12.1	39.8	9.7	0	0.0	0.00
CASE37	48	25.9	40.9	23.0	0	0.0	0.00
CASE38	34	34.7	26.6	40.1	0	0.0	0.00
CASE39	110	21.2	88.1	21.5	0	0.0	0.00
CASE40	98	25.2	80.9	20.9	0	0.0	0.00

Table B.2: Average evaluation measures for each team [48]. * indicates semi-automated methods.

Team	Branch count	Branch detected (%)	Tree length (cm)	Tree length detected (%)	Leakage count	Leakage volume (mm^3)	False positive rate (%)
1	91.1	43.5	64.6	36.4	2.5	152.3	1.27
2	157.8	62.8	122.4	55.9	12.0	563.5	1.96
3*	74.2	32.1	51.9	26.9	4.2	430.4	3.63
4	186.8	76.5	158.7	73.3	35.5	5138.2	15.56
5	150.4	59.8	118.4	54.0	1.9	18.2	0.11
6*	77.5	36.7	54.4	31.3	2.3	116.3	0.92
7	146.8	57.9	125.2	55.2	6.5	576.6	2.44
8*	71.5	30.9	52.0	26.9	0.9	126.8	1.75
9	139.0	56.0	100.6	47.1	13.5	368.9	1.58
10	**79.3**	**32.4**	**57.8**	**28.1**	**0.4**	**14.3**	**0.11**
11*	93.5	41.7	65.7	34.5	1.9	39.2	0.41
12	130.1	53.8	95.8	46.6	5.6	559.0	2.47
13	152.1	63.0	122.4	58.4	5.0	372.4	1.44
14	161.4	67.2	115.4	57.0	44.1	1873.4	7.27
15*	148.7	63.1	119.2	58.9	10.4	158.8	1.19

BIBLIOGRAPHY

[1] D. Aykac, E.A. Hoffman, G. McLennan, and J.M. Reinhardt. Segmentation and analysis of the human airway tree from three-dimensional X-ray CT images. *IEEE Transactions on Medical Imaging*, 22(8):940–950, 2003.

[2] P. Berger, V. Perot, P. Desbarats, J.M. Tunon-de Lara, R. Marthan, and F. Laurent. Airway Wall Thickness in Cigarette Smokers: Quantitative Thin-Section CT Assessment1. *Radiology*, 235(3):1055, 2005.

[3] G. Bertrand and G. Malandain. A new characterization of three-dimensional simple points. *Pattern Recognition Letters*, 15(2):169–175, 1994.

[4] M. Betke, H. Hong, D. Thomas, C. Prince, and J.P. Ko. Landmark detection in the chest and registration of lung surfaces with an application to nodule registration. *Medical Image Analysis*, 7(3):265–281, 2003.

[5] D.J. Brenner and E.J. Hall. Computed tomography–an increasing source of radiation exposure. *The New England journal of medicine*, 357(22):2277, 2007.

[6] C. Cohade, M. Osman, L.T. Marshall, and R.L. Wahl. PET-CT: accuracy of PET and CT spatial registration of lung lesions. *European Journal of Nuclear Medicine and Molecular Imaging*, 30(5):721–726, 2003.

[7] M.M. Coselmon, J.M. Balter, D.L. McShan, and M.L. Kessler. Mutual information based CT registration of the lung at exhale and inhale breathing states using thin-plate splines. *Medical Physics*, 31:2942, 2004.

[8] P.A. de Jong, N.L. Muller, P.D. Pare, and H.O. Coxson. Computed tomographic imaging of the airways: relationship to structure and function. *European Respiratory Journal*, 26(1):140, 2005.

[9] K. Doi. Computer-aided diagnosis in medical imaging: historical review, current status and future potential. *Computerized medical imaging and graphics: the official journal of the Computerized Medical Imaging Society*, 31(4-5):198, 2007.

[10] K. Doi, M.L. Giger, R.M. Nishikawa, and R.A. Schmidt. Computer aided diagnosis of breast cancer on mammograms. *Breast cancer*, 4(4):228–233, 1997.

[11] A.A. Enquobahrie, A.P. Reeves, D.F. Yankelevitz, and C.I. Henschke. Automated detection of small pulmonary nodules in whole lung CT scans. *Academic radiology*, 14(5):579–593, 2007.

[12] R. Estépar, G. Washko, E. Silverman, J. Reilly, R. Kikinis, and C.F. Westin. Accurate airway wall estimation using phase congruency. *Medical Image Computing and Computer-Assisted Intervention–MICCAI 2006*, pages 125–134, 2006.

[13] R. Fazel, H.M. Krumholz, Y. Wang, J.S. Ross, J. Chen, H.H. Ting, N.D. Shah, K. Nasir, A.J. Einstein, and B.K. Nallamothu. Exposure to low-dose ionizing radiation from medical imaging procedures. *The New England journal of medicine*, 361(9):849, 2009.

[14] FDA. Reducing radiation from Medical X-rays. *http://www.fda.gov/ForConsumers/ConsumerUpdates/ucm095505.htm*.

[15] J.T. Ferrucci. Colon cancer screening with virtual colonoscopy: promise, polyps, politics. *American Journal of Roentgenology*, 177(5):975, 2001.

[16] C.I. Fetita, F. Preteux, C. Beigelman-Aubry, and P. Grenier. Pulmonary airways: 3-D reconstruction from multislice CT and clinical investigation. *IEEE Transactions on Medical Imaging*, 23(11):1353–1364, 2004.

[17] J. Fripp, S. Crozier, S.K. Warfield, and S. Ourselin. Automatic segmentation of the bone and extraction of the bone–cartilage interface from magnetic resonance images of the knee. *Physics in medicine and biology*, 52:1617, 2007.

[18] M.L. Giger. Computer-aided diagnosis of breast lesions in medical images. *Computing in Science and Engineering*, 2(5):45, 2000.

[19] M.L. Giger. Update on the potential of computer-aided diagnosis for breast cancer. *Future Oncology*, 6(1):1–4, 2010.

[20] F.J. Gilbert and H. Lemke. Computer-aided diagnosis. *British Journal of Radiology*, 78(Special Issue 1):S1, 2005.

[21] G.W. Goerres, E. Kamel, T.N.H. Heidelberg, M.R. Schwitter, C. Burger, and G.K. von Schulthess. PET-CT image co-registration in the thorax: influence of respiration. *European Journal of Nuclear Medicine and Molecular Imaging*, 29(3):351–360, 2002.

[22] M.W. Graham, J.D. Gibbs, and W.E. Higgins. Robust system for human airway-tree segmentation. In *Proceedings of SPIE Meidcal Imaging*, volume 6914, page 69141J, 2008.

[23] P.A. Grenier, C. Beigelman-Aubry, C. Fetita, F. Preteux, M.W. Brauner, and

S. Lenoir. New frontiers in CT imaging of airway disease. *European radiology*, 12(5):1022–1044, 2002.

[24] A. Grgic, U. Nestle, A. Schaefer-Schuler, S. Kremp, E. Ballek, J. Fleckenstein, C. Rube, C.M. Kirsch, and D. Hellwig. Nonrigid Versus Rigid Registration of Thoracic 18F-FDG PET and CT in Patients with Lung Cancer: An Intraindividual Comparison of Different Breathing Maneuvers. *Journal of Nuclear Medicine*, 50(12):1921, 2009.

[25] M.N. Gurcan, B. Sahiner, N. Petrick, H.P. Chan, E.A. Kazerooni, P.N. Cascade, and L. Hadjiiski. Lung nodule detection on thoracic computed tomography images: preliminary evaluation of a computer-aided diagnosis system. *Medical Physics*, 29:2552, 2002.

[26] S. Halligan, D.G. Altman, S.A. Taylor, S. Mallett, J.J. Deeks, C.I. Bartram, and W. Atkin. CT Colonography in the Detection of Colorectal Polyps and Cancer: Systematic Review, Meta-Analysis, and Proposed Minimum Data Set for Study Level Reporting1. *Radiology*, 237(3):893, 2005.

[27] C.I. Henschke, D.F. Yankelevitz, D.M. Libby, M.W. Pasmantier, J.P. Smith, and O.S. Miettinen. Survival of patients with stage I lung cancer detected on CT screening. *The New England journal of medicine*, 355(17):1763–1771, 2006.

[28] Y. Jiang, R.M. Nishikawa, R.A. Schmidt, C.E. Metz, M.L. Giger, and K. Doi. Improving breast cancer diagnosis with computer-aided diagnosis. *Academic Radiology*, 6(1):22–33, 1999.

[29] Y. Kang, K. Engelke, and WA Kalender. A new accurate and precise 3-D segmentation method for skeletal structures in volumetric CT data. *IEEE Transactions on Medical Imaging*, 22(5):586–598, 2003.

[30] S. Katsuragawa and K. Doi. Computer-aided diagnosis in chest radiography. *Computerized Medical Imaging and Graphics*, 31(4-5):212–223, 2007.

[31] M.R. Kaus, K.K. Brock, V. Pekar, L.A. Dawson, A.M. Nichol, and D.A. Jaffray. Assessment of a model-based deformable image registration approach for radiation therapy planning. *International Journal of Radiation Oncology* Biology* Physics*, 68(2):572–580, 2007.

[32] Y. Kawata, N. Niki, H. Omatsu, M. Kusumoto, R. Kakinuma, K. Mori, H. Nishiyama, K. Eguchi, M. Kaneko, and N. Moriyama. Tracking interval changes of pulmonary nodules using a sequence of three-dimensional thoracic images. In *Proceedings of SPIE Medical Imaging*, volume 3979, page 86, 2000.

[33] B.M. Keller, A.P. Reeves, R.G. Barr, D.F. Yankelevitz, and C.I. Henschke. Variation compensation and analysis on diaphragm curvature analysis for emphysema quantification on whole lung CT scans. In *Proceedings of SPIE*, volume 7624, page 762432, 2010.

[34] B.M. Keller, A.P. Reeves, D.F. Yankelevitz, and C.I. Henschke. Automated quantification of pulmonary emphysema from computed tomography scans: comparison of variation and correlation of common measures in a large cohort. In *Proceedings of SPIE*, volume 7624, page 76241Q, 2010.

[35] B.M. Keller, A.P. Reeves, D.F. Yankelevitz, C.I. Henschke, and R.G. Barr. Emphysema quantification from CT scans using novel application of diaphragm curvature estimation: comparison with standard quantification methods and pulmonary function data. In *Proceedings of SPIE*, volume 7260, page 726032, 2009.

[36] J.S. Kim, N.L. Müller, C.S. Park, D.A. Lynch, L.S. Newman, P. Grenier, and C.J. Herold. Bronchoarterial ratio on thin section CT: comparison between high altitude and sea level. *Journal of computer assisted tomography*, 21(2):306, 1997.

[37] A.P. Kiraly, W.E. Higgins, G. McLennan, E.A. Hoffman, and J.M. Reinhardt. Three-dimensional human airway segmentation methods for clinical virtual bronchoscopy. *Academic Radiology*, 9(10):1153–68, Oct 2002.

[38] A.P. Kiraly, B.L. Odry, M.C.B. Godoy, B. Geiger, C.L. Novak, and D.P. Naidich. Computer-aided Diagnosis of the Airways: Beyond Nodule Detection. *Journal of Thoracic Imaging*, 23(2):105, 2008.

[39] A.P. Kiraly, S. Qing, and H. Shen. A novel visualization method for the ribs within chest volume data. In *Proceedings of SPIE Medical Imaging*, volume 6141, page 614108, 2006.

[40] H. Kitaoka and B. Suki. Branching design of the bronchial tree based on a diameter-flow relationship. *Journal of Applied Physiology*, 82(3):968, 1997.

[41] H. Kitaoka, R. Takaki, and B. Suki. A three-dimensional model of the human airway tree. *Journal of Applied physiology*, 87(6):2207, 1999.

[42] T. Kitasaka, K. Mori, J. Hasegawa, Y. Suenaga, and J. Toriwaki. Extraction of bronchus regions from 3D chest X-ray CT images by using structural features of bronchus. In *International Congress Series*, volume 1256, pages 240–245. Elsevier, 2003.

[43] T. Klinder, C. Lorenz, J. von Berg, S.P.M. Dries, T. Bulow, and J. Ostermann. Automated model-based rib cage segmentation and labeling in CT images. *Lecture Notes in Computer Science*, 4792:195, 2007.

[44] T. Klinder, J. Ostermann, M. Ehm, A. Franz, R. Kneser, and C. Lorenz. Automated model-based vertebra detection, identification, and segmentation in CT images. *Medical Image Analysis*, 13(3):471–482, 2009.

[45] T. Kobayashi, XW Xu, H. MacMahon, C.E. Metz, and K. Doi. Effect of a computer-aided diagnosis scheme on radiologists' performance in detection of lung nodules on radiographs. *Radiology*, 199(3):843, 1996.

[46] H. Lamecker, M. Seebass, H.C. Hege, and P. Deuflhard. A 3D statistical shape model of the pelvic bone for segmentation. In *Proceedings of SPIE*, volume 5370, page 1341. Citeseer, 2004.

[47] Q. Li. Recent progress in computer-aided diagnosis of lung nodules on thin-section CT. *Computerized Medical Imaging and Graphics*, 31(4-5):248–257, 2007.

[48] P. Lo, J.M. Reinhardt B. van Ginneken, and M. de Bruijne. Extraction of airways from CT (EXACT'09). In *Proc. of Second International Workshop on Pulmonary Image Analysis*, 2009.

[49] P. Lo and M. de Bruijne. Voxel classification based airway tree segmentation. In *Proceedings of SPIE Medical Imaging*, 2008.

[50] L.M. Lorigo, O. Faugeras, W.E.L. Grimson, R. Keriven, and R. Kikinis. Segmentation of bone in clinical knee MRI using texture-based geodesic active contours. *Lecture Notes in Computer Science*, pages 1195–1204, 1998.

[51] J.A. Maintz and M.A. Viergever. A survey of medical image registration. *Medical Image Analysis*, 2(1):1–36, 1998.

[52] C.J. Martin, D.G. Sutton, and P.F. Sharp. Balancing patient dose and image quality. *Applied Radiation and Isotopes*, 50(1):1–19, 1999.

[53] A. Mastmeyer, K. Engelke, C. Fuchs, and W.A. Kalender. A hierarchical 3D segmentation method and the definition of vertebral body coordinate systems for QCT of the lumbar spine. *Medical image analysis*, 10(4):560, 2006.

[54] D. Mattes, DR Haynor, H. Vesselle, TK Lewellen, and W. Eubank. PET-CT im-

age registration in the chest using free-form deformations. *IEEE Transactions on Medical Imaging*, 22(1):120–128, 2003.

[55] M. Montaudon, M. Lederlin, S. Reich, H. Begueret, et al. Bronchial Measurements in Patients with Asthma: Comparison of Quantitative Thin-Section CT Findings with Those in Healthy Subjects and Correlation with Pathologic Findings1. *Radiology*, 2009.

[56] Y. Nakano, NL Muller, G.G. King, A. Niimi, S.E. Kalloger, M. Mishima, and P.D. Paré. Quantitative assessment of airway remodeling using high-resolution CT. *Chest*, 122(6; Suppl):271–274, 2002.

[57] Y. Nakano, S. Muro, H. Sakai, T. Hirai, K. Chin, M. Tsukino, K. Nishimura, H. Itoh, P.D. Paré, J.C. Hogg, et al. Computed tomographic measurements of airway dimensions and emphysema in smokers. Correlation with lung function. *American journal of respiratory and critical care medicine*, 162(3):1102, 2000.

[58] F.H. Netter. *Atlas of human anatomy*. Saunders, 2006.

[59] NIH. What is chronic obstructive pulmonary disease (COPD)? *http://www.nhlbi.nih.gov/health/dci/Diseases/Copd/Copd_WhatIs.html*.

[60] B.L. Odry, A.P. Kiraly, C.L. Novak, D.P. Naidich, J.P. Ko, and M.C.B. Godoy. Evaluation of scoring accuracy for airway wall thickness. In *Proceedings of SPIE Medical Imaging*, volume 7260, page 72602X, 2009.

[61] K. Palágyi, J. Tschirren, E.A. Hoffman, and M. Sonka. Quantitative analysis of pulmonary airway tree structures. *Computers in biology and medicine*, 36(9):974–996, 2006.

[62] K. Palágyi, J. Tschirren, and M. Sonka. Quantitative analysis of three-dimensional tubular tree structures. *Proceedings of SPIE Medical Imaging*, 5032:267–277, 2003.

[63] T. Pan, O. Mawlawi, N. Swanston, J. Jackson, E. Rohren, and H. Macapinlac. New utility for registration of the CT and PET data in PET/CT. In *Society of Nuclear Medicine Annual Meeting Abstracts*, volume 50, page 1497. Soc Nuclear Med, 2009.

[64] S.J. Park, T.J. Kim, K.G. Kim, S.H. Lee, J.M. Goo, and J.H. Kim. Accurate measurement of respiratory airway wall thickness in CT images using a signal restoration technique. In *Proceedings of SPIE*, volume 6913, page 691336, 2008.

[65] D.A. Pierce and D.L. Preston. Radiation-related cancer risks at low doses among atomic bomb survivors. *Radiation Research*, 154(2):178–186, 2000.

[66] D.L. Preston, E. Ron, S. Tokuoka, S. Funamoto, N. Nishi, M. Soda, K. Mabuchi, and K. Kodama. Solid Cancer Incidence in Atomic Bomb Survivors: 1958-1998. *Radiation Research*, 168(1):1–64, 2007.

[67] D.L. Preston, Y. Shimizu, D.A. Pierce, A. Suyama, and K. Mabuchi. Studies of mortality of atomic bomb survivors. Report 13: Solid cancer and noncancer disease mortality: 1950-1997. *Radiation Research*, 160(4):381–407, 2003.

[68] RadiologyInfo. CAT Scan (CT). *http://www.radiologyinfo.org/en/info.cgm?pg=chestct*.

[69] A.P. Reeves, A.M. Biancardi, , D.F. Yankelevitz, S. Fotin, B.M. Keller, A. Jirapatnakul, and J. Lee. A public image database to support research in computer aided diagnosis. In *Proceedings of IEEE Engineering in Medicine and Biology Conference*, pages 3715–3718, 2009.

[70] A.P. Reeves, A.M. Biancardi, T.V. Apanasovich, C.R. Meyer, H. MacMahon, E.J.R. van Beek, E.A. Kazerooni, D. Yankelevitz, M.F. McNitt-Gray, G. McLennan, et al. The lung image database consortium (LIDC) a comparison of different size metrics for pulmonary nodule measurements. *Academic radiology*, 14(12):1475–1485, 2007.

[71] A.P. Reeves, A. Chan, D. Yankelevitz, C. Henschke, B. Kressler, and W. Kostis. On measuring the change in size of pulmonary nodules. *IEEE Transactions on Medical Imaging*, 25(4):435–450, 2006.

[72] A.P. Reeves and W.J. Kostis. Computer-aided diagnosis of small pulmonary nodules. In *Seminars in Ultrasound, CT, and MRI*, volume 21, pages 116–128. Elsevier, 2000.

[73] J.M. Reinhardt, N.D. D'Souza, and E.A. Hoffman. Accurate measurement of intrathoracic airways. *IEEE Transactions on Medical Imaging*, 16(6):820–827, 1997.

[74] A. Rosenfeld. Connectivity in digital pictures. *Journal of the ACM (JACM)*, 17(1):160, 1970.

[75] A. Rosenfeld and J.L. Pfaltz. Sequential operations in digital picture processing. *Journal of the ACM (JACM)*, 13(4):471–494, 1966.

[76] S. Russell, P. Norvig, and A. Artificial Intelligence. A modern approach. *Artificial Intelligence. Prentice-Hall, Egnlewood Cliffs*, 1995.

[77] O.I. Saba, E.A. Hoffman, and J.M. Reinhardt. Maximizing quantitative accuracy of lung airway lumen and wall measures obtained from X-ray CT imaging. *Journal of Applied Physiology*, 95(3):1063, 2003.

[78] A. Saragaglia, C. Fetita, and F. Preteux. Assessment of airway remodeling in asthma: Volumetric versus surface quantification approaches. *Lecture Notes in Computer Science*, 4191:413, 2006.

[79] D. Sarrut, V. Boldea, S. Miguet, and C. Ginestet. Simulation of four-dimensional CT images from deformable registration between inhale and exhale breath-hold CT scans. *Medical physics*, 33:605, 2006.

[80] J. Schmid and N. Magnenat-Thalmann. Mri bone segmentation using deformable models and shape priors. *Medical Image Computing and Computer-Assisted Intervention–MICCAI 2008*, pages 119–126, 2008.

[81] R. Shekhar, P. Lei, C.R. Castro-Pareja, W.L. Plishker, and W.D. DSouza. Automatic segmentation of phase-correlated CT scans through nonrigid image registration using geometrically regularized free-form deformation. *Medical physics*, 34:3054, 2007.

[82] R. Shekhar, V. Walimbe, S. Raja, V. Zagrodsky, M. Kanvinde, G. Wu, and B. Bybel. Automated 3-dimensional elastic registration of whole-body PET and CT from separate or combined scanners. *Journal of Nuclear Medicine*, 46(9):1488, 2005.

[83] H. Shen, L. Liang, M. Shao, and S. Qing. Tracing based segmentation for the labeling of individual rib structures in chest CT volume data. *Lecture Notes in Computer Science*, pages 967–974, 2004.

[84] J. Shi, B. Sahiner, H.P. Chan, L. Hadjiiski, C. Zhou, P.N. Cascade, N. Bogot, E.A. Kazerooni, Y.T. Wu, and J. Wei. Pulmonary nodule registration in serial CT scans based on rib anatomy and nodule template matching. *Medical Physics*, 34:1336, 2007.

[85] J. Staal, B. van Ginneken, and M.A. Viergever. Automatic rib segmentation and labeling in computed tomography scans using a general framework for detection, recognition and segmentation of objects in volumetric data. *Medical Image Analysis*, 11(1):35–46, 2007.

[86] R.M. Summers, J. Yao, P.J. Pickhardt, M. Franaszek, I. Bitter, D. Brickman, V. Krishna, and J.R. Choi. Computed tomographic virtual colonoscopy computer-aided polyp detection in a screening population. *Gastroenterology*, 129(6):1832–1844, 2005.

[87] T. Sun and Y. Neuvo. Detail-preserving median based filters in image processing. *Pattern Recognition Letters*, 15(4):341–347, 1994.

[88] M.H. Tawhai, AJ Pullan, and PJ Hunter. Generation of an anatomically based three-dimensional model of the conducting airways. *Annals of Biomedical Engineering*, 28(7):793–802, 2000.

[89] J. Tschirren, EA Hoffman, G. McLennan, and M. Sonka. Intrathoracic airway trees: segmentation and airway morphology analysis from low-dose CT scans. *IEEE Transactions on Medical Imaging*, 24(12):1529–1539, 2005.

[90] B. van Ginneken, W. Baggerman, and E.M. van Rikxoort. Robust segmentation and anatomical labeling of the airway tree from thoracic CT scans. *International Conference on Medical Image Computing and Computer-Assisted Intervention*, 11(1):219, 2008.

[91] B. van Ginneken, L. Hogeweg, and M. Prokop. Computer-aided diagnosis in chest radiography: Beyond nodules. *European Journal of Radiology*, 2009.

[92] Web MD. GOLD criteria for COPD. *http://www.webmd.com/lung/copd/gold-criteria-for-copd*.

[93] WebMD. Bone mineral density. *http://www.webmd.com/osteoporosis/bone-mineral-density*.

[94] R. Wiemker, T. Blaffert, T. Bülow, S. Renisch, and C. Lorenz. Automated assessment of bronchial lumen, wall thickness and bronchoarterial diameter ratio of the tracheobronchial tree using high-resolution CT. In *International Congress Series*, volume 1268, pages 967–972. Elsevier, 2004.

[95] S.A. Wood, E.A. Zerhouni, J.D.Hoford, E.A. Hoffman, and W. Mitzner. Measurement of three-dimensional lung tree structures by using computed tomography. *Journal of Applied Physiology*, 79(5):1687–1697, 1995.